

Dissertation

to obtain the academic title

„Doctor rerum naturalium“ (Dr. rer. nat.)

submitted to the council of the

Faculty of Physics and Astronomy of the



**FRIEDRICH-SCHILLER-
UNIVERSITÄT
JENA**

Nanoparticle Tracking Analysis Based on Microstructured Waveguides

research conducted at the



Submitted by:

Fengji Gui

Disputation am 28.05.2024

Gutachter:

1. Prof. Dr. Markus A. Schmidt, Friedrich-Schiller-Universität Jena, Germany
2. Prof. Dr. Christian Eggeling, Friedrich-Schiller-Universität Jena, Germany
3. Prof. Dr. Kyunghwan Oh, Yonsei University, Republic of Korea

To my family and Duoli cat.

Abstract

Nanoparticle tracking analysis is an optical and video-based technique for dynamic monitoring and determining the size distribution of diffraction-limited objects in fluids. Due to the ability to analyze individual nanoparticles, it has become a powerful tool in life science and the study of biochemical processes. However, achieving high-precision measurement of fast diffusing nanoparticles remains a challenge, as it principally requires long trajectories of the mobile targets, and the depth of focus in the microscope is finite. Therefore, a spatial restriction of the diffusive particles is needed. In this context, microstructured optical fibers are excellent platforms to provide confined volumes for the specimens, while the guided fiber modes can supply tailored illuminations, building a compact environment for particle tracking experiments.

The thesis focuses on the approach of fiber-assisted nanoparticle tracking analysis based on elastic light scattering, clarifies its capability of ultralong and fast-tracking of label-free nanoparticles, points out the limitations in the current schemes, and proposes related solutions. Firstly, the thesis reviews the fundamentals of fiber optics and Brownian motion and presents the data methods used in this study. Secondly, a trajectory of 50 nm gold nanosphere with a typical length of 10^5 frames and duration of 40 seconds is obtained by using optofluidic nanobore optical fiber, and the results are compared with state-of-the-art methods. Although the nanochannel transversely confines nanoparticles in the focal plane, the spatial-dependent modal fields cause the scattered intensity to fluctuate with the motion of the target. The third part hence presents a pathway to generate flattened modes within nanofluidic fiber, which allows constant intensity in all three dimensions. As a result, the focal depth is remarkably improved for particle tracking measurements. Also, the general flat-field condition is given for other types of waveguides. Lastly, a novel fiber-integrated optofluidic chip is explored for nanoparticle detection. The concept employs a freely propagating Gaussian beam as illumination for the specimen that is filled in a core-less capillary fiber, aiming to establish a near-flat light field and break through the limits of the flat-field condition in optical fibers.

Overall, the findings of the thesis demonstrate that the fiber-based schemes provide extremely high accuracy and low noise in nanoparticle tracking analysis, and promote the applications of the technique in nanomaterials characterization, microrheology, and fundamental study of light-matter interactions.

Zusammenfassung

Die Nanopartikel-Tracking-Analyse ist eine optische und videobasierte Technik zur dynamischen Überwachung und Bestimmung der Größenverteilung von beugungsbegrenzten Objekten in Flüssigkeiten. Aufgrund der Möglichkeit, einzelne Nanopartikel zu analysieren, ist sie zu einem leistungsstarken Werkzeug in den Biowissenschaften und der Untersuchung biochemischer Prozesse geworden. Die hochpräzise Messung schnell diffundierender Nanopartikel ist jedoch nach wie vor eine Herausforderung, da hierfür grundsätzlich lange Trajektorien der mobilen Partikel erforderlich sind und die Tiefenschärfe von Mikroskopen begrenzt ist. Daher ist eine räumliche Begrenzung der diffusen Partikel erforderlich. In diesem Zusammenhang sind mikrostrukturierte optische Fasern hervorragende Plattformen, die begrenzte Volumina für die Proben bereitstellen und deren geführten Fasermode eine angepasste Beleuchtungen ermöglichen, sodass in den Fasern eine kompakte Umgebung für Partikel-Tracking-Experimente gegeben ist.

Diese Arbeit konzentriert sich auf den Ansatz der fasergestützten Nanopartikel-Tracking-Analyse auf der Grundlage elastischer Lichtstreuung, verdeutlicht dessen Fähigkeit zur ultralangsam und schnellen Verfolgung von markierungsfreien Nanopartikeln, zeigt die Einschränkungen in den aktuellen Ansätzen auf und schlägt damit verbundene Lösungen vor. Zunächst werden in der Arbeit die Grundlagen der Faseroptik und der Brownschen Bewegung erläutert und die in dieser Studie verwendeten Datenverarbeitungsmethoden vorgestellt. Zweitens wird eine Trajektorie einer 50-nm-Goldnanokugel mit einer typischen Länge von 10^5 Frames und einer Dauer von 40 Sekunden mithilfe optofluidischer Nanobore-Lichtwellenleiter aufgenommen und dargestellt und die Ergebnisse mit modernsten Methoden verglichen. Obwohl der Nanokanal die Nanopartikel in der Fokusebene transversal begrenzt, bewirken die räumlich abhängigen Modenfelder, dass die Streuintensität mit der Bewegung der Teilchen schwankt. Im dritten Teil wird daher ein Weg zur Erzeugung abgeflachter Moden innerhalb nanofluidischer Fasern vorgestellt, der zu einer konstanten Intensität in allen drei Dimensionen führt. Dadurch wird die Fokustiefe für Partikel-Tracking-Messungen deutlich verbessert. Auch für andere Wellenleitertypen ist die allgemeine Flatfield-Bedingung gegeben. Schließlich wird ein neuartiger faserintegrierter optofluidischer Chip für die Nanopartikeldetektion untersucht. Das Konzept verwendet einen sich frei ausbreitenden Gauß-Strahl als Beleuchtung für die Probenpartikel, die in eine kernlose Kapillarfaser gefüllt sind, sodass ein nahezu flaches Lichtfeld geschaffen wird, um die Grenzen der Flatfield-Bedingung in optischen Fasern zu überwinden.

Insgesamt zeigen die Ergebnisse der Dissertation, dass die faserbasierten Verfahren eine extrem hohe Genauigkeit und geringes Rauschen bei der Nanopartikel Tracking-Analyse bieten und die Technik voranbringen, die bei der Charakterisierung von Nano-

materialien, der Mikrorheologie und der grundlegenden Untersuchung von Licht-Materie-Wechselwirkungen Anwendung findet.

Contents

Abstract	IV
List of figures	X
List of Tables	XII
List of Abbreviations	XIII
1 Introduction	1
1.1 Nanoparticle Tracking Analysis	1
1.2 Fiber-assisted Nanoparticle Tracking Analysis	3
1.3 Motivation of the Thesis	3
1.4 Contents of the Thesis	5
1.5 Highlight of the Contributions	6
2 Fundamentals of Fiber Optics and NTA	7
2.1 Introduction to Optical Fiber	7
2.1.1 Step-index Optical Fiber	7
2.1.2 Nanobore Optical Fiber	10
2.2 Introduction to Brownian Motion	12
2.2.1 Diffusion Equation	13
2.2.2 Mean Square Displacement	14
2.2.3 Video-based Tracking and Error Analysis	15
2.2.4 Power Spectral Density Method	20
2.3 Chapter Summary	21
3 Ultralong Tracking of Nanoparticle in NBF	22
3.1 Introduction	22
3.2 Concept and Experimental Setup	23
3.3 Methods	26
3.3.1 MSD Analysis	27
3.3.2 PSD Analysis	28
3.3.3 Random Walk Simulation	28
3.3.4 Hindrance Effect and Averaged Resistance Factor	28
3.4 Results	30
3.4.1 MSD and PSD Analysis	30
3.4.2 Segmented Trajectory	31
3.4.3 Error Analysis	32
3.5 Discussion	34

3.6	Chapter Summary	36
4	NTA with Flattened Mode in NBF	38
4.1	Introduction	38
4.2	Working Principle	40
4.2.1	Flat-Field Condition	40
4.2.2	Flattened Mode in NBF	42
4.2.3	Numerical Simulation	43
4.3	Results	47
4.3.1	Diffusion Length Estimation	47
4.3.2	Experimental Setup	48
4.3.3	Modal Distribution Measurement	49
4.3.4	Case 1: Water-Filled NBF	50
4.3.5	Case 2: RI-adjusted Liquid and Temperature Scan	51
4.4	Discussion	55
4.5	Materials and Methods	56
4.5.1	Nanoparticle Solution	56
4.5.2	Optical Setup	57
4.5.3	Data Analysis	58
4.5.4	Random Walk Simulation in Circular Domain	60
4.6	Chapter Summary	64
5	NTA with Flattened Illumination in Capillary Fiber	65
5.1	Introduction	65
5.2	Working Principle	66
5.2.1	Illumination with Gaussian Beam	67
5.2.2	Numerical Simulations	68
5.2.3	Experimental Setup	72
5.3	Results	73
5.3.1	Scattered Intensity Measurement	74
5.3.2	MSD Analysis	77
5.4	Discussion	81
5.5	Chapter Summary	82
6	Summary and Outlook	83
6.1	Summary of the Thesis	83
6.2	Outlook	84
	References	85
	Acknowledgment	94

Curriculum Vitae	95
Publications	96
Ehrenwörtliche Erklärung	98

List of figures

Figure 1.1:	Sketch of FaNTA	4
Figure 1.2:	Sketch of flattened-mode FaNTA	5
Figure 2.1:	Sketch of step-index fiber	7
Figure 2.2:	Effective mode index of step-index fiber	9
Figure 2.3:	Sketch of nanobore optical fiber	10
Figure 2.4:	PSF of nanoparticle	16
Figure 2.5:	Random walk simulation with microsteps	19
Figure 3.1:	Sketch of the NBF-based NTA	24
Figure 3.2:	Size characterization of the nanospheres	25
Figure 3.3:	Experimental setup of the FaNTA	27
Figure 3.4:	MSD curves of the nanoparticle in NBF	29
Figure 3.5:	Results of the MSD and PSD fittings	31
Figure 3.6:	MSDs of the segmented sub-trajectories	32
Figure 3.7:	Segmented MSD analysis	33
Figure 3.8:	Statistical results of the segmented analysis	34
Figure 3.9:	Comparison of reported NTA experiments	36
Figure 4.1:	Concept of the light strand	39
Figure 4.2:	Flat mode in slab waveguide	42
Figure 4.3:	Flat fields in NBF	44
Figure 4.4:	Flat mode in liquid-filled NBF	45
Figure 4.5:	Modes study of liquid-filled NBF	45
Figure 4.6:	Sensitivity of the Flat-field Condition	46
Figure 4.7:	Optical setup of the FaNTA	48
Figure 4.8:	Definition of the bins for mode analysis	50
Figure 4.9:	Statistical analysis of the modal fields in water-filled NBF	51
Figure 4.10:	RIs of DMSO/water mixture	52
Figure 4.11:	Temperature scan of the RI-adjusted NBF	53
Figure 4.12:	Scattering cross-section of gold nanosphere	57
Figure 4.13:	Intensity measurement of a static nanoparticle	58
Figure 4.14:	Measured intensities with the transversal positions	59
Figure 4.15:	Simulation of the intensity sampling	61
Figure 4.16:	Simulated intensities with the transversal positions	62
Figure 4.17:	Simulation of the temperature scan	63
Figure 5.1:	Sketch of the fiber-assisted optofluidic device	68
Figure 5.2:	Calculation of Gaussian beam	69
Figure 5.3:	Mode simulation of the water-filled case	70
Figure 5.4:	Mode simulation of RI-mismatch cases	71

Figure 5.5:	Simulation of the mode in capillary fiber	72
Figure 5.6:	Experimental setup of the optofluidic device	73
Figure 5.7:	Image of the experimental device	74
Figure 5.8:	Results of the intensity measurement	75
Figure 5.9:	Histograms analysis of the scattered intensity	76
Figure 5.10:	Intensity measurement of static nanoparticle	77
Figure 5.11:	MSD analysis	78
Figure 5.12:	Segmented analysis	79

List of Tables

Table 3.1:	Key parameters in recent NTA experiments	35
Table 4.1:	Parameters to estimate the diffusion length	48
Table 4.2:	Statistical benchmarks of the modes analysis	54
Table 4.3:	Parameters to calculate RI of DMSO/water mixture	56
Table 5.1:	Key results of the intensity measurement	77
Table 5.2:	Key results of the MSD analysis	80

List of Abbreviations

NTA	nanoparticle tracking analysis
EM	electron microscop
MSD	mean square displacement
SPT	single particle tracking
SNR	signal-to-noise ratio
FaNTA	fiber-assisted nanoparticle tracking analysis
NBF	nanobore fiber
RI	refractive index
HCF	hollow core fiber
PCF	photonic crystal fiber
ARHCF	anti-resonant hollow core fiber
iSCAT	interferometric scattering microscopy
DMSO	dimethyl sulfoxide
FEM	finite element method
PSD	power spectra density
PDF	probability density function
PSF	point spread function
LSF	least-square fit
CRLB	Cramér–Rao lower bound
MLE	maximum likelihood estimation
FWHM	full-width-half-maximum
FoV	field of view
CB	central bin
SB	side bin

1 | Introduction

1.1 Nanoparticle Tracking Analysis

Micro- and nano-scale particles, formed naturally or artificially, play important roles in many research fields. Detecting and sizing these small objects are fundamental tasks in the area of scientific analyses, for example, environmental monitoring^{1,2}, biochemistry³ and toxicology^{4,5}. Particularly, if the particles have sub-diffraction sizes (usually the scales are of tens nanometers which are below the resolution of the microscope) and are suspended in liquid environments, where the Brownian motion is present, a random movement resulting from the collisions of the liquid molecules. To accurately characterize these nanoobjects, electron microscopy (EM) is a possible option, but this remains challenging as it relies on complex microfluidic cells and still presents experimental difficulties⁶.

An alternative and commonly used technique for determining the size distribution of Brownian particles is dynamic light scattering (DLS), which is based on the measurement of scattered light intensity from an ensemble of diffusing particles⁷. It has been applied for analyses of colloids⁸, proteins⁹, and magnetic nanoparticles¹⁰. However, the main drawback of DLS is that the sensitivity is dominated by large-sized particles, even though they constitute only a small fraction of the size distribution, since the scattered intensity is proportional to the sixth power of the particle's diameter¹¹. Therefore, the accuracy is limited in measuring polydisperse suspensions of particles. Besides, in DLS measurements, high concentrations of nanoparticles are needed to obtain sufficient scattering intensity, which may require additional preprocessing of the samples, such as centrifugation.

In this context, nanoparticle tracking analysis (NTA) has been developed as an optical-based technique for the characterization of single nanoparticles in liquids. By using a standard optical microscope and CMOS camera, NTA can measure the movement rate—diffusion coefficient (D)—of the Brownian motion of the nanoparticle. In case the D is measured from the particle tracking experiment, the size of the nanoparticle can be calculated according to the Stokes-Einstein equation^{12,13}, which is associated with the absolute temperature and viscosity of the liquid. NTA is based on the detection of elastic light scattering, and thus can be applied to particles of different materials, such as metals, polymers, and biological matter. Particles are detectable as long as their scattering cross-section exceed that of the liquid medium, that is, the signal is above the background noise. NTA supports the real-time monitoring and accurate analysis of the size distribution for diffusing particles in a wide range of scales (from 10 nm to 1 μ m).

In recent years, NTA has become an emerging tool in numerous applications, including life science (e.g., the study of virus or cells¹⁴⁻²¹ and biological materials²²⁻²⁴), nanotechnology (e.g., nanomaterials characterization²⁵⁻²⁷) and nanomedicines (e.g., drug delivery^{28,29} and vaccines³⁰).

In contrast to DLS, a notable feature of NTA is the focus on individual trajectories of nanoparticles, making it possible to do particle-by-particle analysis, termed single particle tracking (SPT). Due to its ability to track and resolve the diffusion movement of single nanoobjects, SPT has played a key role in many cutting-edge biophysical researches such as single-molecule detection³¹⁻³³, membrane dynamics³⁴⁻³⁸ and anomalous diffusion studies³⁹⁻⁴¹. A widely used method in SPT to determine D from the trajectory of a Brownian particle is the mean square displacement (MSD)^{12,42,43}. The simplest case is the tracking of freely diffusing nanoparticles in an isotropic medium, where the displacements in a given time follow a Gaussian distribution and the MSD is a linear function as the lag times. The D can be determined by conducting a linear fitting to the calculated MSD. The MSD analysis taking into account the localization uncertainty arising from the video-based tracking experiment has been developed by Michalet, from which the theoretical expressions of MSD offset and error estimation as well as the optimal number of fitting lags are given^{44,45}.

Due to the stochastic nature of the MSD method, the retrieved D has an inherent statistical error that depends on the length of the trajectory (the number of captured frames N), even though the measurement of the position is infinitely precise⁴⁶. Typically, the relative standard deviation of the measured D follows $1/\sqrt{N}$, thus, obtaining long enough trajectories is one key requirement of the NTA experiment regarding statistical accuracy. However, this remains challenging, particularly for measuring nanoparticles with large D (small diameter), since if the object is not spatially restricted in the tracking area they can easily diffuse out of the illuminating volume or field of view (FoV) of the microscope, resulting a small number of captured frames and thus a reduced measurement accuracy.

Besides, in the detection of fluorescence-labeled nanoparticles, the frame rate is relatively low because of the large exposure time required to detect sufficient fluorescent photons, and the photobleaching also limits the total observation time. Alternative approaches that can overcome these drawbacks are to employ elastic light scattering, such as dark-field microscopy⁴⁷⁻⁵⁰ and interferometric scattering microscopy⁵¹ (iSCAT), enabling fast-tracking of label-free single nanoparticles. However, the mentioned techniques still suffer from the issues of being difficult to capture long trajectories or being limited by the time-varying background noise⁵². For example, in the case of free diffusion (particles are unconfined), the scattered intensity reduces as the particle moves away from the depth of focus of the microscope, leading to increased localization uncertainty. Therefore, to achieve high-speed, label-free, and high signal-to-noise ratio

(SNR) tracking of nanoparticles, a new scheme based on optical fiber and elastic light scattering was proposed by Faez et al.,⁵² termed as fiber-assisted nanoparticle tracking analysis (FaNTA).

1.2 Fiber-assisted Nanoparticle Tracking Analysis

With the development of fiber drawing technologies, microstructured optical fibers have been fabricated and widely used in many scientific researches. Thanks to its customization and specificity, the applications cover multiple fields such as optical communications⁵³⁻⁵⁵, laser systems⁵⁶⁻⁵⁹, fiber sensors⁶⁰⁻⁶⁶, nonlinear optics⁶⁷⁻⁷² and microfluidics⁷³⁻⁷⁸. Among them, optofluidic fiber with nanobore structure is naturally an ideal platform for NTA applications. A comparison of the conventional NTA and FaNTA is depicted in Fig. 1.1. The FaNTA approach in this study has unique features: (i) nanoparticle solution is filled into an externally accessible nanochannel in the core of a step-index optical fiber, and the guiding mode provides the illumination field to the samples; (ii) objective lens is perpendicularly placed with the fiber to collect the scattered light from nanoparticles; (iii) the dark-field illumination is established, thus the particles are imaged in a dark background (only the scattered light enters the objective), making it appropriate for obtaining the point spread functions of single nanoparticles.

In conventional NTA schemes, the nanoparticles are freely diffusing in a bulk medium, leading to the tracking duration being limited by the finite depth of field or illumination volume of the imaging system. For example, a 50 nm nanosphere in water ($D=8.6 \mu\text{m}^2/\text{s}$) has an in-focus observation time of 2 s by using an objective with 20x magnification and NA=0.4 (the depth of field $\sim 6 \mu\text{m}$). One possible solution is to construct an auto-focus imaging system to follow the object, but this requires the use of a fast-response mechanical system, increasing the cost of the experiment. The main benefit of FaNTA is that the nanochannel transversely restricts the mobile targets within the focal plane of the microscope, enabling continuous observation of typically tens seconds⁵². Furthermore, the FaNTA integrates both the optofluidic cell and dark-field illumination in a single fiber, providing a compact platform for NTA experiments. Also, the frame rate can be significantly increased (up to kHz) due to the high SNR and reduced FoV (only focusing on the part of the nanochannel). All of these advantages are difficult to achieve in conventional NTA setups.

1.3 Motivation of the Thesis

The original literature⁵² proposed and experimentally proved the working principle of the FaNTA approach based on nanofluidic optical fiber. The innovative method should be placed in the proper context, and the benefits of using the highly-confined

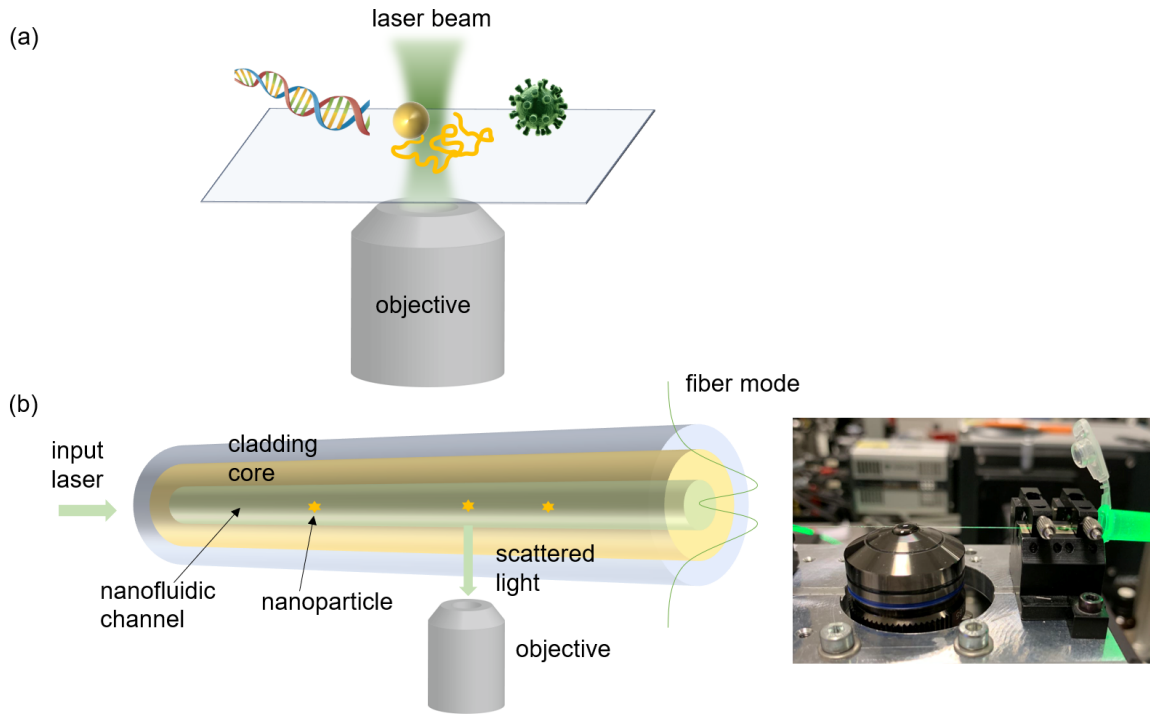


Figure 1.1: Comparison of classic NTA and FaNTA setups. (a) Sketch of a typical NTA setup, samples are placed on the focal plane of an objective lens, and illuminated with a laser beam. Nanoparticles such as viruses, metal nanospheres, or DNA molecules freely diffuse in liquid. (b) Sketch of the FaNTA setup, the sample solution (water) is confined in the nanofluidic channel of a step-index optical fiber and illuminated by an evanescent-shaped mode (due to the low refractive index of the liquid). Laterally scattered light is detected via an objective lens. The bottom right inset shows a photo of the experimental setup.

nanochannel as well as the intrinsic accuracy of the measurements need to be clarified. Therefore, the first task of the thesis is to demonstrate the capability of nanobore optical fiber in ultralong nanoparticle tracking. With a large number of frames from a single nanoparticle, it enables to quantification of the noise level and statistical accuracy of diffusion measurement, as well as the size determination.

Secondly, the FaNTA relies on the detection of elastic light scattering of the nanoparticle, and the signal intensity is proportional to the localized modal intensity within the illuminating domain (Rayleigh Scattering). A sketch to illustrate this issue is presented in Fig. 1.2. In the water-filled case, an evanescent field is formed in the nanochannel due to the low refractive index of water. One problem that arises from this process is that the brightness of the detected nanoparticles changes with the diffusive movement, and tracking may be interrupted once the target is at a location of low modal intensity. Therefore, generating a guided mode with spatial-invariant field distribution—a light strand—in the fluidic area is ideal for continuously observing nanoparticles with constant SNR. Another benefit of the flattened mode is unlocking the potential of FaNTA

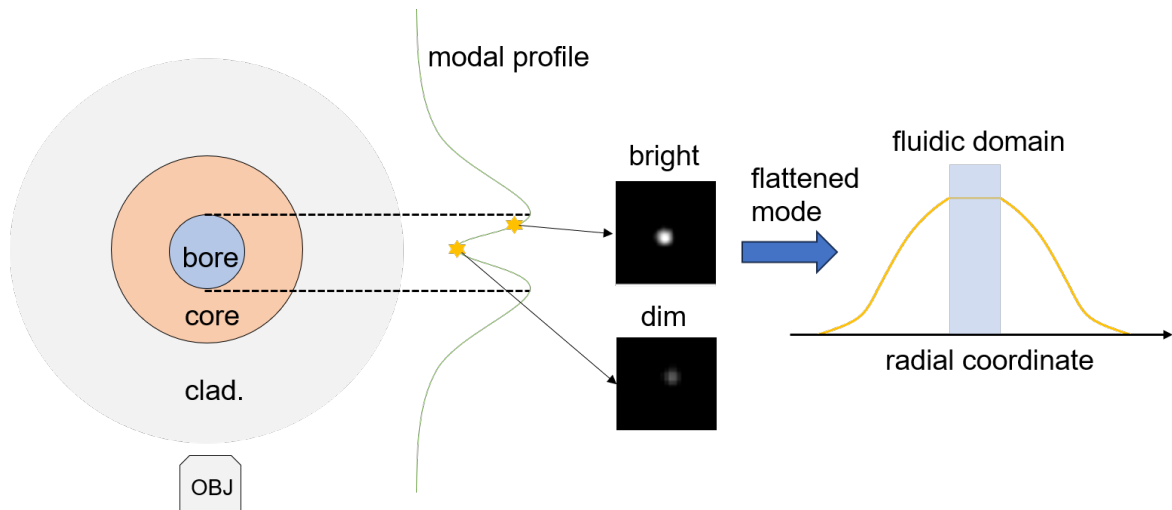


Figure 1.2: Sketch of FaNTA with flattened mode. In a water-filled nanochannel, the modal field is evanescent, leading to variant brightness of the imaged nanoparticle as the diffusive movement. A spatial-independent modal distribution is desired for continuous NTA measurement since the scattered intensity and SNR can remain constant.

for intensity-based experiments, such as the refractive index measurement or the rotational diffusion of non-spherical nanobjects. Therefore, this thesis has studied the general condition of the flat-field mode in optical fibers and demonstrated the constant intensity distribution through NTA experiments.

Finally, another possible route to obtain flattened fields in the fluidic domain is explored. The basic concept is the employment of a freely propagating Gaussian beam as the illumination and the intensity variation can be ignored in the micro-scaled channel. To achieve this purpose, any guiding modes need to be avoided. Hence, a capillary fiber is aligned with the launching beam, and placed in the nanoparticle solution that has the same refractive index as the glass, forming a homogeneous medium. This method not only offers a near-flat illumination but also the nanoparticles are restricted in the capillary, breaking through the flat-field condition that requires specified parameters (geometries or refractive indexes of liquids) of the microstructured optical fibers. Besides, the size of the capillary fiber is flexible to be chosen and integrated with an on-chip optofluidic platform, which paves new ways for applications in nanoparticle detection and the study of light-matter interactions.

1.4 Contents of the Thesis

Chapter 2: Fundamentals of optical fibers, specifically, step-index fiber and nanobore fiber (NBF), are described based on wave optics. The formation of flat modes is studied

from the theoretical and simulation perspectives. Brownian motion and MSD method, as well as the error analysis, are presented.

Chapter 3: The capability of ultralong tracking using NBF is experimentally demonstrated. With a large number of captured frames, the statistical accuracy of the diffusing measurement is qualified via performing MSD analysis on individual sub-trajectories, and the results are confirmed with theoretical prediction. The core benchmarks obtained from the FaNTA are compared with state-of-the-art approaches and the benefits are discussed.

Chapter 4: The flat-field condition in NBF is experimentally proved by performing NTA measurements. The modal distribution in a nanoscale domain, which is difficult to resolve by image-based measurement, can be retrieved through a statistical histogram analysis. Furthermore, with the benefit of the designed analysis, the subtle transitions of the mode shapes, Gaussian-flat-evanescent, can also be determined, which is implemented by controlling the temperature of the fiber.

Chapter 5: A novel on-chip optofluidic fiber device with flat-field illumination is explored. The designed chip aims at the use of core- and mode-less fiber configuration and straightforward employment of Gaussian beam for illuminating the nanoobjects in the microscale fluidic channel. The excellent performance in NTA application is experimentally demonstrated. Similarly, the same analysis method is used to determine the light intensity distribution within the fluidic area.

Chapter 6: The achievements of the thesis are summarized, and the outlook studies originating from the results are pointed out.

1.5 Highlight of the Contributions

The main contributions of the thesis are listed below:

- It reveals the ability of FaNTA in dynamic monitoring of nanoobjects with ultralong time and high localization accuracy, which has been close to the theoretical limit.
- The focal depth of FaNTA experiments is increased by employing the flattened fiber mode, allowing a constant illumination field in all three dimensions.
- The designed fiber-assisted optofluidic device unlocks the spatial limitation of the optical core in fibers while supporting the ultralong observation of nanoparticles with nearly flat illumination.
- The results extend the application prospects of FaNTA in many scientific fields, such as biochemistry sensing, nanomaterials science, and the fundamental study of light-matter interactions.

2 | Fundamentals of Fiber Optics and NTA

2.1 Introduction to Optical Fiber

Optical fibers are typically flexible and transparent strands that are made of glass or plastic materials, which can be used to transmit light waves over long distances. The simplest case is step-index optical fiber consisting of a core-cladding structure where the core has a higher refractive index (RI) than the cladding. The total internal reflection occurs on the interface and the light is confined in the core region, forming the guided modes. With the development of the fiber drawing technique, more and more optical fibers with complex structures are manufactured, including NBFs, hollow core fibers (HCFs), and photonic crystal fibers (PCFs). These fibers with special structures and functions greatly broaden their applications in sensing, optical communication, and nonlinear optics. In this section, the fundamentals of step-index optical fiber and NBF as well as their mode properties are discussed.

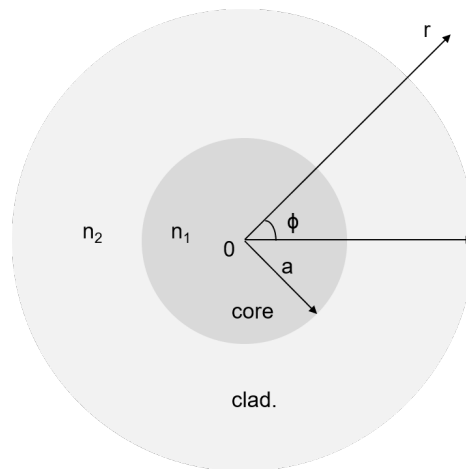


Figure 2.1: Sketch of the step-index fiber. The refractive indexes of the core and cladding are noted as n_1 and n_2 . The radial and azimuthal coordinates are noted as r and ϕ . The radius of the core is a .

2.1.1 Step-index Optical Fiber

The sketch of step-index fiber in cylindrical coordinates is shown in Figure 2.1. The time-harmonic guiding mode can be written as $\psi = \psi(r, \phi)\exp[i(\beta z - \omega t)]$, where $\beta = k_0 n_{\text{eff}}$ is the propagation constant, $k_0 = 2\pi/\lambda$ is the wave number, n_{eff} is the

effective mode index and ω is the angular frequency. Starting from Maxwell's equations, $\nabla \times \vec{\mathbf{E}} = i\omega\mu_0\vec{\mathbf{H}}$ and $\nabla \times \vec{\mathbf{H}} = -i\omega\epsilon_0\epsilon\vec{\mathbf{E}}$, the transverse fields can be derived

$$E_\phi = \frac{i\beta}{k_0^2\epsilon - \beta^2} \left(\frac{1}{r} \frac{\partial E_z}{\partial \phi} - \frac{\omega\mu_0}{\beta} \frac{\partial H_z}{\partial r} \right) \quad (2.1)$$

$$E_r = \frac{i\beta}{k_0^2\epsilon - \beta^2} \left(\frac{\partial E_z}{\partial r} + \frac{\omega\mu_0}{\beta r} \frac{\partial H_z}{\partial \phi} \right) \quad (2.2)$$

$$H_\phi = \frac{i\beta}{k_0^2\epsilon - \beta^2} \left(\frac{1}{r} \frac{\partial H_z}{\partial \phi} + \frac{\omega\epsilon_0\epsilon}{\beta} \frac{\partial E_z}{\partial r} \right) \quad (2.3)$$

$$H_r = \frac{i\beta}{k_0^2\epsilon - \beta^2} \left(\frac{\partial H_z}{\partial r} - \frac{\omega\epsilon_0\epsilon}{\beta r} \frac{\partial E_z}{\partial \phi} \right) \quad (2.4)$$

where $\epsilon = n^2$ is the dielectric constant of the materials. It shows that the problem now is to solve the field components E_z and H_z , which both satisfy the wave equation

$$\left[\frac{1}{r} \frac{\partial}{\partial r} \left(r \frac{\partial}{\partial r} \right) + \frac{1}{r^2} \frac{\partial^2}{\partial \phi^2} + (k_0^2 n^2 - \beta^2) \right] \psi = 0, \quad (2.5)$$

where $\psi = [E_z, H_z]^T$. The above equation can be solved by using the separation of variables so that the solution is supposed as $\psi(r, \phi) = R(r)\Phi(\phi)$, then the wave equation can be written as

$$-\frac{1}{\Phi(\phi)} \frac{d^2\Phi(\phi)}{d\phi^2} = m^2 \quad (2.6)$$

$$\frac{r}{R(r)} \frac{d}{dr} \left[r \frac{dR(r)}{dr} \right] + (k_0^2 n^2 - \beta^2) r^2 = m^2 \quad (2.7)$$

where m is the azimuth index. The solution of Eq. 2.6 can be expressed as $\Phi(\phi) = \sin(m\phi)$ or $\Phi(\phi) = \cos(m\phi)$. Eq. 2.7 is a Bessel equation and the solution is called the Bessel function. The solutions that agree with the guiding mode in the fiber can be expressed as

$$\begin{cases} E_z^1 = AJ_m(k_1 r) \sin(m\phi), & 0 < r < a \\ E_z^2 = BK_m(k_2 r) \sin(m\phi), & a < r \\ H_z^1 = CJ_m(k_1 r) \cos(m\phi), & 0 < r < a \\ H_z^2 = DK_m(k_2 r) \cos(m\phi), & a < r \end{cases} \quad (2.8)$$

where A, B, C, D are constants. $k_1 = k_0 \sqrt{n_1^2 - n_{\text{eff}}^2}$ and $k_2 = k_0 \sqrt{n_{\text{eff}}^2 - n_2^2}$. The superscript (E) and subscript (k) refer to the regions: 1-core; and 2-cladding. J_m and K_m are the first and second kind Bessel functions, describing the radial profiles of the mode in the core and cladding. According to the definitions of k_1 and k_2 , The guiding modes condition of the fiber should satisfy $n_2 < n_{\text{eff}} < n_1$. Some related parameters are defined as

$$U = ak_1 = k_0 a \sqrt{n_1^2 - n_{\text{eff}}^2} \quad (2.9)$$

$$W = ak_2 = k_0a\sqrt{n_{\text{eff}}^2 - n_2^2} \quad (2.10)$$

$$V = \sqrt{U^2 + W^2} = k_0a\sqrt{n_1^2 - n_2^2}. \quad (2.11)$$

To determine the n_{eff} , put Eq. 2.8 into Eqs. 2.1 \sim 2.4, and then apply the continuity boundary conditions: tangential components are equivalent on the interface ($r = a$)

$$E_z^1 = E_z^2; H_z^1 = H_z^2; E_\phi^1 = E_\phi^2; H_\phi^1 = H_\phi^2. \quad (2.12)$$

The boundary conditions will produce four algebraic equations with respect to the coefficients A, B, C, D , and then the eigenequation of the guided mode can be derived as

$$\left[\frac{J'_m(U)}{UJ_m(U)} + \frac{K'_m(W)}{WK_m(W)} \right] \left[n_1^2 \frac{J'_m(U)}{UJ_m(U)} + n_2^2 \frac{K'_m(W)}{WK_m(W)} \right] = m^2 n_{\text{eff}}^2 \left(\frac{V}{UW} \right)^4. \quad (2.13)$$

The effective mode index n_{eff} can be numerically solved from the above equations if the fiber parameters n_1, n_2 , and a are specified. The n_{eff} of the fundamental mode (HE_{11}) as function of the wavelength is shown in Fig. 2.2.

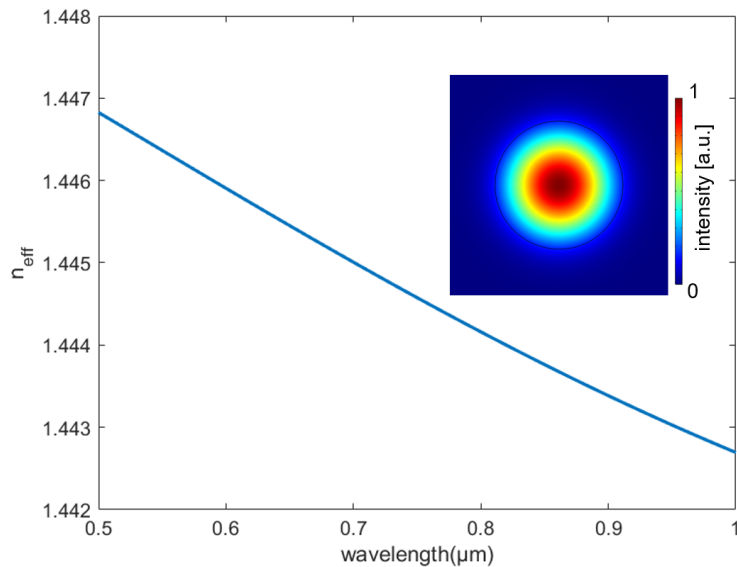


Figure 2.2: The calculated n_{eff} of the fundamental mode as a function of the wavelength with $n_1 = 1.45$, $n_2 = 1.44$ and $a = 1.5 \mu\text{m}$. The inset shows the modal distribution at the wavelength of 600 nm.

In practical applications, the optical fibers commonly have small refractive index contrasts, that is, $(n_1 - n_2)/n_1 \ll 1$, which are called weakly guiding waveguides. In this approximation, the longitudinal components of the fields are negligible compared to the transversal components, which means the modes are nearly TEM waves and linear polarized (LP-mode)⁷⁹. The fundamental mode in this case is termed LP_{01} ($m = 0$).

2.1.2 Nanobore Optical Fiber

In this thesis, NTA experiments are performed based on nanobore optical fiber (NBF). The NBF has a nanoscale channel penetrating along the z -axis of a step-index optical fiber, forming a 3-layer concentric structure (bore-core-cladding). The cross-section of the NBF is shown in Fig. 2.3, where the refractive indexes are noted as n_1 , n_2 , and n_3 corresponding to the bore, core, and cladding, respectively. Similar to step-index optical fiber, the working principle of NBF is also based on internal total reflection, but it allows different types of modes that depend on the RI of the channel. On the one hand, if the RI is lower than the core, such as air or water, the mode is evanescent in the channel, appearing as a hollow core distribution. On the other hand, if the channel is filled with high RI liquids, e.g., DMSO, the mode possesses an enhanced Gaussian distribution and most of the field energy will be confined in the fluidic channel.

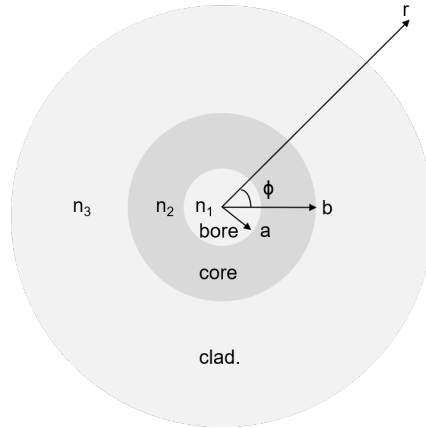


Figure 2.3: Sketch of the NBF cross-section. The refractive indexes of the bore, core, and cladding are noted as n_1 , n_2 , and n_3 . a and b refer to the radius of the bore and core, respectively.

Theoretical analysis of NBF is similar to step-index fiber, and the general solutions of the radial profiles of the modes in the core can be expressed as the sum of Bessel functions $J_m(k_2r)$ and $Y_m(k_2r)$. The fields in the bore and cladding are proportional to $J_m(k_1r)$ and $K_m(k_3r)$, respectively. The azimuthal term of the electric field is supposed to be $\sin(m\phi)$ and that of the magnetic field is $\cos(m\phi)$, thus the expressions of the mode fields in the corresponding layers are

$$\left\{ \begin{array}{ll} E_z^1 = AJ_m(k_1r)\sin(m\phi), & 0 < r < a \\ E_z^2 = [CJ_m(k_2r) + DY_m(k_2r)]\sin(m\phi), & a < r < b \\ E_z^3 = GK_m(k_3r)\sin(m\phi), & b < r \\ H_z^1 = BJ_m(k_1r)\cos(m\phi), & 0 < r < a \\ H_z^2 = [EJ_m(k_2r) + FY_m(k_2r)]\cos(m\phi), & a < r < b \\ H_z^3 = HK_m(k_3r)\cos(m\phi), & b < r \end{array} \right. \quad (2.14)$$

where $k_1 = k_0\sqrt{n_1^2 - n_{\text{eff}}^2}$, $k_2 = k_0\sqrt{n_2^2 - n_{\text{eff}}^2}$ and $k_3 = k_0\sqrt{n_{\text{eff}}^2 - n_3^2}$, note here is assumed $n_3 < n_{\text{eff}} < n_1$. According to the continuity boundary conditions we have

$$\begin{aligned} E_z^1 &= E_z^2, & H_z^1 &= H_z^2, & r &= a, \\ E_z^2 &= E_z^3, & H_z^2 &= H_z^3, & r &= b, \\ E_\phi^1 &= E_\phi^2, & H_\phi^1 &= H_\phi^2, & r &= a, \\ E_\phi^2 &= E_\phi^3, & H_\phi^2 &= H_\phi^3, & r &= b. \end{aligned} \quad (2.15)$$

Put Eq. 2.14 into Eqs. 2.1-2.4, and apply the boundary conditions Eq. 2.15, a series of linear equations for the coefficients from A to H can be obtained. This set of algebraic equations can be rearranged into a matrix equation $M\vec{X} = 0$, where $\vec{X} = [A, B, C, D, E, F, G, H]^T$. The non-zero solution of \vec{X} requires the determinant of the coefficients matrix to be zero, which yields

$$\det[M] = 0, \quad (2.16)$$

where the elements of the matrix M are written as below

$$\begin{bmatrix} J_1 & 0 & -J_a & -Y_a & 0 & 0 & 0 & 0 \\ 0 & J_1 & 0 & 0 & -J_a & -Y_a & 0 & 0 \\ \frac{m}{a}Q_1J_1 & -\frac{\omega\mu_0}{\beta}Q_1J'_1 & -\frac{m}{a}Q_2J_a & -\frac{m}{a}Q_2Y_a & \frac{\omega\mu_0}{\beta}Q_2J'_a & \frac{\omega\mu_0}{\beta}Q_2Y'_a & 0 & 0 \\ \frac{\omega\epsilon_0\epsilon_1}{\beta}Q_1J'_1 & -\frac{m}{a}Q_1J_1 & -\frac{\omega\epsilon_0\epsilon_2}{\beta}Q_2J'_a & -\frac{\omega\epsilon_0\epsilon_2}{\beta}Q_2Y'_a & \frac{m}{a}Q_2J_a & \frac{m}{a}Q_2Y_a & 0 & 0 \\ 0 & 0 & J_b & Y_b & 0 & 0 & -K_3 & 0 \\ 0 & 0 & 0 & 0 & J_b & Y_b & 0 & -K_3 \\ 0 & 0 & \frac{m}{b}Q_2J_b & \frac{m}{b}Q_2Y_b & -\frac{\omega\mu_0}{\beta}Q_2J'_b & -\frac{\omega\mu_0}{\beta}Q_2Y'_b & -\frac{m}{b}Q_3K_3 & \frac{\omega\mu_0}{\beta}Q_3K'_3 \\ 0 & 0 & \frac{\omega\epsilon_0\epsilon_2}{\beta}Q_2J'_b & \frac{\omega\epsilon_0\epsilon_2}{\beta}Q_2Y'_b & -\frac{m}{b}Q_2J_b & -\frac{m}{b}Q_2Y_b & -\frac{\omega\epsilon_0\epsilon_3}{\beta}Q_3K'_3 & \frac{m}{b}Q_3K_3 \end{bmatrix}. \quad (2.17)$$

The symbols in the matrix are defined below

$$\begin{aligned} Q_j &= \frac{i\beta}{k_0^2n_j^2 - \beta^2} (j = 1, 2, 3), \\ J_1 &= J_m(k_1a), & J'_1 &= \frac{m}{a}J_m(k_1a) - k_1J_{m+1}(k_1a), \\ J_a &= J_m(k_2a), & J'_a &= \frac{m}{a}J_m(k_2a) - k_2J_{m+1}(k_2a), \\ J_b &= J_m(k_2b), & J'_b &= \frac{m}{b}J_m(k_2b) - k_2J_{m+1}(k_2b), \\ Y_a &= Y_m(k_2a), & Y'_a &= \frac{m}{a}Y_m(k_2a) - k_2Y_{m+1}(k_2a), \\ Y_b &= Y_m(k_2b), & Y'_b &= \frac{m}{b}Y_m(k_2b) - k_2Y_{m+1}(k_2b), \\ K_3 &= K_m(k_3b), & K'_3 &= \frac{m}{b}K_m(k_3b) - k_3K_{m+1}(k_3b). \end{aligned} \quad (2.18)$$

Combining Eqs. 2.17 and 2.18 with Eq. 2.16, it will give a transcendental equation with respect to n_{eff} , which can be numerically solved once the fiber parameters and operating wavelength are defined. The fundamental mode of NBF could have either a Gaussian ($n_{\text{eff}} > n_1$) or an evanescent modal distribution ($n_{\text{eff}} < n_1$, substitute $J_m(k_1r)$ into $I_m(k_1r)$ in this case.).

The distribution of propagating modal intensity is given by the time-averaged Poynting vector

$$S_z = \text{Re}[\vec{\mathbf{E}} \times \vec{\mathbf{H}}]_z. \quad (2.19)$$

In addition, the theoretical analysis for a multi-layer structured fiber (Bragg fiber) will yield a matrix equation with a larger scale and the calculation is more cumbersome. In that case, an effective method based on the transfer matrix could be used⁸⁰.

Finite Element Method Simulation

The analytical solutions are difficult to obtain if the optical fibers have complex structures. In these cases, a commonly used method to study the mode properties is the numerical simulation based on the finite element method (FEM). The basic concept of FEM is the discretization (a mesh) of the geometries, and the associated boundary value problem can be solved via numerical algorithms⁸¹. In the simulation of optical fibers, the wave equation in the defined materials and boundaries is solved, and the eigenvalues of the modes (n_{eff}), as well as the full components of the electromagnetic fields, are computed. The commercial FEM software COMSOL Multiphysics is used in this thesis for the mode calculations for optical fibers.

2.2 Introduction to Brownian Motion

In 1827, the botanist Robert Brown observed that small particles suspended in liquids were doing random motion while he was studying pollen grains with a microscope, then such motion was firstly called Brownian motion¹³. It was proved that this motion was not caused by microorganisms, because this kind of behavior could be still observed from some inorganic particles. In 1905, Albert Einstein published his famous paper and explained the stochastic nature of Brownian motion based on molecular-kinetic theory where the motion of the Brownian particle refers to the collisions of the surrounding fluid molecules¹², which connects the microscopically molecular motions and measurable diffusion rate. In the next hundred years, the mechanism of Brownian motion not only promotes many theoretical developments for statistical physics^{13,82}, chaotic system⁸³ and fluid mechanics^{84,85} but also plays an important role in many application fields, such as soft matters^{86,87}, life science^{88,89} and biophysics⁹⁰.

The next sections will discuss the mathematical descriptions of Brownian motion, the diffusion equation, and the measurement of the random trajectory of the particle, the data analysis methods including mean square displacement (MSD) and power spectra density (PSD).

2.2.1 Diffusion Equation

To describe Brownian motion, Einstein derived that the probability density function (PDF) of the Brownian particle in free space should satisfy the diffusion equation¹²

$$\frac{\partial}{\partial t} f(x, t) = D \frac{\partial^2}{\partial x^2} f(x, t), \quad (2.20)$$

where $f(x, t)$ is the PDF in the one-dimensional case, representing the probability of finding the particle at the position x and given time t . D is the diffusion coefficient which is given by the Stokes-Einstein equation for the case of a spherical particle in a liquid with a low Reynolds number

$$D = \frac{K_B T}{6\pi\eta r}, \quad (2.21)$$

where K_B is Boltzmann constant, T is the absolute temperature, η is the viscosity of the liquid and r is the hydrodynamic radius of the particle. This relation is the foundation of the particle tracking analysis since it established a bridge between the properties of the liquid and the measurable quantity D . For example, the radius of the particle can be calculated when the values of D , T , and η are known.

With the initial condition $f(x, t = 0) = \delta(x - x_0)$, the solution of the diffusion equation is given by

$$f(x, t) = \frac{1}{\sqrt{4\pi Dt}} \exp\left[-\frac{(x - x_0)^2}{4Dt}\right], \quad (2.22)$$

showing that the PDF is a Gaussian distribution with the initial position of the particle defined as x_0 . According to the probability theory, the mathematical expectation of an arbitrary function $g(x, t)$ of the random variable x can be calculated by integrating the product with the PDF $f(x, t)$, which states

$$\langle g(t) \rangle = \int_{-\infty}^{\infty} g(x, t) f(x, t) dx, \quad (2.23)$$

the brackets $\langle \rangle$ denote the ensemble average in the whole space. In the above results, the diffusion coefficient D is the key parameter that refers to the velocity of Brownian motion, which can be measured from NTA experiments. One of the commonly used approaches to retrieve D is based on the MSD method, from which the MSDs are calculated and fitted for each trajectory of individual nanoparticles. In the next sections, the theoretical derivations of MSD, including the completed expressions taking into account the motion blur and exposure effect in video-based tracking, as well as the error analysis are discussed.

2.2.2 Mean Square Displacement

MSD is one commonly used statistical method to measure the D of a particle with Brownian motion based on its position information. The definition of MSD is

$$\text{MSD}(t) = \langle [x(t) - x_0]^2 \rangle = \frac{1}{N} \sum_{i=1}^N [x(t) - x(0)]_i^2, \quad (2.24)$$

where N is the number of frames recorded from the moving particle, $x(0)$ and $x(t)$ represent the initial position of the particle and the next position after the lag time t , respectively. To calculate D from MSD, it can be expanded as

$$\begin{aligned} \text{MSD} &= \langle (x - x_0)^2 \rangle \\ &= \langle x^2 \rangle + x_0^2 - 2x_0 \langle x \rangle. \end{aligned} \quad (2.25)$$

Now the task is to calculate the average of x and x^2 . One can directly calculate them by using Eqs. 2.22 and 2.23, another way is to apply the moment-generating function to find out the k -th moment of PDF, which is exactly what we need. For the first step, calculate the integral

$$\begin{aligned} \langle \exp(ikx) \rangle &= \frac{1}{\sqrt{4\pi Dt}} \int_{-\infty}^{\infty} \exp(ikx) \exp\left[-\frac{(x-x_0)^2}{4Dt}\right] dx \\ &= \exp[(ikx_0 - k^2Dt)], \end{aligned} \quad (2.26)$$

then expand e^{ikx} by the Taylor series and take the average bracket

$$\langle \exp(ikx) \rangle = 1 + ik \langle x \rangle + \frac{(ik)^2}{2} \langle x^2 \rangle + \dots, \quad (2.27)$$

take the natural logarithm on both sides of the above equation

$$\begin{aligned} \ln \langle \exp(ikx) \rangle &= \ln \left[1 + ik \langle x \rangle + \frac{(ik)^2}{2} \langle x^2 \rangle + \dots \right] \\ &= i \langle x \rangle k + \frac{i^2}{2} \langle x^2 \rangle k^2 - \frac{i^2}{2} \langle x \rangle^2 k^2 + \dots, \end{aligned} \quad (2.28)$$

from Eq. 2.26, it has been known that

$$\ln \langle \exp(ikx) \rangle = ikx_0 - k^2Dt, \quad (2.29)$$

compare the coefficients of the same power of k in Eqs. 2.28 and 2.29, to yield

$$\langle x \rangle = x_0, \quad (2.30)$$

$$\langle x^2 \rangle = 2Dt + x_0^2, \quad (2.31)$$

insert Eqs. 2.30 and 2.31 into Eq. 2.25 then we can get the expression of MSD

$$\text{MSD}(t) = 2Dt. \quad (2.32)$$

It shows that MSD is linearly proportional to t when the particle is freely diffusing, where the D can be obtained from the slope of a linear fitting to MSD as a function of the lag time. For cases of higher dimensions, the spatial coordinates are independent, thus it can be derived that

$$\text{MSD}(t) = 2dDt. \quad (2.33)$$

where d is the dimensional index, $d = 1, 2, 3$ respectively for the 1-D, 2-D and 3-D cases. In the next sections, the microscope-based particle tracking experiment will be discussed, which includes the point spread function (PSF) and error analysis.

2.2.3 Video-based Tracking and Error Analysis

The tracking of a single particle is based on the microscope-camera system, from which one can record a video of the moving particle and then extract the trajectory (particle's position as a function of time) by using image processing frame by frame⁴⁴. MSD of the discrete data can be calculated as below

$$\text{MSD}(n\Delta t) = \frac{1}{N-n} \sum_{i=1}^{N-n} [x((i+n)\Delta t) - x(i\Delta t)]^2 \quad (2.34)$$

where Δt is the frame time of the camera, N is the length of the trajectory, $n\Delta t$ represents the lag time of MSD ($n=1, 2, 3, \dots, N-1$). The series of $x(i\Delta t)$ are obtained from the image processing program, and i refers to the index of each frame. The slope of a linear fitting to the calculated MSD points as a function of lag times gives the values of D ($D=\text{slope}/2d$, d is the dimensional index). It is worth noting that the optimal number of lags in the MSD fitting depends on the localization uncertainty (offset of MSD curve, e.g., the first two lags are used in case the offset is negligible), which has been discussed in detail in the reference⁴⁴. For each trajectory, the longer the length leads to the higher precision of the estimation on diffusion coefficient⁹¹ since the standard deviation of fitted D is roughly proportional to $1/\sqrt{N}$.

Dynamic Localization Uncertainty Induced MSD Offset

In the measurement of the particle position, localization error arises from the optical diffraction limit and diffusing movement, leading to the offset in MSD. The image of a point light emitter, such as a nanoparticle, behaves like the airy disk on the focal plane

of the microscope, which means the real object has been blurred as a light spot described by the PSF. In the particle tracking experiment under the standard microscope system, a good approximation of the PSF is expressed as Gaussian function⁴⁴

$$I(x, y) = I_0 \exp \left[-\frac{(x - x_0)^2 + (y - y_0)^2}{2s_0^2} \right], \quad (2.35)$$

where I_0 is the peak intensity of the light spot and (x_0, y_0) is the mass center of the particle in the frame. s_0 represents the standard deviation of the Gaussian distribution and can be determined by

$$s_0 = 0.21 \frac{\lambda}{\text{NA}}, \quad (2.36)$$

where λ is the working wavelength and NA is the numerical aperture of the objective lens. It indicates that the actual position of the particle cannot be determined within the area of s_0 due to the optical diffraction limit, shown in Fig. 2.4, even though the mass center of the PSF is assumed as the measured position. The localization uncertainty of

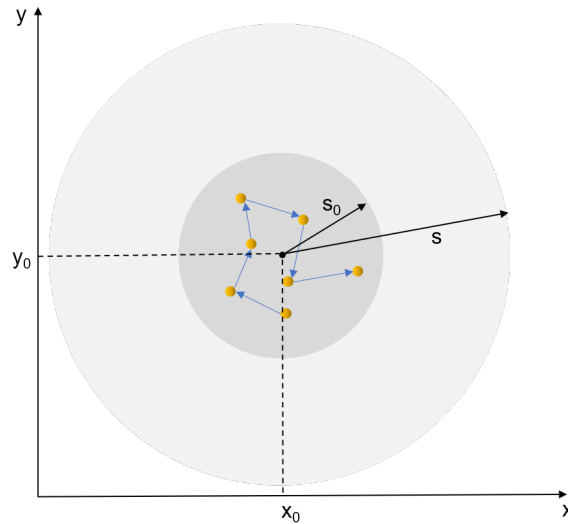


Figure 2.4: Schematic of the localization uncertainty in particle tracking analysis. Due to the optical diffraction, the image of a static nanoparticle on the focal plane is a light spot, described as the Gaussian PSF in Eq. 2.35, with a standard deviation of s_0 (illustrated in the central area), whereas a diffusing nanoparticle leads to a broadened PSF in the exposure time of the camera, depicted as the outer region. The standard deviation of the broadened PSF is noted as s .

a static particle, neglecting the readout noise of the camera, can be described by using the width of PSF s_0 ⁴⁴

$$\sigma_0 = \frac{s_0}{\sqrt{N_{\text{ph}}}}, \quad (2.37)$$

where N_{ph} represents the number of detected photons within the PSF, which can be calculated by the product of the camera gain and the intensity counts in the frame⁹².

Compared with a static nanoparticle, the mobile objects will broaden the PSF ($s_0 \rightarrow s$, see Fig. 2.4) in the finite exposure time. For a fixed exposure time (the captured photons number remains the same), diffusion leads to a lower peak intensity I_0 (larger s_0) of the PSF, the localization uncertainty will accordingly increase. The increased standard deviation of PSF introduces additional errors in the determination of particle position, which is called the dynamic localization uncertainty⁴⁴. Taking into account the broadening of PSF caused by both diffraction and diffusion, the so-called dynamic localization uncertainty can be expressed as⁴⁴

$$\sigma = \frac{s}{\sqrt{N_{\text{ph}}}} = \sigma_0 \sqrt{1 + \frac{Dt_E}{s_0^2}}, \quad (2.38)$$

where D is the diffusion coefficient and t_E is the exposure time per frame. On one hand, if the particle is fast diffusing (D is large), $\sigma \approx \sqrt{Dt_E/N_{\text{ph}}}$, the diffusion is dominant to the localization uncertainty; on the other hand, when the diffusion is slow, $\sigma \approx \sigma_0$, the diffraction limit is dominant. In MSD analysis, the localization uncertainty will contribute to the offset of MSD, which has been derived out, and the modified MSD is given by⁴⁴

$$\text{MSD}(t) = 2d(Dt + \sigma^2). \quad (2.39)$$

It indicates that the MSD has a positive offset when the localization uncertainty is not neglected.

Exposure Induced MSD Offset

In the video-based particle tracking experiments, one should consider another type of contribution to the MSD offset, which is called the motion blur (or the microsteps) due to the exposure time of the camera⁴⁴. An intuitive explanation of this effect is that the measured position is obtained by calculating the average of the microsteps during the finite exposure time t_E . In general cases when the frame time $\Delta t \geq t_E$, this effect is counted into a parameter named as the reduced square localization error⁴⁵

$$x = \frac{\sigma^2}{D\Delta t} - \frac{t_E}{3\Delta t}. \quad (2.40)$$

Taking into account the exposure effect, the completed expression of MSD is given by

$$\begin{aligned} \text{MSD}(t) &= 2dD\Delta tx + 2dDt \\ &= 2d \left(\sigma^2 - \frac{Dt_E}{3} \right) + 2dDt. \end{aligned} \quad (2.41)$$

It shows that the exposure time provides a negative contribution to the MSD offset, for instance, if the particle is under a well-optimized imaging system (small σ) and the

diffusion is fast, then one can get a negative-offset MSD curve, which has been observed in the publication of fiber-assisted particle tracking with ultralong trajectory⁹¹.

Errors of Determined Diffusion Coefficient

MSD is a statistical method to extract the diffusion coefficient D from the recorded positions of nanoparticles. In statistics, the lower limit of the errors for an unbiased estimator can be calculated quantitatively according to the Cramér–Rao lower bound (CRLB), which is the theoretical limit that none of the estimating methods can have beyond precision. In the case of MSD fitting, an approximation, taking into account both the dynamic localization uncertainty and exposure effect, of the relative standard deviation of the measured D has been given by Michalet⁴⁵

$$\frac{S(D)}{D} \geq \sqrt{\frac{2}{d(N-1)}} \left(1 + 2\sqrt{1+2x}\right)^{\frac{1}{2}}, \quad (2.42)$$

where d is the dimensional index, N is the length of the particle trajectory, x is defined in Eq. 2.40, and note that the value of x should not be too large (compared to 1) when this expression is used.

The Number of Lags for MSD Fitting

CRLB has quantified the theoretical limit of the errors arising from MSD analysis, and the limit is correlated to the number of lags in MSD fitting. In the estimation of D , a linear fitting to the MSD curve using unweighted least-square fit (LSF) achieves the best output (the error on D is minimized) in case the number of lags is chosen correctly. Here a simple empirical formula can be used to determine the optimal number of lags^{44,45}

$$p_{min} = E(2 + 2.3x^{0.52}), \quad (2.43)$$

where $E(\cdot)$ represents the round down to the closet integer. Note that this equation is based on the prior knowledge of x defined in Eq. 2.40, from which the expected value of D and imaging parameters should be known. If there is none of the prior knowledge, p_{min} can be determined by an iterative method described in the reference⁴⁵.

Random Walk Simulation with Microsteps

The trajectory of Brownian motion in free space can be simulated by using random walk based on random number generation algorithm. The process for one-dimensional cases is described as

$$\begin{cases} \tilde{x}_{i+1} = \tilde{x}_i + \Delta x_i \\ x_{i+1} = \tilde{x}_{i+1} + \chi_i \end{cases} \quad (2.44)$$

where \tilde{x}_i is the real position of the particle at the i -th step, $\Delta x_i \sim N(0, \sqrt{2D\Delta t})$ is the displacement governed by the normal distribution, x_{i+1} is the observed position which has been deviated by the localization uncertainty $\chi_i \sim N(0, \sigma)$. As discussed before, the exposure effect (motion blur) can be simulated by introducing the microsteps between the previously defined i and $i + 1$ steps and calculating the averaged position⁴⁴

$$\begin{aligned}\tilde{x}_q^{(i)} &= \frac{1}{q} \left[\tilde{x}_i + (\tilde{x}_i + \Delta x_1^{(i)}) + \dots + (\tilde{x}_i + \Delta x_1^{(i)} + \dots + \Delta x_{q-1}^{(i)}) \right] \\ &= \tilde{x}_i + \sum_{j=1}^{q-1} \frac{q-j}{q} \Delta x_j^{(i)},\end{aligned}\quad (2.45)$$

where q is the number of microsteps counted in the exposure time t_E and the superscript (i) refers to the i -th measurement, and $q = mt_E/\Delta t$ where m is the number of microsteps in the frame time ($\Delta t > t_E$). The duration per microstep is $\delta t = \Delta t/m$, and $\Delta x_j^{(i)} \sim N(0, \sqrt{2D\delta t})$. Then the observed position at the (i) -th measurement can be obtained by adding the localized uncertainty

$$\bar{x}_q^{(i)} = \tilde{x}_q^{(i)} + \chi_i. \quad (2.46)$$

Note that the starting position of the real trajectory in the next measurement $(i + 1)$ should be updated into

$$\tilde{x}_{i+1} = \tilde{x}_i + \sum_{j=1}^m \Delta x_j^{(i)}. \quad (2.47)$$

As shown in Fig. 2.5, the simulations with microsteps indicate that the offset of MSD fitting can be positive or negative, depending on the contributions of both localization uncertainty and motion blur, the value of x , that is, the offset is positive when $x > 0$, or negative when $x < 0$.

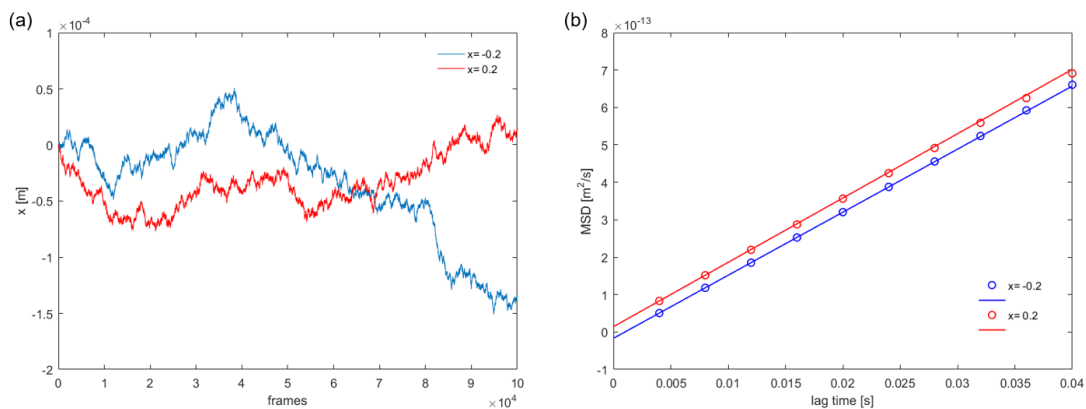


Figure 2.5: Simulation results of the random walk taking into account the microsteps. (a) simulated trajectories of the cases: $x = -0.2$ and $x = 0.2$. (b) Calculated MSD and the corresponding fittings for the trajectories in (a).

2.2.4 Power Spectral Density Method

In addition to MSD, the diffusion coefficient of a Brownian particle can be extracted by an alternative approach named power spectral density (PSD)⁹³. In the case of a spherical particle, the trajectory (1-D) $x(t)$ satisfies the Langevin equation

$$\gamma_0 x'(t) + \kappa x(t) = (2k_B T \gamma_0)^{1/2} F(t), \quad (2.48)$$

where $\gamma_0 = 6\pi\eta r$ is the friction coefficient, η is the viscosity, $\kappa x(t)$ is the harmonic trap force, $F(t)$ represents a Gaussian process of random force in Brownian motion, having $\langle F(t) \rangle = 0$ and $\langle F(t)F(t-t_0) \rangle = \delta(t_0)$.

Take Fourier transformation on both sides of the equation and combining the properties of $F(t)$, the PSD of $x(t)$ is obtained

$$P(f) = |\mathcal{F}(x(t))|^2 = \frac{D}{2\pi^2(f_c^2 + f^2)}, \quad (2.49)$$

where \mathcal{F} represents the Fourier transform, $f_c = \kappa/2\pi\gamma_0$ is called corner frequency, and it refers to the magnitude of the trapping force, which is explicit in, for instance, optical tweezers, or it tends to zero if the particle is freely diffusion.

In actual measurements, the motion blur leads to an averaged effect on the localization of nanoparticles, equivalently, the observed position can be approximately described as a convolution between the real trajectory and boxcar function^{94,95} of the exposure time. In frequency domain, the PSD is modified by multiplying $\text{sinc}^2(\pi f t_E)$

$$P_B(f) = \frac{D}{2\pi^2(f_c^2 + f^2)} \frac{\text{sin}^2(\pi f t_E)}{(\pi f t_E)^2}. \quad (2.50)$$

The other distortion on PSD curve is aliasing, which occurs in the sampling process that the frequency components higher than the Nyquist frequency overlap with the sampled spectrum. The corrected PSD can be given by⁹⁵

$$P_{A,B}(f) = \sum_{n=-\infty}^{\infty} P_B(|f + n f_s|), \quad (2.51)$$

where n is integer and $f_s = 1/\Delta t$ is the sampling frequency. D and f_c are the parameters to be estimated by fitting the experimental PSD using Eq. 2.51, for which the unbiased fitting should perform the maximum likelihood estimation (MLE), and that is equivalently to search the minimal of the cost function⁹⁵

$$F_c = \sum_k n_b \left[\frac{\tilde{y}_k}{y_k(D, f_c)} + \ln y_k(D, f_c) \right], \quad (2.52)$$

where n_b is the number of blocks for the averaged preprocessing to the positions data⁹⁶, \tilde{y}_k and y_k are respectively the measured PSD and theoretical expression of $P_{A,B}$. The minimization of F_c gives the diffusion coefficient D and the associated corner frequency f_c . In case of free diffusion, $f_c = 0$, otherwise, $f_c > 0$, representing the presence of restoring force on the particle, such as for optical tweezers.

2.3 Chapter Summary

In this chapter, the theoretical models of optical fibers, including the step-index fiber and NBF, and Brownian motions of particles in liquids with the corresponding analysis methods, including the MSD and PSD, have been introduced. These foundations are the working principles of the FaNTA and can be appropriately applied for the related data analysis. The next chapters present three research works: NTA using NBF with ultralong tracking; and the realization of a flattened mode in NBF—the light strand—to improve the performance of FaNTA; a fiber-based optofluidic device with flattened illumination. The results have demonstrated that the FaNTA is compatible with general analysis tools and can be further extended to applications, such as life science, refractive index sensing, and fundamental studies of light-matter interactions.

3 | Ultralong Tracking of Fast-Diffusing Nanoparticle in Nanobore Optical Fiber

NTA plays a crucial role in characterizing the motions of Brownian nanoparticles in liquids. To reveal the dynamic processes of nanoparticles in high-precision measurement necessitates the acquisition of tracking with a long trajectory which ensures high statistical significance. In this chapter, the FaNTA using NBF has demonstrated an approach to enable the tracking of a fast diffusing golden nanosphere with 100,000 frames and a frame rate up to 2 kHz. The diffusion of nanoparticles is spatially confined in the nanofluidic channel and illuminated by the guiding mode, allowing for the recording of Brownian motion over ultralong duration at high frame rates. Due to the benefits of the long trajectory, segmented data analysis is possible, which can reveal the dependence between the measured diffusion coefficient and the number of frames per sub-trajectory. The results show that the FaNTA not only possesses the ability to monitor the dynamic processes of fast diffusing nanoobjects, but also determine their size with extraordinary accuracy, both of which promote the applications of NTA on biology, microrheology, and nano-object characterization.

This chapter is based on the publication by Gui et al.⁹¹, reproduced with a CC-BY license. Copyright 2021, The Authors, Published by Wiley.

3.1 Introduction

As discussed in chapter 2.2.3, the measurement accuracy significantly depends on the length of the trajectory N , or the number of the frames per track, the statistical error of the MSD method, described by the parameter CRLB, decreases as the N increases, where the error is roughly proportional to $1/\sqrt{N}$. Furthermore, the longer the observation duration of the nanoparticle, the more dynamic information can be monitored from the diffusion process, providing more insights into the interactions between the probe and the surrounding environment. Thus, long and continuous tracking is crucial in the NTA applications, such as behaviors of nano-objects on membranes^{22,24}, or the study of anomalous diffusion^{97,98}. The tracking of a fast-diffusion single nanoparticle with a long trajectory is a challenge in the experiments of NTA since the nanoparticle can easily escape from the focal depth of the objective if there is no spatial limitation to the field of view (FoV). The trajectory will interrupt once the object moves out of the FoV, which can happen in a second, for example, a nanoparticle with diffusion coefficient $D = 1 \mu\text{m}^2/\text{s}$ in the FoV of $6 \times 6 \mu\text{m}^2$, the typical observing time is 1 sec-

ond^{99,100}. It is reported that a long tracking of 150,000 frames but with a low diffusion speed $D = 0.017 \mu\text{m}^2/\text{s}$ has been achieved, where the axial confinement and adaptive focusing stage has been used for orbit tracking of single-particle in glycerin solution⁹⁹.

In 2015, Faez et al. presented a novel NTA approach that utilizes microstructured optical fibers featuring a nanofluidic channel along the fiber axis, the NBF as mentioned before, which enables rapid, label-free, and long observation of nano-objects or single virus^{52,101}. The field of fiber-assisted NTA (FaNTA) has been developed after this innovative waveguide-based approach was proposed, and there is a series of research works published in recent years. Jiang et al. reported the full 3D tracking of a single nanoparticle based on intensity-dependent position retrieval in optofluidic microstructured fiber^{92,102}. Foerster et al. presented the size measurements of multi nanoparticles (hundreds) using antiresonant hollow-core fibers (ARHCF)¹⁰³.

The capability of FaNTA to acquire ultralong trajectories is attributed to the confinement of nanoobjects inside the fluidic channel as well as the light-strand illumination by the guiding mode, providing a well-confined focal depth and reduced FoV (longitudinal direction of the fiber) that supports a higher readout speed (frame rate). As a result, these comprehensive advantages can significantly improve the ability to track fast-diffusion nanoobjects with ultralong trajectory, paving the way for new applications of NTA.

In this work, the NTA experiment is carried out using NBF and it demonstrates that the FaNTA approach can support a tracking of fast-diffusion nanosphere (50 nm diameter and $D = 6 \mu\text{m}^2/\text{s}$) with an ultralong trajectory of 100,000 frames and the observation time is nearly 40 s. To determine the D of the nanosphere, the data is analyzed by using the MSD method. Due to the benefits of the large number of N , the data set can be segmented into sub-trajectory, and the related measurement errors are calculated, showing a good agreement with CRLB, the lower error limit, which indicates the advantage of the FaNTA in recording long trajectories.

3.2 Concept and Experimental Setup

NBF has a concentric 3-layer structure, including a central nanochannel to fill with the nanoparticle solution, a Ge-doped core for guiding the optical mode in the fiber, and a pure silica outer cladding, which is shown in Fig. 3.1 (a).

The tracking experiment is conducted in the water-filled NBF, and due to the low RI of water (compared to the core), the mode field is evanescent inside the nanochannel, where suspending nano-objects elastically scatter the light field, which is then collected by a microscope. CMOS camera is used to image the scattered signal (depicted in the bottom of (a)), and the motion of the nanoobject is recorded into a series of individual frames. Fig. 3.1 (b) shows the scanning electron microscopic (SEM) image of the fiber

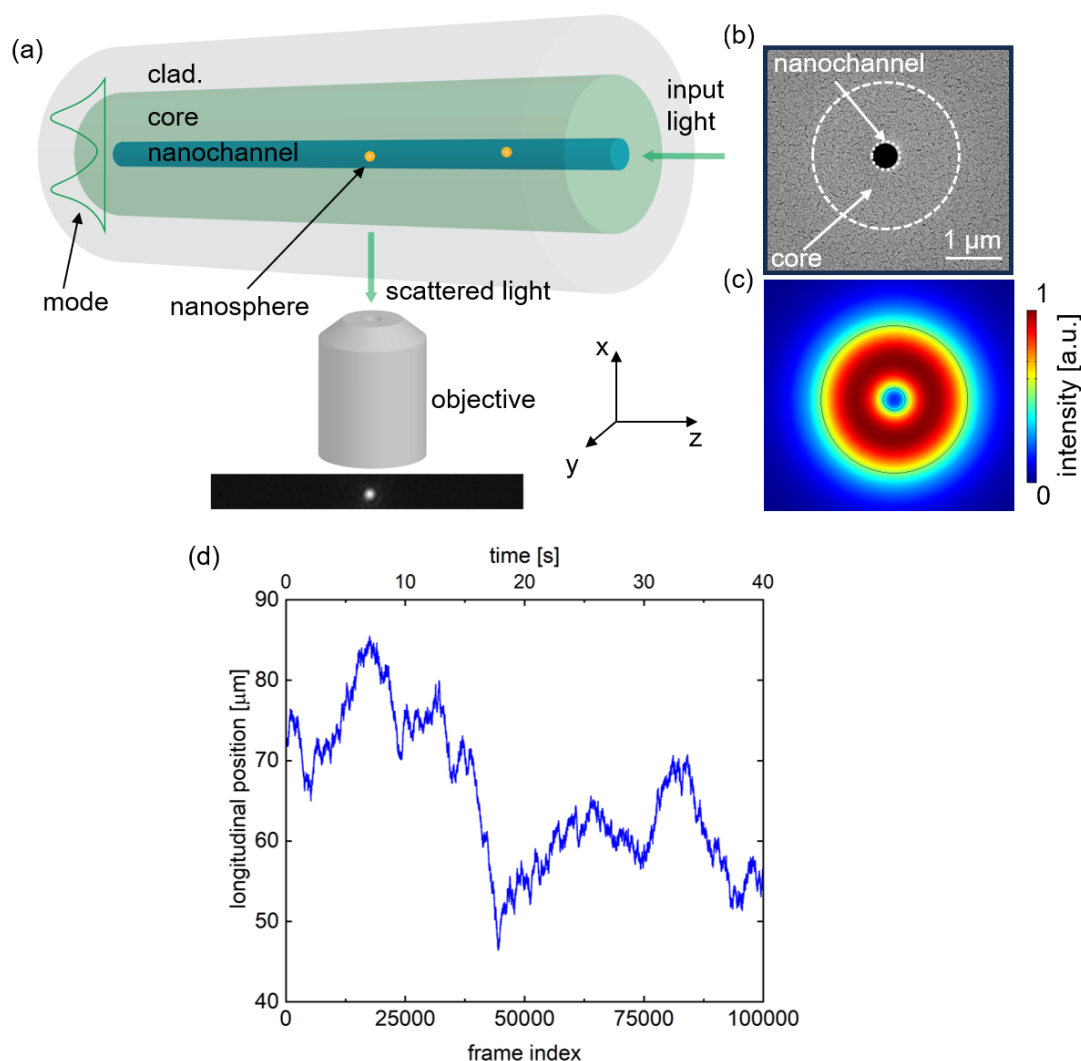


Figure 3.1: NTA inside the NBF filled with nanosphere suspension solution. (a) Illustration of the concept, including the NBF, nanosphere, objective, and a sample of the imaged nanosphere. The cyan area refers to the nanochannel filled with nanosphere solution, the light green area represents the doped core, and the gray part is the silica cladding of the fiber, where the RI of the nanofluidic channel, doped core and silica cladding are respectively $n_1 = 1.3337$, $n_2 = 1.4687$ and $n_3 = 1.4607$. (b) SEM image of the cross-section of the NBF, the diameter of the nanochannel is nearly 560 nm. (c) The simulated intensity distribution of the fundamental mode in the NBF at the operating wavelength of 532 nm. (d) Recorded trajectory in the longitudinal direction (z-axis) from a 50 nm golden nanosphere as a function of frames and the observation time (bottom and top axes), where the total number of frames is 10^5 and the corresponding time is 40 s.

cross-section, where the radii of the channel and Ge-doped core are $a = 280$ nm and $b = 1.9$ μm , respectively. The RI of the water-filled channel, Ge-doped core, and pure silica cladding are $n_1 = 1.3337$, $n_2 = 1.4687$ and $n_3 = 1.4607$ (more detailed information about the NBFs can be found in the publication by Schaarschmidt¹⁰⁴). As discussed in the previous chapter, the guidance mechanism of NBF is based on the total internal

refraction. Here, the RI of the doped core is higher than the cladding and water-filled channel, the energy of the fundamental mode (at working wavelength $\lambda = 532$ nm) is mainly concentrated in the core region whereas the channel consists of the decaying fields, forming an evanescent mode as shown in Fig. 3.1 (c). The mode field varies only in the transversal direction and keeps invariant longitudinally, as a consequence, a line-shaped illumination is formed upon the nanoobjects along the fiber length. The diffusion motion of the nanoobject is then recorded as continuous frames and Fig. 3.1 (d) shows the results of longitudinal positions (z -positions) as a function of the recording time or frames (the top or bottom axis). One feature of the NBF-based NTA is that the high RI doped core can confine most of the mode power due to the total internal reflection, preventing the illuminating light from entering the objective, which improves the signal noise ratio (SNR) for the detection of the scattered light. Furthermore, since NBFs possess distinctive modal properties and relatively simple structure compared to other types of microstructured fibers, they have been applied in other experiments, such as nonlinear plasmonics¹⁰⁵ and fiber-integrated spectroscopy¹⁰⁶.

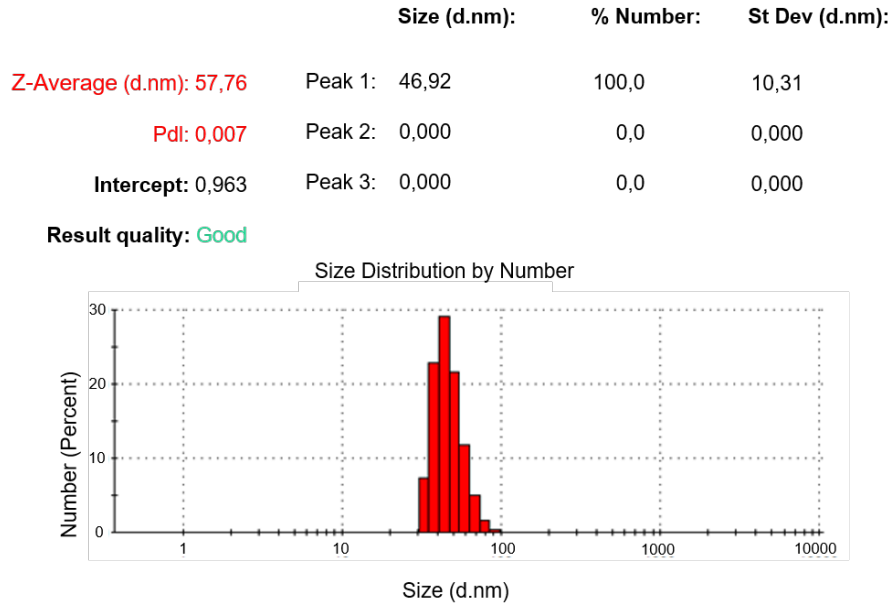


Figure 3.2: Hydrodynamic diameter measurement of the nanospheres which is conducted via an in-house ZetaSizer instrument.

The aqueous solution of ultra uniform golden nanosphere (mean diameter $\bar{d}_p = 49.4 \pm 2.2$ nm, concentration: 4.2×10^{10} particles/ml, nanoComposix) was used in the experiment. The mean hydrodynamic diameter of the nanospheres is $\bar{d}_h = 58 \pm 10$ nm, which is measured by the commercial instrument Zetasizer (Malvern), and the detained information is shown in Fig. 3.2. The particle solution can be filled into the nanofluidic channel via capillary force, which is achieved by immersing the output side of the fiber into the sample and the liquid will flow along the channel spontaneously.

The filling time for the nanochannel with a length of 10 cm and a diameter of 560 nm is about 20 minutes, which can be estimated by Washburn equation¹⁰⁷. Once the solution reaches the observation area, the tip of the fiber is sealed using plasticine to stop further flowing and maintain the nanoobjects within the observation area.

The sketch of the experimental setup is shown in Fig. 3.3. The input laser of 532 nm (WhisperIT, W532-50FS) is coupled into the NBF by an objective lens (40 \times , NA = 0.65, Olympus). Shown as the inset of Fig. 3.3 (a), the scattered light from the nanosphere suspending in the nanofluidic channel is collected by an oil-immersed objective (60 \times , NA = 0.9, Olympus), and then detected by a fast CMOS camera (ANDOR Zyla 4.2 Plus, pixel scale: 72.6 nm/pixel), where the acquisition settings are exposure time $t_e = 0.2$ ms and frame rate $\nu = 2480$ Hz. The imaging system is well optimized and diffraction limited as can be seen in the sidebands of the PSF on the image plane (see the inset at the lower left corner in Fig. 3.3 (a)). Note that the number of nanoparticles per FoV in the tracking can be estimated by multiplying the concentration (4.2×10^{10} particles/ml) and the volume of the nanochannel (2.7×10^{-11} ml), leading to nearly one nanoparticle in the FoV.

The image processing is programmed by using the Python package *Trackpy* to localize the position of nanoobject through calculating the mass center of the PSF in each frame (another useful package *PyNTA* was released by Faez et al.¹⁰⁸). For the 100,000 frames trajectory, the parallel programming yields a total computing time is 287 s, comprising 101 s for reading the frame stack in tiff format, 124 s for localization of nanoparticle, and 53 s for linking the trajectory of the single particle (link the nearest-neighborhood positions from the individual frames). The length of the entire trajectory is 100,000 frames and the corresponding duration is 40.3 s, for which the statistical histograms of the z-displacement with lagtimes (Fig. 3.1 (b)) are fitted by normal distribution probability density function, indicating the nanoobject is diffusing as Brownian motion¹³.

3.3 Methods

To demonstrate the advantage of the FaNTA in the acquisition of ultralong trajectory and enhanced statistical accuracy, firstly, we apply 1D-MSD analysis to determine the diffusion coefficient D using the position data of longitudinal direction (z -axis). In addition, the PSD method as an alternative approach to estimate D is used to confirm the results of MSD analysis. Furthermore, the long data set is segmented into sub-trajectories for error analysis. It is important to note that the wall of the nanochannel in NBF leads to a spatial hindrance to the diffusion of nanoparticles, this effect can be described by the so-called resistance factor in the view of hydrodynamics. Therefore,

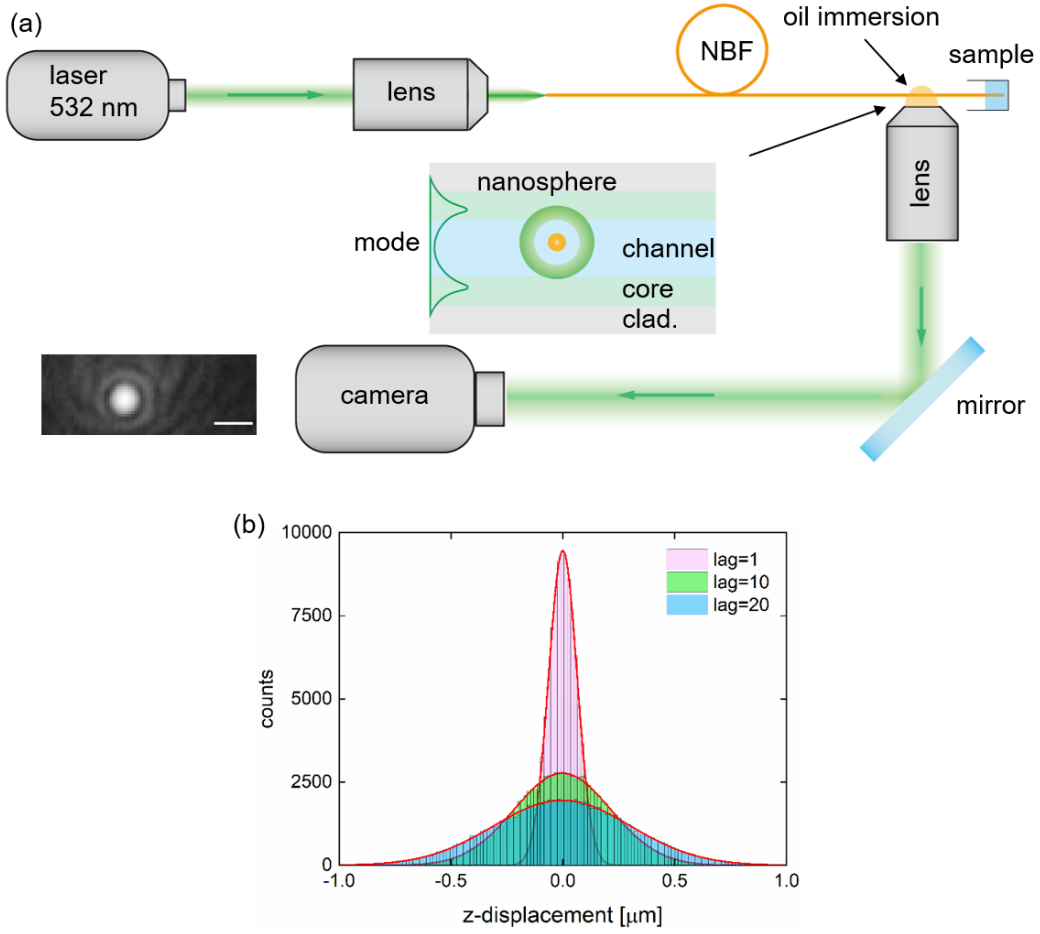


Figure 3.3: Experimental setup of the FaNTA. (a) Sketch of the setup, including laser coupling arrangement, NBF, and microscope system. The central inset shows the mode excitation and scattering process of the nanosphere inside NBF. The inset at the lower left corner shows one example of the imaged nanosphere, where the white bar indicates a length of 1 μm . (b) Histograms of the displacement of the recorded trajectory (the one shown in Fig. 3.1) with different lagtimes: 1 frame (0.4 ms), 10 frames (4 ms), and 20 frames (8 ms), respectively.

a theoretical model is introduced to calculate the resistance factor so that the free diffusion coefficient (unconfined) can be corrected.

3.3.1 MSD Analysis

As discussed in the chapter 2.2.3, the 1D-MSD of nanoparticle with diffusion motion is given by⁴⁵

$$\langle z^2(n\Delta t) \rangle = 2D_c n\Delta t + 2\sigma^2 - \frac{2D_c t_E}{3}, \quad (3.1)$$

where $\langle z^2(n\Delta t) \rangle$ is the MSD in z -positions and calculated by using the expression in Eq. 2.33, $n=1, 2, 3, \dots, N_c - 1$ is the number of lagtimes and N_c is the number of continuous frames in a trajectory. D_c represents the corrected diffusion coefficient in the

nanochannel. The linear fitting is performed to the MSD calculated from the segmented trajectory to obtain a time-resolved series of D_c , making it possible to conduct error analysis with CRLB and clarify the measurement accuracy that depends on the number of frames (N).

3.3.2 PSD Analysis

Besides the MSD method, the diffusion coefficient can also be determined through PSD analysis that is to fit the power spectrum of the nano-object's position in the frequency domain^{93,95}. The detailed expressions of PSD and the corresponding MLE fitting have been shown in chapter 2.2.4. The PSD method is employed for video tracking of single particles in harmonic potentials, such as optical trapping^{109,110} and magnetic tweezers¹¹¹. For the nanoparticles' diffusion in the nanofluidic channel of NBF, there is no restoring force along the longitudinal direction, as a result, the z-direction diffusion still keeps free and the related PSD curve will show a steadily decreasing function in the positive frequency domain (the corner frequency f_c is close to 0).

3.3.3 Random Walk Simulation

To examine the experimental results, a random walk simulation of particle diffusion that matched the experimental conditions has been conducted, where $t_e=0.2$ ms, $\nu=2480$ Hz, $N = 10^5$, $NA = 0.9$ and $\lambda=532$ nm. The random walk of 1D diffusion along the fiber axis (z-direction) is performed, disregarding the reflections at the liquid/solid boundary, and the localization uncertainty and motion blur ($m=100$ for microstep) were included to produce the negative offset of MSD (discussed in chapter 2.2.3). Taking into account the hindrance effect from the channel, the measured diffusion coefficient (corrected value of the D in free diffusion) D_c has been used in the random walk. Note that although the nanochannel restricts the transversal motions of the nanoparticles, the random walk simulation in a longitudinal direction can be still considered as free diffusion, since it has been demonstrated experimentally that the measured MSD is a linear function as the first few lagtimes and not saturation observed in the delayed ones.

3.3.4 Hindrance Effect and Averaged Resistance Factor

Due to the sub-micron diameter of the fluidic channel in NBF, it is important to emphasize that the measured diffusion coefficient D here is modified by the transversal hindrance of the channel, leading to the confined diffusion^{112,113}. As a result, the D has decreased compared to the case without the confinement, or equivalently, the viscosity of the liquid has increased. The diffusion in the z-direction is also slowed down, even though there is no direct longitudinally hindrance. This effect can be accounted by the

so-called average resistance factor R_{avg} ^{102,114}, and the corrected diffusion coefficient (with confinement) $D_c = D_f/R_{avg}$, where D_f is the free diffusion coefficient without confinement. Note that the MSD of z -positions remains linear, whereas the MSD for x or y -positions will be nonlinear and saturated with the lagtimes (confined diffusion). However, the motion in the z -direction can be still regarded as free diffusion, and modified by the factor of R_{avg} . A comparison of MSD curves of the nanosphere in z - and y -directions is shown in Fig. 3.4.

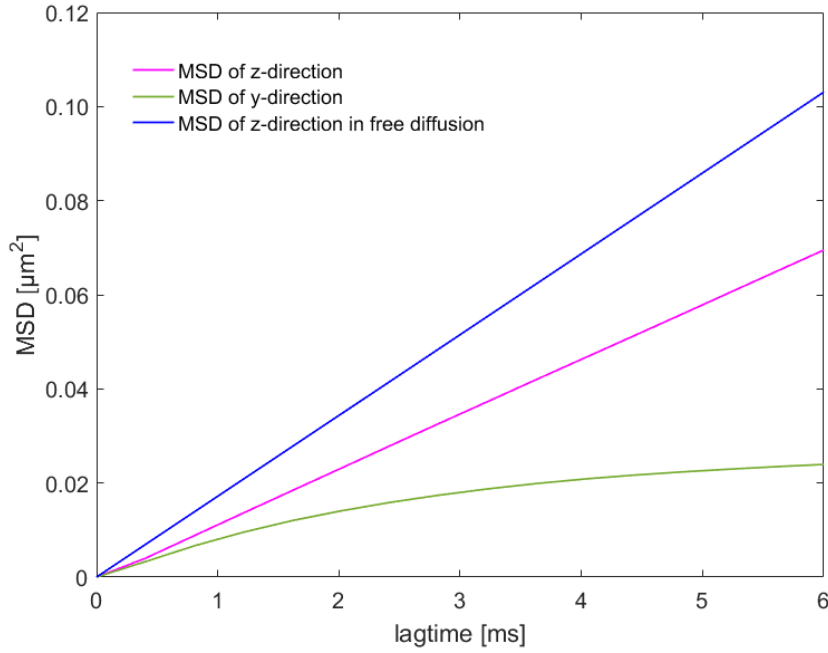


Figure 3.4: MSD curves for transversal and longitudinal directions of the 50 nm golden nanoparticle tracked in NBF. The MSD of free diffusion is calculated by $2Dt$, where D is obtained from the Stokes-Einstein relation.

Inside the channel, the viscosity of the liquid gradually increases towards the liquid-wall interface, leading to a denser position distribution of the nanoparticle. Thus the diffusion coefficient is dependent on the radial coordinates $D(r)$, and given by¹¹⁴

$$D(r) = \frac{D_f}{R(\lambda, r)}, \quad (3.2)$$

where $R(\lambda, r)$ is the resistance function, $\lambda = r_p/a$, r_p and a are the radii of nanoparticle and fluidic channel, respectively. The expression of $R(\lambda, r)$ has been given out by Higdon, et al. based on the fluid mechanical model for spherical particles in cylindrical tube¹¹⁴

$$R(\lambda, r) = \sum_{i=0}^7 [c_i(\lambda)\psi_i(\lambda, r)], \quad (3.3)$$

the corresponding parameters are defined as below

$$\begin{aligned}
\psi_0 &= 1; & \psi_1 &= \lambda\beta^2; & \psi_2 &= \lambda\beta^4; & \psi_3 &= \frac{\beta^2}{\rho}\beta^{2m}; & \psi_4 &= \left(\frac{\beta^2}{\rho}\right)^2\beta^{2m} \\
\psi_5 &= \delta\left[\ln\left(\frac{\delta+1}{\delta}\right) - \ln\left(\frac{\delta_0+1}{\delta_0}\right)\right] - \beta^2\frac{\delta_0+1}{\delta_0}; \\
\psi_6 &= \ln\left(\frac{\delta+1}{\delta}\right) - \ln\left(\frac{\delta_0+1}{\delta_0}\right) - \beta^2\left(\frac{\delta_0+1}{\delta_0}\right); \\
\psi_7 &= \frac{1}{\delta} - \frac{1+\beta^2}{\delta_0}; & \beta &= \frac{r}{(a-r_p)}; & \rho &= \frac{1}{\lambda}[1 - \beta^2(1 - \lambda)^2]; \\
\delta &= \frac{1}{2\lambda}(1 - \lambda)(1 - \beta^2); & \delta_0 &= \frac{a-r_p}{2r_p}.
\end{aligned} \tag{3.4}$$

Here the values of c_i with respect to λ can be found in section 4 of the publication by Higton et al.¹¹⁴, and arbitrary values of λ should be obtained by interpolations. The calculation of the resistant factor for z-direction has $m = 2$. The weighted average of the inverse resistance factor is obtained by the integral the $R(\lambda, r)$ through the cross-section of the nanochannel

$$1/R_{\text{avg}} = \frac{\int_A w/R(\lambda, r)dA}{\int_A wdA}, \tag{3.5}$$

transform to cylindrical coordinates and yield

$$1/R_{\text{avg}} = \frac{\int_0^{a-r_p} w/R(\lambda, r)rdr}{\int_0^{a-r_p} wrdr}, \tag{3.6}$$

assume that the particle is homogeneously distributing in the channel so that the integral is unweighted ($w = 1$)¹⁰²

$$1/R_{\text{avg}} = \frac{\int_0^{a-r_p} /R(\lambda, r)rdr}{\int_0^{a-r_p} rdr}. \tag{3.7}$$

Note that the R_{avg} is dependent on the radii of the nanoparticle r_p and channel a , which is supposed to be unknown in the NTA measurement. Thus it is needed to conduct a numerical solution to the equation $\tilde{r}_p - r_p R_{\text{avg}}(r_p, a) = 0$, where \tilde{r}_p is the measured radius of the nanoparticle from MSD fitting (use Einstein-Stokes relation), and r_p is the actual radius we want to retrieve for the unconfined situation.

3.4 Results

3.4.1 MSD and PSD Analysis

The trajectory of a single nanosphere with 10^5 frames (Fig. 3.1 (d)) has been analyzed by MSD and PSD methods, the corresponding results are shown in Figure 3.5, proving the consistency of the results from both of the approaches. The measured $D_c^{\text{MSD}} = 5.97 \mu\text{m}^2/\text{s}$ is obtained by fitting the first two lagtimes of MSD, which perfectly matches the result from the PSD fitting, $D_c^{\text{PSD}} = 5.98 \mu\text{m}^2/\text{s}$. The retrieved hydrodynamic

diameter of the nanosphere (without the confinement of nanochannel) is $d_h = 53.3$ nm (the expected value is 58 nm measured by Zetasizer) and the corresponding resistance factor $R_{avg} = 1.35$.

Note that the choosing of the only first two lags is optimal since the value of reduced square localization error x is small (here $x = -0.16$), leading to a negative fitting offset, and more lags in the fitting could introduce additional error to the estimation of D^{45} . As shown in Eq. 3.1, the term $-2D_c t_E/3$ (motion blur in finite exposure time) contributes to the negative offset in MSD fitting. In our measurement, the localization uncertainty $2\sigma^2$ is negligible compared to the value of $2D_c t_E/3$, and the calculated $-2D_c t_E/3 = -7.96 \times 10^{-16}$ m² which is in agreement with the offset -8.11×10^{-16} m² from the MSD fitting.

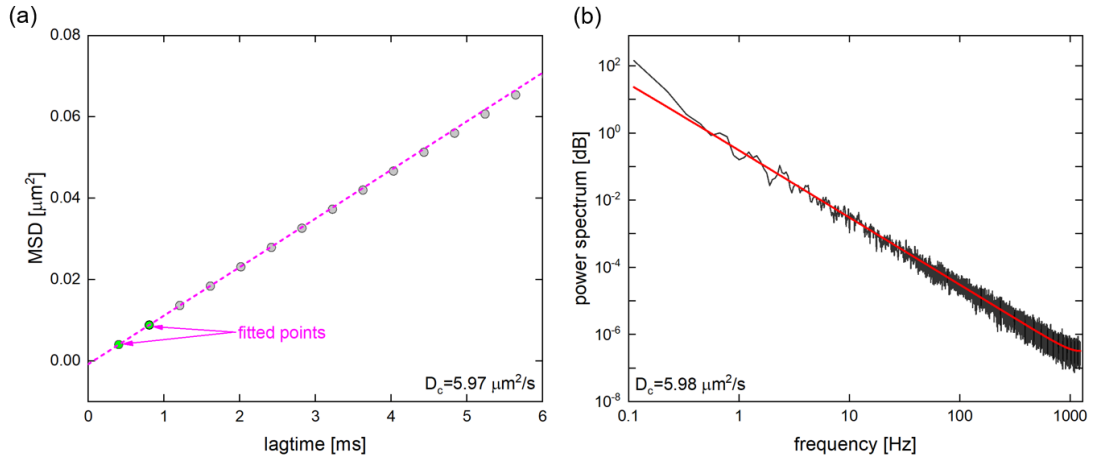


Figure 3.5: Results of the MSD and PSD fittings using the 10^5 frames trajectory shown in Fig 3.1 (d), yielding the identical D_c . (a) MSD fitting using the first two data points (green) based on Eq. 3.1, showing a well-linear distribution and a negative offset. (b) PSD fitting based on MLE using the expressions in section 2.2.4.

3.4.2 Segmented Trajectory

The obtained long trajectory of the single nanoparticle ($N = 10^5$ frames with tracking duration of 43 seconds) can be divided into sub-trajectories with a shorter length. Then MSD analysis is separately performed on each sub-trajectory for estimations of the diffusion coefficients. As a consequence, a dynamic measurement of the diffusion for a single nanoparticle is available and the time resolution is dependent on the length of the sub-trajectory. Besides, due to the statistical nature of MSD, the determined D has intrinsic deviation even though all the trajectories are obtained from identical nanoparticle. This error can be quantified by using the segmented analysis.

Specifically, the entire trajectory is divided into n_s segments with equivalent length $N_c = N/n_s$. The results of the calculated MSD curves, as representative, $n_s = 200$; $N_c =$

500 and $n_s = 50$; $N_c = 2000$, are shown in Figs. 3.6 (a) and (b), respectively. It clarifies that both the slopes and offsets of the MSDs are different, and the deviation is smaller as the increasing of N_c . The corresponding diffusion coefficients D_c^{seg} fitted from the MSDs as functions of time are shown in Figs. 3.7 (a) and (c), which vary in time with random fluctuations around the mean value ($\overline{D}_c^{seg} = \frac{1}{N_c} \sum_{N_c} D_c^{seg} = 5.97 \mu\text{m}^2/\text{s}$, labeled as the solid horizontal lines). The dashed horizontal lines denote the standard deviations σ_D^{seg} of the D_c^{seg} in the related segments.

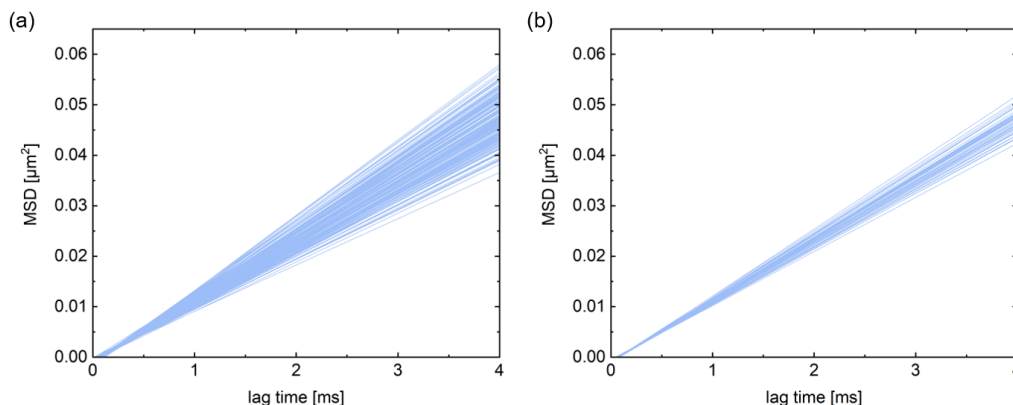


Figure 3.6: Results of the segmented MSDs from the full trajectory of a single nanoparticle. (a) MSD curves with the number of segments $n_s = 200$ and the number of frames per sub-trajectory $N_c = 500$. (b) MSD curves for the case of $n_s = 50$ and $N_c = 2000$.

Note that both cases give the same mean value of D_c^{seg} , however, compare (a) and (c), the larger length of the sub-trajectory (N_c) leads to the smaller fluctuations of D_c^{seg} . The hydrodynamic diameters of the single nanosphere retrieved from the segments analysis are plotted as histograms in Figs. 3.7 (b) and (d), which also demonstrate the case of larger N_c produces a higher accuracy (narrower distribution). These results experimentally reveal the dependence between the precision of MSD analysis and the length of the trajectory, and show the potential of FaNTA on dynamic detection of a single nanoparticle's diffusion behavior.

3.4.3 Error Analysis

Due to the benefit of the ultralong trajectory, we can use the segments analysis to quantitatively reveal the dependence of the error corresponding to the measured diffusion coefficient and the length of the trajectory. In Fig. 3.6, the histograms clearly show that the statistical average of D_c^{seg} keeps invariant as different frames N_c , however, the relative standard deviation $\sigma_D^{seg} / \overline{D}_c^{seg}$ significantly depends on N_c . Thus, we use the segment analysis for different numbers of frames ranging from $10^2 < N_c < 10^5$. Note

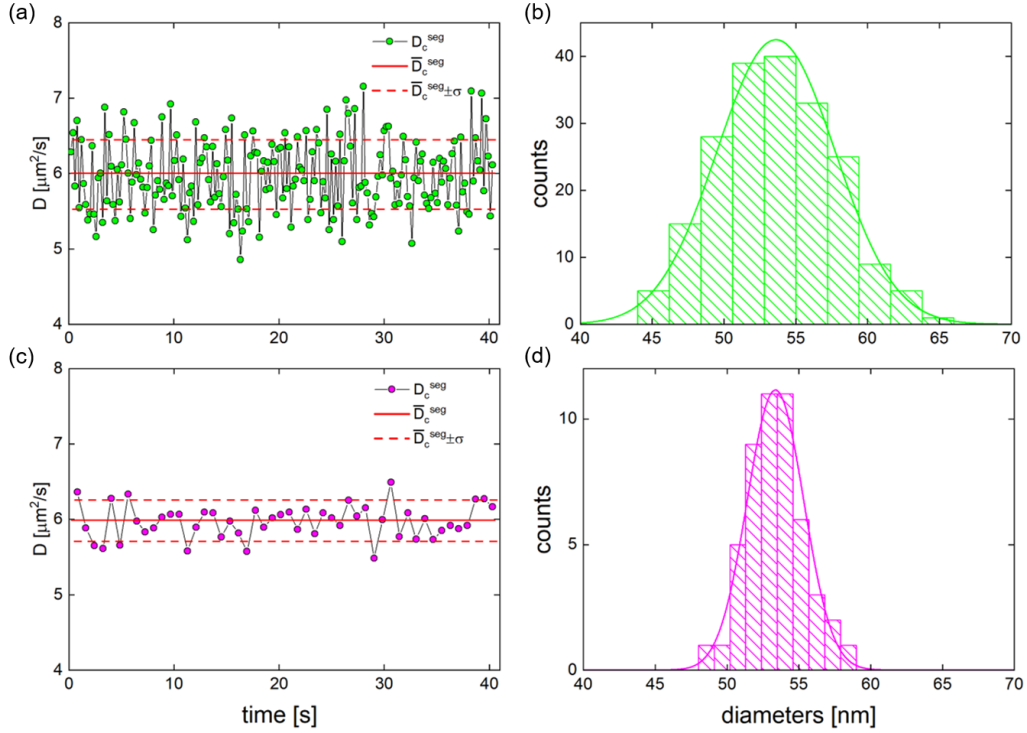


Figure 3.7: Results of the segmented MSD analysis with two examples: (a)-(b) The measured diffusion coefficients with the number of segments $n_s = 200$ and the number of frames per sub-trajectory $N_c = 500$ (the time resolution is $43/200 \text{ s} = 0.215 \text{ s}$). The scatter plots show the resolved D from each sub-trajectory, where the standard deviation $\sigma_D^{seg} = 0.58 \mu\text{m}^2/\text{s}$. The histogram shows the retrieved hydrodynamic diameters from (a), where the standard deviation $\sigma_d^{seg} = 4.13 \text{ nm}$, obtained by using inverse Gaussian fitting (solid line). (c)-(d) The measured diffusion coefficients for the case of $n_s = 50$ and $N_c = 2000$ (the time resolution is $43/50 \text{ s} = 0.86 \text{ s}$), the standard deviations are $\sigma_D^{seg} = 0.28 \mu\text{m}^2/\text{s}$ and $\sigma_d^{seg} = 1.97 \text{ nm}$.

that the results here emphasize the condition of "single nanoparticle", which means the actual D_c or diameter of the object is never changed, and it differs from the measurements based on dynamic light scattering (DLS) such as Zetasizer that characterize a large number of nanoparticles. Figure 3.7 (a) shows the averaged hydrodynamic diameters, having a similar value $d_h^{sed} = 53 \text{ nm}$, and the standard deviations (plotted as error bar) as functions of the frame length N_c , indicating that the σ_d^{seg} decreases as the number of frames N_c , which is in agreement with the CRLB prediction (Eq. 2.36).

To deeply understand the errors that arise in FaNTA experiment, Fig. 3.8 (b) compares the experimental results of the dependence between relative standard deviation of the segmented diffusion coefficient $\sigma_D^{seg} / \overline{D}_c^{seg}$ and trajectory length N_c with the simulated and theoretical results (CRLB in Eq. 2.36). Note that when $N_c < 10^3$ the experimental $\sigma_D^{seg} / \overline{D}_c^{seg}$ are in good agreement with the CRLB curve, but deviations occur at the larger N_c . This is due to the decreasing sample size (number of subtrajectories) as the increasing length of subtrajectory and thus the statistical significance

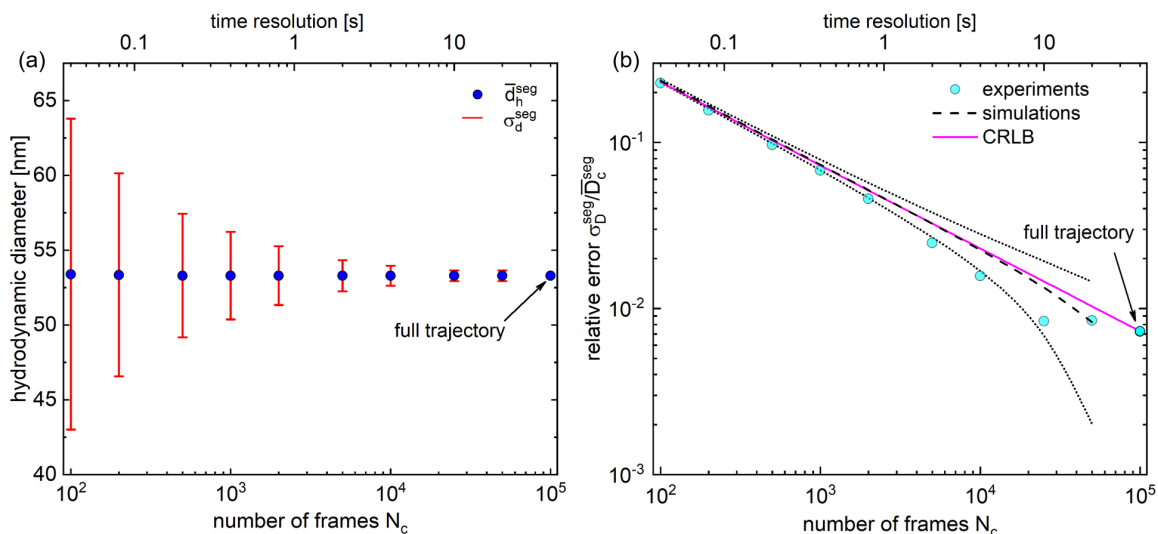


Figure 3.8: Statistical results of MSD analysis for the segmented subtrajectory from representative trajectory depicted in Fig. 3.1 (d). (a) The averaged hydrodynamic diameters and associated standard deviations (error bar) as functions of the number of frames per sub-trajectory N_c . The final point labeled as full trajectory refers to $N_c = 10^5$ and has no error bar. The bottom and top axes refer to N_c and the time resolution (the duration of the sub-trajectory with a length of N_c). (b) Relative standard deviations of the measured diffusion coefficients as a function of N_c , where the experimental results, simulations, and theoretical CRLB are indicated by cyan points, magenta, and black lines, respectively (the dashed line refers to the averaged results of CRLB from 5000 times simulations, and the dotted lines refer to the plus or minus of the standard deviation of the simulations). The final point with the full trajectory $N_c = 10^5$ predicts the standard error to be $\sigma_D^{seg}/\bar{D}_c^{seg} = 0.7\%$.

is reduced. For example, there are only 10 subsets when $N_c = 10^4$ (the entire length is 10^5), as a result, the value of $\sigma_D^{seg}/\bar{D}_c^{seg}$ fluctuates around the theoretical prediction. To validate this impact, we performed 5000 independent simulations with completely identical conditions as the experiment (including the segmented analysis) and obtained the averaged $\sigma_D^{seg}/\bar{D}_c^{seg}$ and the associated deviations (presented by black lines in Fig. 3.8 (b)), which allows to reveal the system errors from the segmented analysis. Once the sub-trajectory length N_c is fixed, the entire trajectory (10^5 frames here) yields one value of $\sigma_D^{seg}/\bar{D}_c^{seg}$, which will fluctuate around the CRLB curve, however, if one conduct repeated simulations (5000 times here) the resulting averaged value will be consistent with the CRLB prediction, shown as the black dashed line in Fig. 3.8 (b).

3.5 Discussion

A crucial finding of the segmented analysis (Fig. 3.8 (b)) is the experimental demonstration of the dependence between the error of the diffusion coefficient measurement and the number of frames per sub-trajectory, given by the relative standard deviation

$\sigma_D^{seg}/\overline{D}_c^{seg}$. The results could guide the development of a NTA experiment with a determined precision expectation using MSD analysis, for example, a relative error of 5% for a measured diffusion coefficient or diameter needs at least 1000 continuous frames in each trajectory of the nanoobject.

In addition, the number of frames in the entire trajectory is particularly essential in the detection of the dynamic process of nanoobject (e.g., the environment-induced size changes of the core-shell nanoparticles¹¹⁵), since each sub-trajectory (the length is N_c) can be transferred into a time interval in which the diffusion coefficient is determined and the associated time resolution is dependent on the frame rate (ν) of the camera, $\Delta T = N_c/\nu$, shown in the top-axis of Fig. 3.8. Note that the time resolution can be improved by increasing the frame rate, however, it is limited by the minimal exposure time t_E to obtain sufficient signal from the nanoobject. This long tracking can be a potential approach used for the dynamic monitoring of nanoparticle diffusion behavior in complex environments where the D_c or d_h is time-dependent.

To compare the presented results with other approaches, Table 3.1 collects some of the key achievements from the NTA experiments reported in recent years. Even though there is literature reporting a successful nanoparticle tracking with more than 10^5 frames, note that the FaNTA in this work supports tracking of fast-diffusion (100 times larger diffusion coefficient) nanoparticles due to the confinement feature of the nanofluidic channel. Besides, the free diffusion length in FaNTA here (a distance that the particle can diffuse during the recording time $l = \sqrt{2Dt}$) is 22 μm in 43 s, exceeding most of the other reported works shown in Table 3.1.

Particle /diameter (nm)	Measured D ($\mu\text{m}^2/\text{s}$)	Frame rate (Hz)	Frames /duration (1)/(s)	Diffusion length (μm)	Matter	Approach
Au/50	5.97	2480	$10^5/41$	22	water	NBF (this work)
Au/51	5	1000	$2 \cdot 10^4/20$	14	water	NBF ⁵²
Au/100	4	25	$3 \cdot 10^3/120$	31	water	dark-field microscopy ⁴⁸
Au/20	1.6	10^5	$10^5/1$	1.7	membrane	iSCAT ¹⁰⁰
Au/20	1.48	$5 \cdot 10^4$	$1.55 \cdot 10^5/3$	3	membrane	iSCAT ²²
fluo-beads /200	0.17	20	$3 \cdot 10^3/150$	7.14	glycerol-water	multifocal microscopy ¹¹⁶
Au/20	0.16	1000	$5 \cdot 10^3/5$	1.26	membrane	iSCAT ²⁴
fluo-beads /20	0.017	250	$1.52 \cdot 10^5/608$	4.5	glycerol	fluo-microscope ⁹⁹

Table 3.1: Comparisons of key parameters in this work with other NTA experimental approaches in recent years.

To highlight the advantages of FaNTA compared with other scenarios, the measured diffusion coefficients corresponding to the number of frames are presented in Table. 3.1

are shown in Fig. 3.9. It indicates that the FaNTA approach possesses the ability to track fast-diffusion nanoobjects and still acquire a large number of frames, which enables high precision for the MSD analysis and dynamic detection of nanoparticle's diffusion behavior.

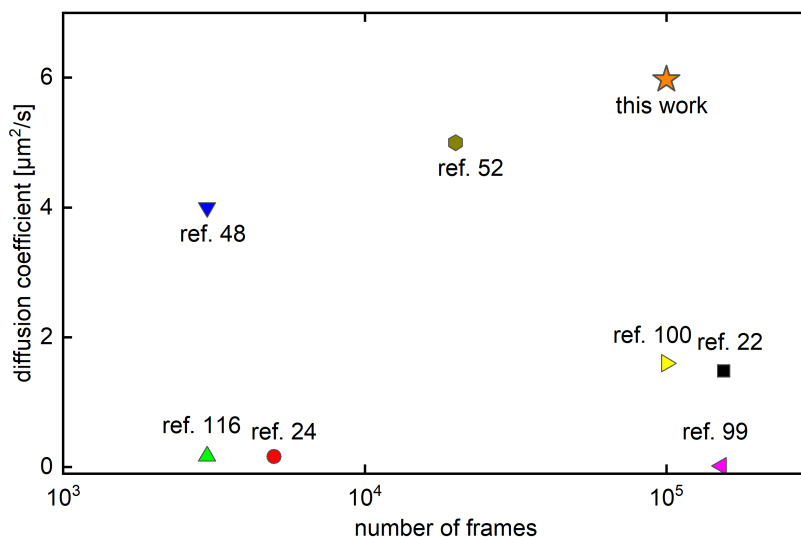


Figure 3.9: The measured diffusion coefficients and the recorded number of frames in reported NTA experiments corresponding to Table 3.1.

In this work, 10^5 continuous frames from a single nanosphere (the trajectory is shown in Fig. 3.1 (d)) are used for the MSD analysis, which is the typical number of frames that have been successfully recorded via our FaNTA system. Using the $60\times$ and $\text{NA}=0.9$ objective with ANDOR Zyla 4.2 camera, the width of FoV (the longitudinal direction of the fiber) is approximately $L_{\text{FoV}} = 100 \mu\text{m}$. The expected diffusion length of the 50 nm Au nanosphere is roughly $22 \mu\text{m}$ during the recording time of 43 s, meaning that the nanosphere walks over $1/5$ of the entire L_{FoV} , thus the observation time could be further prolonged in general cases for acquiring more frames before the nanoparticle going out of the FoV. Other possible ways to increase the number of frames are to use a camera with a larger sensor, such as Basler with 30 megapixels (the ANDOR camera has a 4.2 megapixels sensor), or choose objectives with lower magnification, sacrificing the resolution, to enlarge the FoV. Our approach can be readily applied to bio-analysis, such as viruses or vesicles, furthermore, possible extensions include the electrostatic interaction-related measurements of the biological objects in liquids^{101,117,118}.

3.6 Chapter Summary

Due to the random nature of the Brownian motion, the high-precision measurements of the nanoparticle's diffusion coefficient necessitate the tracking containing a large

number of frames to achieve high statistical significance. In this work, the presented NBF-based NTA experimentally demonstrates that more than 10^5 frames from a 50 nm single nanosphere (the measured diffusion coefficient is $5.97 \mu\text{m}^2/\text{s}$) can be recorded with the frame rate of 2480 Hz, which is attributed to the nanofluidic channel in the core of a step-index optical fiber. The channel is illuminated by the evanescent field of the mode and can restrict the transverse diffusion of the nanoobjects so that they are forced to stay in the focal depth for a long observing time. Note that even though the hindrance of the nanochannel reduces the measured diffusion coefficient of the nanoobject, the defined resistance factor can correct this impact, which still allows us to determine the hydrodynamic diameter in case of free diffusion (unconfined). The averaged resistance factor is around 1.35 with 560 nm diameter nanochannel and the corrected diameter of the nanosphere is 53 nm (the expected value is 57 nm measured by Zetasizer). By conducting a segmented MSD analysis, we establish a clear correlation between the errors of the determined D and the number of frames per sub-trajectory, which is in good agreement with the CRLB prediction. The findings are compared with previous NTA works, showing that our FaNTA provides a particular advantage in capturing a large number of frames from fast-diffusing nanoobjects.

In outlook, this approach opens up a pathway for determining the size of single nanoobjects with extraordinarily high precision and monitoring dynamic processes of the probes or detecting the information of the fluids¹¹⁹, both of which are useful in living cell analysis¹²⁰, microrheology¹²¹, refractive index sensing¹²².

4 | Nanoparticle Tracking Analysis with Flattened Mode in Nanobore Optical Fiber

It has been demonstrated that FaNTA has advantages in ultralong tracking of label-free and fast-diffusion nanoobjects with significantly high precision. However, the light fields in optical fibers always exhibit spatial distributions, for example, the water-filled NBF has an evanescent field in the fluidic channel. As a result, the signal of scattered light in FaNTA fluctuates as the diffusion motions of the nanoobject. This feature reduces the focal depth of the illumination in the tracking area and limits the detection capability of FaNTA in fast-diffusion nanoobjects. In this work, an approach to creating a light field in the fluidic channel with ideally constant intensity in all three spatial dimensions—a light strand—has been studied and demonstrated by nanoparticle tracking experiments. This concept facilitates the applications of FaNTA such as characterizing the unique shapes of nanoobjects, analyzing nanoscale chemical reactions and rheology, and studying fundamental light-matter interactions.

This chapter is based on the publication by Gui et al.¹²³, reproduced with permission. Copyright 2023, Optica Publishing Group.

4.1 Introduction

The key component of NTA experiments is the establishment of appropriate illumination fields in the volume of the specimens. A method to obtain customized light fields is based on the structured light generation^{124,125}, which has multiple applications in the field of imaging technology, including the needle-shaped beams¹²⁶, light sheets microscopy^{127,128} and 3D fluorescence imaging¹²⁹. Manipulation and shaping of light beams can be achieved through metasurfaces^{130,131}, digital holography^{132,133} and diffractive optical elements¹³⁴. In particular, the concept of flat-top beams^{134–136} could be useful in the context of NTA applications, for which the invariant light fields can effectively improve the depth of focus. However, due to the diffraction of beams in free space, the generation of an ideally constant light field in all three dimensions remains a challenge.

Using optical waveguides can be a strategy to overcome the divergence of beams, as waveguides, unlike the case of free space, confine light rays inside the core, forming the optical modes, and the intensity distribution keeps invariant at any axial position of the waveguide. Note that as long as the cross-section of the waveguide remains identical,

the only factor that can reduce the mode intensity in the propagation direction is the attenuation caused by the optical loss. So far, waveguides with designed nanostructures provide a feasible route to generate tailored modes with nanoscale, examples include strong field enhancement in slot waveguides^{137,138}, the flat-top mode in dielectric slab-waveguide¹³⁹ and nanochannels in optical fibers^{140,141}.

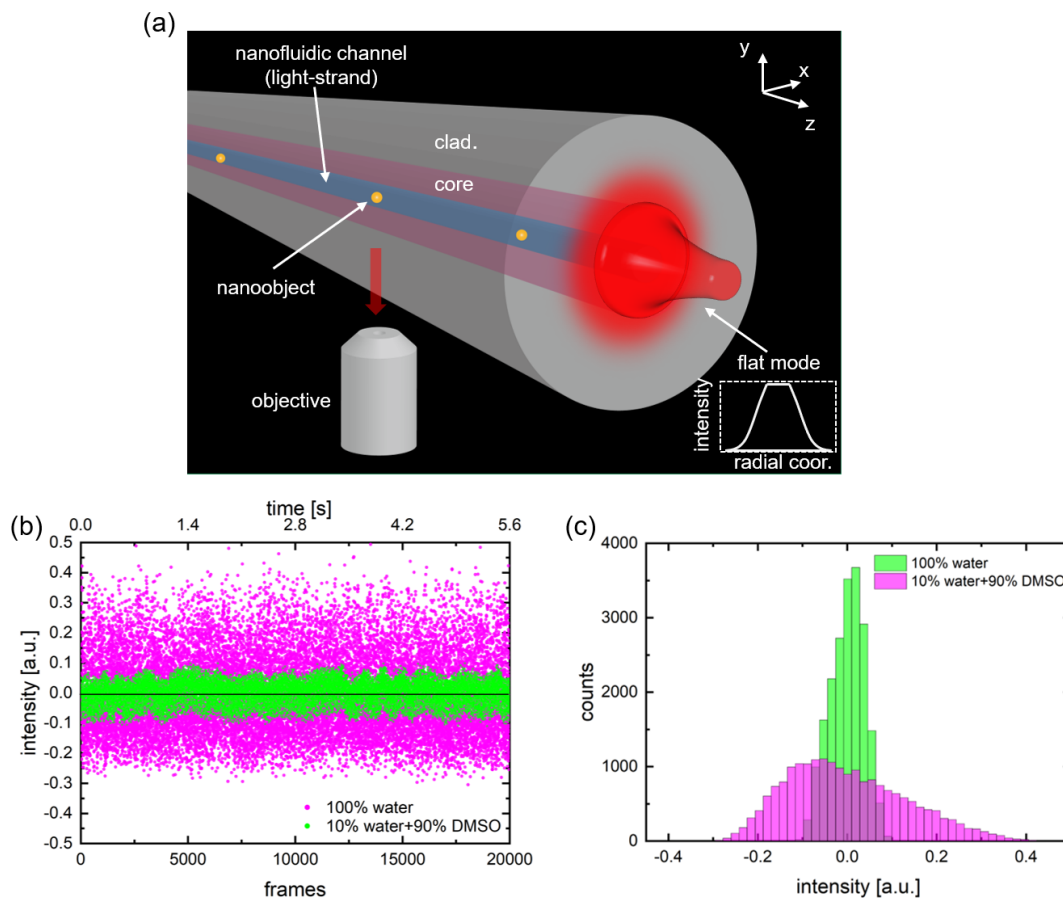


Figure 4.1: Schematic of flattened mode (light strand) formation based on optofluidic nanostructured optical fiber and associated nanoparticle tracking analysis. (a) Illustration of the NBF filled with RI-adjusted liquid, supporting the flattened mode. The blue area refers to the light strand. Scattered light from the nanosphere is collected via objective for the NTA experiment to measure the intensity distribution within the nanochannel. (b) The measured intensities (normalized) scattered by a 50 nm gold single nanosphere diffusing in the nanochannel (filled with RI-adjusted liquid (green) or water (magenta)) as functions of frame index (bottom axis) or time (top axis). (c) Histograms of the measured intensities for those two cases.

In the field of micro-nano photonics, NTA is particularly benefiting from the developments of tailored light fields, examples are the real-time detecting and counting of nanoobjects through optical force¹⁴² and localization of nanoparticles with angstrom precision¹⁴³. In recent years, FaNTA, as an innovative technology combining NTA and optical fiber, has attracted more and more attention^{52,102,103}. As presented in the previ-

ous chapter, the step-index optical fiber with axial nanochannel (NBF) was successfully used to track a 50 nm gold single nanosphere over 100,000 frames⁹¹.

However, one main disadvantage of FaNTA, as well as the free-space configuration, is that the fiber mode intensity decreases rapidly in the transversal directions (evanescent field). As a result, the nanoparticles experience different local intensities during the diffusion motion, and the scattering intensity changes in real-time, which introduces additional variables in the tracking experiment. This feature reduces the localization accuracy of nanoobjects, limits tracking length and, in some cases, such as large-size fluidic channels (radial intensity decreases several orders of magnitude), even truncates the trajectory, all of which degrade the statistical significance of MSD analysis and the accuracy in characterizing specimens. These examples indicate the great demand for flattened fields, ideally keeping constant in all three dimensions.

In this work, an approach is presented to create a flattened mode with ideally constant intensity in all three spatial dimensions—a light strand—based on nanofluidic optical fiber filled with RI-adjusted liquid, shown in Fig. 4.1 (a). This concept integrates the externally accessible nanochannel as well as the flattened fiber mode, allowing for the study of light-matter interactions in nanofluidic environments under the illumination of constant intensity. A single gold nanosphere was used as a probe to detect the modal intensity distribution in the liquid-filled nanochannel via its Brownian motion. The FaNTA results show that scattering intensities exhibit no dependence in arbitrary spatial directions and demonstrate the formation of the light strand in the nanochannel, as shown in Figs. 4.1 (b) and (c).

4.2 Working Principle

4.2.1 Flat-Field Condition

An electric field without radial dependence ($dE(r)/dr = 0$) typically occurs in the core region of a waveguide if a critical condition is satisfied. As a simplified model, the three-layer slab waveguide can be used to derive the flat-field condition. The structure of the slab waveguide and associated parameters are illustrated in Fig. 4.2 (a), where d_i refers to the width of the layers and n_i is the corresponding RI ($i = 1$: central layer; $i = 2$: high RI layer; $i = 3$: outer cladding).

According to the waveguide theory, the electromagnetic fields in the mirror-symmetrical slab waveguide satisfy the wave equation and the TE-polarization modes can be written with trigonometric and exponential functions

$$\begin{cases} E_y^1 = A\cos(k_1x) & 0 < x < d_1/2, \\ E_y^2 = B\sin(k_2x) + C\cos(k_2x) & d_1/2 < x < d_1/2 + d_2, \\ E_y^3 = De^{-k_3[x-(d_1/2+d_2)]} & d_1/2 + d_2 < x, \end{cases} \quad (4.1)$$

where $k_1 = k_0 \sqrt{n_1^2 - n_{\text{eff}}^2}$, $k_2 = k_0 \sqrt{n_2^2 - n_{\text{eff}}^2}$ and $k_3 = k_0 \sqrt{n_{\text{eff}}^2 - n_3^2}$ are the wave vectors in layer 1, 2 and 3 ($k_0 = 2\pi/\lambda_0$, the wave vector in vacuum; n_{eff} , the effective mode index), and A, B, C, D are constants. Note that here the wave vectors are assumed to be real-valued (lossless mode), which means that the RI distribution considered for the guided modes should have $n_2 > n_1 > n_3$.

By applying the continuity boundary conditions of E_y and dE_y/dx on interfaces of the mediums, the dispersion equation corresponding to parameters of the slab waveguide can be derived, reading as

$$k_2 \cos\left(\frac{k_1 d_1}{2}\right) [k_3 \cos(k_2 d_2) - k_2 \sin(k_2 d_2)] = k_1 \sin\left(\frac{k_1 d_1}{2}\right) [k_2 \cos(k_2 d_2) + k_3 \sin(k_2 d_2)]. \quad (4.2)$$

The flattened fields require that the modal intensity is spatially invariant in medium 1, that is, the Poynting vector of the TE mode $S_z^1 = -E_y^1 H_x^1 \propto \cos^2(k_1 x)$ needs to be a constant. It implies that the wave vector $k_1 = k_0 \sqrt{n_1^2 - n_{\text{eff}}^2} = 0$. Thus the flat-field condition is obtained

$$n_1 = n_{\text{eff}}. \quad (4.3)$$

This relation indicates that a flattened field is formed when the effective mode index is equal to the RI of the central medium. From the perspective of waveguides, firstly, the flat-field condition cannot be applied to the modes in single-interface (step-index) waveguides, which indicates the necessity of using multi-layer systems. Furthermore, Eq.4.1 implies that the mode in the flat-field domain equals an associated plane wave that has the same phase velocity as the mode in bulk medium. Due to the constant field distribution, the differential equation describing the field components of medium 1 changes from a wave equation to a second-order ordinary differential equation, and its general solution has the form $E(x) = c_1 + c_2 x$ (c_1 and c_2 are constants). Regarding the symmetry of the slab waveguide geometry, we have $c_2 = 0$ and the field in medium 1 is constant. Insert the flat-field condition Eq. 4.3 into Eq. 4.2, yielding

$$d_2 = \frac{1}{k_2} \left[\arctan\left(\frac{k_3}{k_2}\right) + m\pi \right], \quad (4.4)$$

where $m = 0, 1, 2, \dots$, is an integer number that refers to the mode order in layer 2. This equation specifies the parameters of the slab waveguide designed to achieve the flattened mode.

The calculated d_2 using Eq. 4.4 as functions of wavelength and mode order m are plotted in Fig. 4.2 (b). Numerical simulations have been conducted to validate the flat-field condition. Figs. 4.2 (c) and (d) show the intensity distributions of the modes, in which $m = 0$, $d_2 = 0.657 \mu\text{m}$ and $m = 1$, $d_2 = 3.288 \mu\text{m}$ for the slab waveguide using parameters governed by Eq. 4.4, where $\lambda = 633 \text{ nm}$, $d_1 = 0.4 \mu\text{m}$, and the RI

of the mediums are respectively $n_1 = 1.435$, 1.445 (flat mode) or 1.455, $n_2 = 1.45$ and $n_3 = 1.44$.

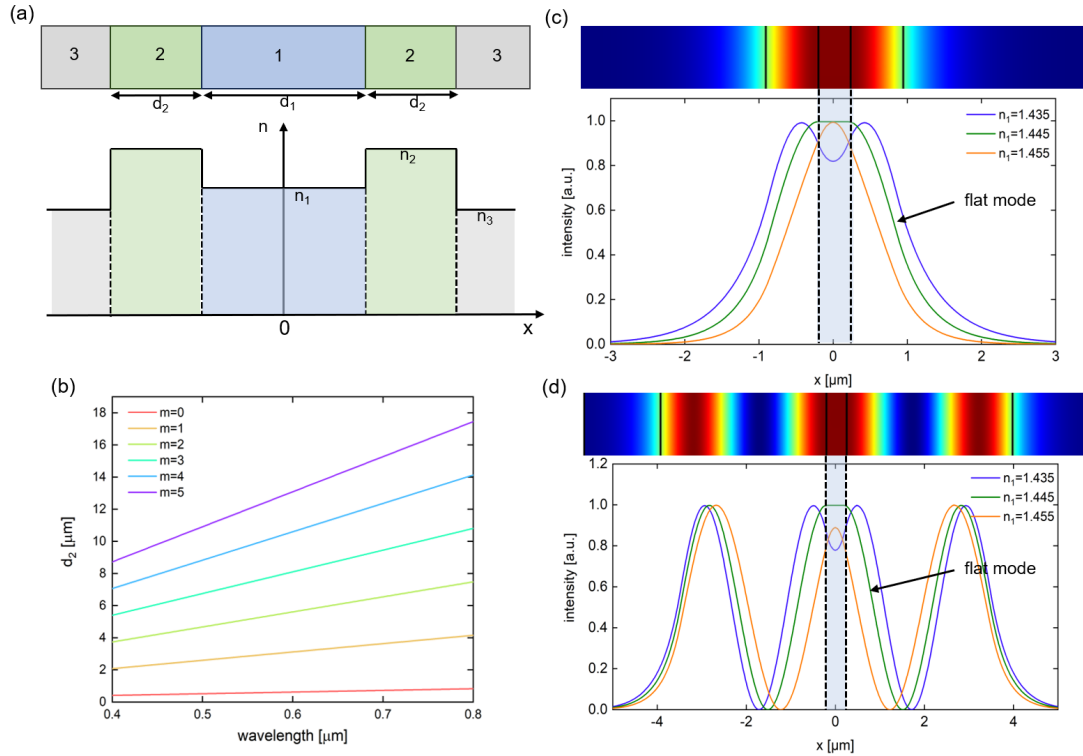


Figure 4.2: The fundamental mode (TE polarization) with flattened fields in a three-layer symmetric slab waveguide. (a) Structure of the slab waveguide with the defined widths and RIs corresponding to the layers. (b) The calculated d_2 as functions of wavelength and the mode order m in the flat-field condition. (c) Calculated modal intensity distributions of the slab waveguide in the flat-field condition, where $m = 0$, $\lambda = 633$ nm, $d_1 = 0.4$ μm , $d_2 = 0.657$ μm , $n_2 = 1.45$ and $n_3 = 1.44$. The values of $n_1 = 1.435$, 1.445 (flat field), and 1.455. (d) The modal intensity distributions for the case of $m = 1$ and $d_2 = 3.288$ μm .

4.2.2 Flattened Mode in NBF

As discussed in the previous section, the flat-field condition is given by $n_{\text{eff}} = n_1$ for TE mode in slab waveguide. This condition can be generalized to optical fiber. Considering the weakly guiding fiber, the modes in this case are quasi-TEM waves, where the fundamental modes are denoted as LP_{01} modes (see section 2.1.1). The transversal fields of LP_{01} mode are azimuthally independent ($m=0$) and satisfy the scalar wave equation, $[\nabla_{\text{t}}^2 + k_0^2 n^2 - \beta^2]\psi_{\text{t}} = 0$, where ∇_{t}^2 is the transversal Laplacian in cylindrical coordinates⁷⁹. Therefore, by using the relations of the flattened mode,

$d\psi_t/dr = 0$ and $n_{\text{eff}} = n_1$ (note that the wave equation still holds), the expressions of the flat fields in NBF can be expressed as

$$\psi_t(r) = \begin{cases} A, & 0 < r < a \\ BJ_0(k_{21}r) + CY_0(k_{21}r), & a < r < b \\ DK_0(k_{31}r), & b < r \end{cases} \quad (4.5)$$

where $k_{21} = k_0\sqrt{n_2^2 - n_1^2}$ and $k_{31} = k_0\sqrt{n_1^2 - n_3^2}$. Here we apply the continuity boundary condition for ψ_t and $d\psi_t/dr$ respectively on $r = a$ and $r = b$, then the coefficients matrix M is obtained as below

$$\begin{bmatrix} 1 & -J_0(k_{21}a) & -Y_0(k_{21}a) & 0 \\ 0 & J_0(k_{21}b) & Y_0(k_{21}b) & -K_0(k_{31}b) \\ 0 & k_{21}J'_0(k_{21}a) & k_{21}Y'_0(k_{21}a) & 0 \\ 0 & k_{21}J'_0(k_{21}b) & k_{21}Y'_0(k_{21}b) & -k_{31}K'_0(k_{31}b) \end{bmatrix}. \quad (4.6)$$

Let $\det[M] = 0$ and rearrange the equation, yielding

$$\frac{J'_0(k_{21}a)}{Y'_0(k_{21}a)} = \frac{k_{21}K_0(k_{31}b)J'_0(k_{21}b) - k_{31}K'_0(k_{31}b)J_0(k_{21}b)}{k_{21}K_0(k_{31}b)Y'_0(k_{21}b) - k_{31}K'_0(k_{31}b)Y_0(k_{21}b)}. \quad (4.7)$$

The above equation associates the fiber parameters supporting a flat field. Note that the flattened mode can only exist in a multi-layer structured waveguide (at least three layers), due to the continuity of the derivative of the fields. Eq. 4.7 is a transcendental equation corresponding to the parameters of n_1 , n_2 , n_3 , a , and b , and this relation could be the design principle to obtain the flattened mode in NBF. In addition to the theory model, finite element method (FEM) simulation is another effective way to the mode analysis for optical fibers. In this thesis, the simulations were carried out by using COMSOL Multiphysics 5.2.

4.2.3 Numerical Simulation

Fig. 4.3 (a) shows the solved core radius b as a function of wavelength for the flat fields using Eq. 4.7 where $a = 200$ nm, $n_1 = 1.445$, $n_2 = 1.45$ and $n_3 = 1.44$. At the wavelength of 0.632 μm , the related $b = 1.384$ μm (noted as the red dot), supporting the LP_{01} mode, and the simulated modal distribution is shown in Fig. 4.3 (b), where the numerically obtained $n_{\text{eff}} = 1.44498$. In the next sections, the flattened mode is demonstrated by FaNTA experiments using RI-adjusted NBF. The mode shapes near the flat-field condition (Gaussian or evanescent) depend on n_1 ($n_1 > n_{\text{eff}}$ or $n_1 < n_{\text{eff}}$), thus various applications based on this mechanism can be developed, such as temperature sensing and RI measurements in nanoscale.

The flat-field condition of NBF has been discussed and Eq. 4.7 is derived to give the combination of the demanded fiber parameters. Here, it experimentally demonstrates

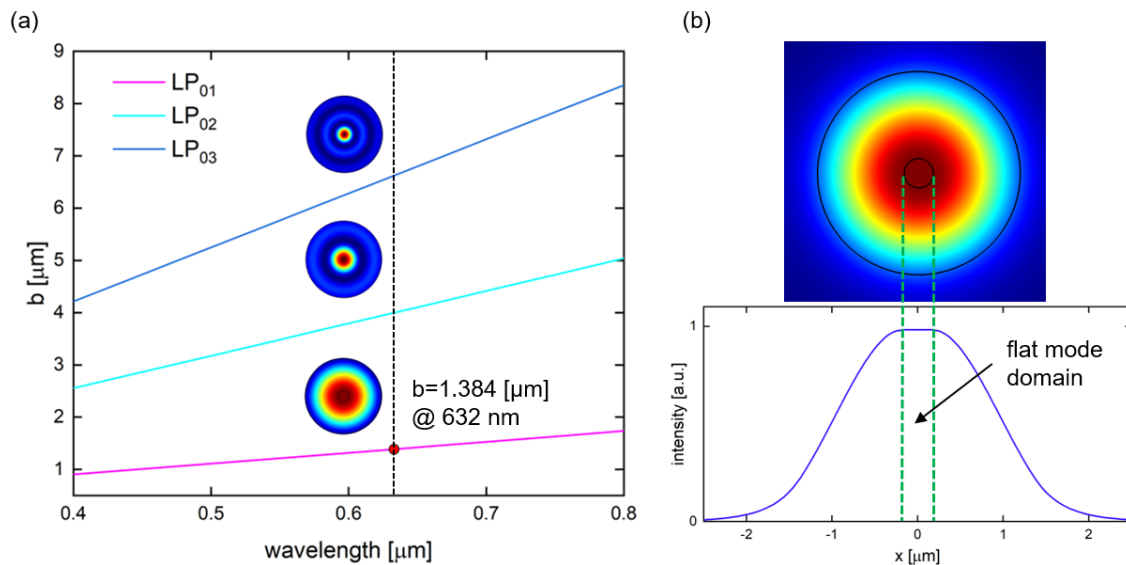


Figure 4.3: Flat fields in NBF. (a) Calculated b as functions of the wavelength, where $a = 200$ nm, $n_1 = 1.445$, $n_2 = 1.45$ and $n_3 = 1.44$. (b) The simulated intensity distribution of the flattened LP_{01} mode, which refers to the red dot in (a).

the light strand by using NBF filled with RI-adjusted liquid, which is a suitable system for achieving the flat-field condition. The used NBF is a silica step-index fiber, consisting of a fused silica cladding ($n_3 = 1.457$ at wavelength $\lambda_0 = 632$ nm, and the outer diameter is 125 μm) and optical core (GeO₂-doped fused silica with doping concentration 5.3 mol./%, $n_2 = n_3 + \Delta n$, $\Delta n = 8 \times 10^{-3}$, core radius $b = 1.5$ μm) which contains a nanobore (radius $a = 200$ nm) in the center of the cross-section. The fiber was designed and fabricated in collaboration with Heraeus Quarzglas GmbH & Co. KG and has been applied in previous FaNTA-related works^{52,91}.

To establish a flat field, the RI of the nanochannel was numerically determined using finite element simulations, and the value of n_1 could be precisely tuned by mixing water and DMSO with different concentrations¹⁰⁶, for example, $n_1 \approx 1.4646$ when the water/DMSO mixture is 9/91 wt%. Figs. 4.4 (a), (b), and (c) show the configurations of the used NBF and the simulated flattened mode by filling with the RI-adjusted liquid ($n_1 = n_{\text{eff}} = 1.46088$). Fig. 4.4 (d) shows the intensity profiles of both RI-adjusted and the water-filled cases ($n_1 = 1.3317$) on the central line, where an evanescent field forms in the water-filling nanobore.

The fabrication of the NBF is based on the high-temperature fiber drawing of a doped silica rod containing a central hole, and the SEM image of the cross-section is shown in Fig. 4.4 (b). The liquid-filled NBF works in single mode at 632 nm and is thus insensitive to bending (more information on the NBF can be found in the reference¹⁰⁴.). The dispersion relations of the modes in liquid-filled NBF have been studied using finite element simulations by COMSOL Multiphysics 5.2. Fig. 4.4 (a) shows the results of

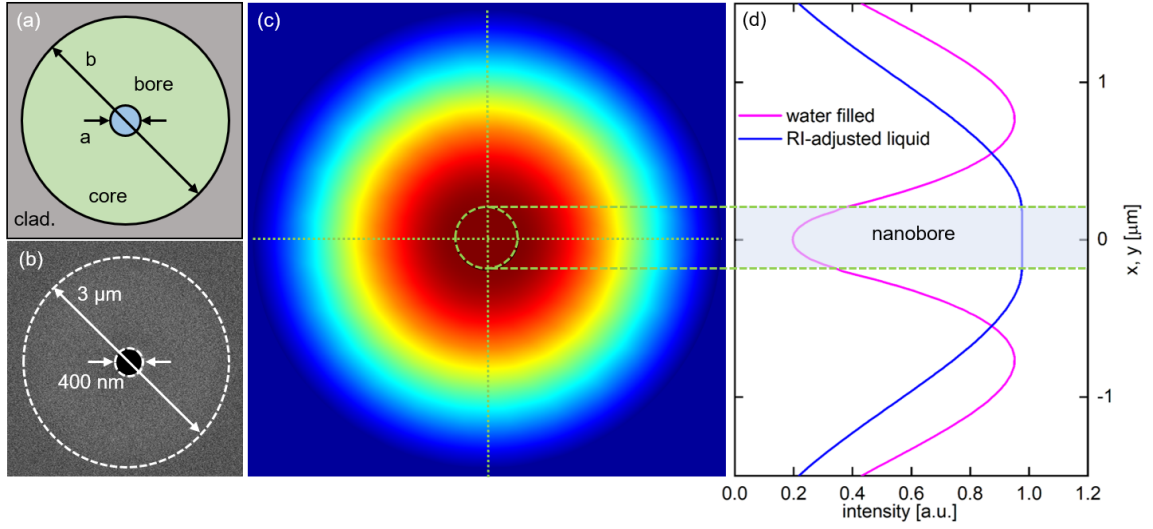


Figure 4.4: The fundamental mode with flattened fields in NBF filled with RI-adjusted liquid. (a) Schematic of the NBF cross-section with the defined nanobore (blue), core (light green), and cladding (gray). (b) SEM image of the used NBF, the measured diameters of the nanobore and core are 400 nm and 3 μm , respectively. (c) Simulated modal distribution of the fundamental mode with flattened fields, where $\lambda = 632 \text{ nm}$ and $n_1 = n_{\text{eff}} = 1.46088$. (d) Modal distributions along vertical central lines, which are measured from the flattened mode in (c) and corresponding to the fibers filled with water or RI-adjusted liquid. The light blue area indicates the domain of the nanobore, showing an evanescent (magenta) or a flat field (blue).

the fundamental mode (HE_{11}) and the first higher-order modes (TE_{01} , TM_{01} , HE_{21}). In the simulation, the dispersion of DMSO/water solution is negligible¹⁴⁴, and the RI

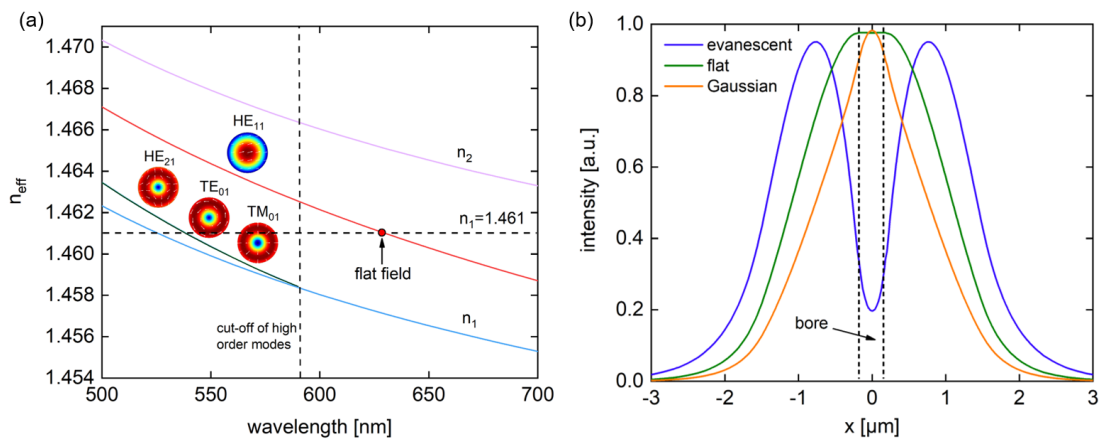


Figure 4.5: Mode simulations of liquid-filled NBF. (a) Calculated effective mode indexes of the first four order modes in the liquid-filled NBF, in case the RI of the liquid is fixed to 1.461. The NBF is working in single mode when $\lambda > 590 \text{ nm}$. The flattened mode is obtained when $n_{\text{eff}} = n_1$ at $\lambda = 632 \text{ nm}$. (b) Three types of modes in NBF: evanescent (blue, $n_1 = 1.33$); flat (green, $n_1 = n_{\text{eff}} = 1.461$); Gaussian (yellow, $n_1 = 1.48$).

is fixed as $n_1 = 1.461$, with which the fundamental mode has almost flattened intensity distribution at $\lambda = 632$ nm. The RI of the fused silica (n_3) is determined using the Sellmeier equation¹⁴⁵. The RI of the GeO₂-doped fused silica core (doping level is 5.3 mol%) is higher than that of the cladding with an amount of $\Delta n = 8 \times 10^{-3}$ at all considered wavelengths. The radii of the bore and core are respectively $a = 200$ nm and $b = 3$ μm .

As shown in Fig. 4.5 (a), the cut-off wavelength of the single-mode is $\lambda = 590$ nm. Note that the n_{eff} of the fundamental mode is larger than n_1 until the cross point at 632 nm, where the flat-field condition is met. Based on the numerical simulation, a general routine to find out the flattened mode in waveguides is to calculate the n_{eff} by scanning the parameters until the point of $n_{\text{eff}} = n_1$ is obtained. Fig. 4.5 (b) shows other two cases that n_1 is larger ($n_1 = 1.48$) or smaller ($n_1 = 1.33$) than n_{eff} , leading to a Gaussian or evanescent modes. In the next section, experiments with tuning the RI of liquids by temperature controlling are carried out to observe the transition from the Gaussian to evanescent modes.

To reveal the influence of the mismatch of the liquid RI on the flat-field condition, we calculated the modal profile for different radii of the nanochannel as functions of n_1 (the RI of liquid). The results are shown in Fig. 4.6.

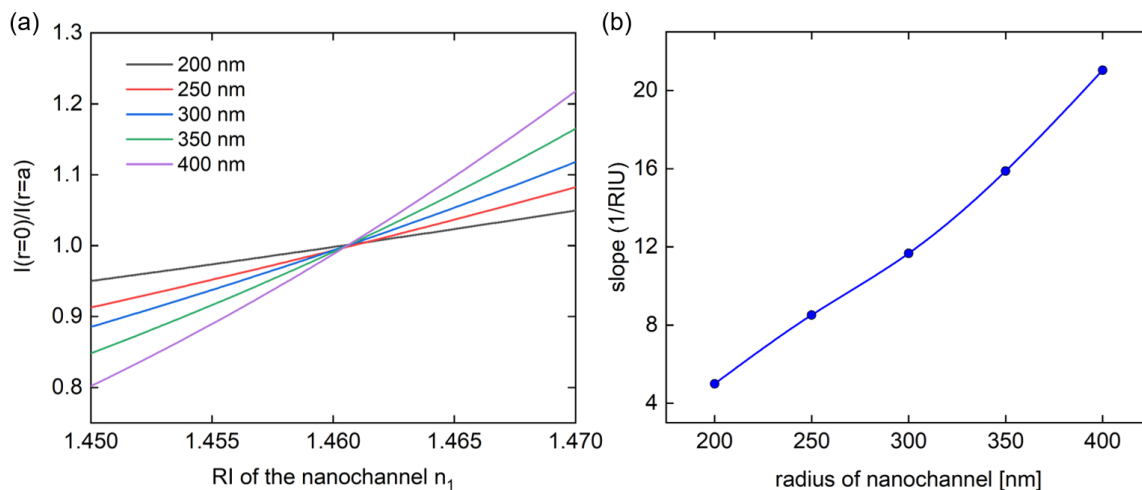


Figure 4.6: The influence of the RI mismatch on the flatness of the modal fields within the nanochannel. (a) The ratio of the intensity at the center and the liquid-wall interface, $K = I(r = 0)/I(r = a)$, as functions of the nanochannel's radius and its RI n_1 . (b) The slope of $K(n_1)$ as a function of the nanochannel's radius.

Here, a benchmark K is defined to qualify the flatness of the mode within the nanochannel, which is the ratio of the modal intensity at the center ($r = 0$) and the liquid-wall interface ($r = a$), that is, $K = I(r = 0)/I(r = a)$. We can expect that $K < 1$, $K > 1$, or $K = 1$ correspond to the evanescent, Gaussian, or flattened modes,

respectively. Fig. 4.6 (b) indicates that the smaller diameter of the nanochannel leads to less sensitivity to the mismatch of the RI since the modal fields change across a shorter distance.

4.3 Results

4.3.1 Diffusion Length Estimation

The formation of light strands in optofluidic NBF is verified through FaNTA experiments, from which the basic idea is to measure the scattered light intensities of a single nanosphere diffusing inside the nanofluidic channel. The inherent feature of a light strand is that the field keeps a constant at all positions within the channel, thus the light intensity scattered from a single nanoparticle should not vary with the diffusing motions, as a result, the statistical histogram of the intensity signal has a narrower distribution compared to the case of a non-flat field. Note that the histogram has an intrinsic width (approximately Gaussian) even though the mode is flattened, which is due to the noise of the imaging system and can be qualified by measuring a static particle in the nanochannel.

To demonstrate this feature, the in-plane positions of a freely diffusing golden nanosphere (mean physical diameter: 50 nm, nanoComposix) inside the nanochannel are tracked, and the corresponding scattered intensity (details of the specimen and the FaNTA setup can be found in the section of temperature scan). Note that for accurate sampling of the light intensity within the nanochannel, the nanoparticle should occupy the cross-section positions as many as possible in a single trajectory. In the presented experiment, FaNTA allows observation of a single nanoparticle over an extraordinarily long trajectory and duration⁹¹, thus providing high statistical significance in retrieving the modal distribution. Here we estimate the number of times that a nanoparticle travels the cross-section of the nanochannel, N_τ . For a nanosphere diffusing in liquid, the diffusion coefficient can be calculated using the Einstein-Stokes relation, thus $D = K_B T / 6\pi\eta r$. Then N_τ can be estimated as

$$N_\tau = \frac{2a}{x_{\text{dif}}}, \quad (4.8)$$

where a is the radius of the nanochannel, $x_{\text{dif}} = \sqrt{2D\tau}$ is the diffusion length in observation time τ . Given the experimental parameters (more details are listed in Table 4.1), a 50 nm nanosphere can travel cross the nanochannel 24.4 times during the time of 5.57 s, which provides sufficient statistical reliability to resolve the modal distribution in this work.

Parameter	Symbol	Unit	Value
frequency	ν	Hz	3592
no. frames	N_f	1	20000
observation time	τ	s	5.57
viscosity	η	mPas	1
temperature	T	K	293
nanosphere diameter	d_N	nm	50
diffusion coefficient	D	$\mu\text{m}/\text{s}$	8.58
diffusion length	x_{dif}	μm	9.78
nanochannel radius	a	nm	200
no.times nanoparticle travel through cross-section	N_t	1	24.4

Table 4.1: Used parameters to estimate the diffusion length and the number of times the nanoparticle travels through the cross-section of the nanochannel.

4.3.2 Experimental Setup

Fig. 4.7 shows the optical setup used for the experiment. The 632 nm laser was coupled into the fiber through a polarizer (polarization direction is along the x direction) and an objective lens (40 \times , NA=0.65, Olympus). The NBF was placed below the Peltier

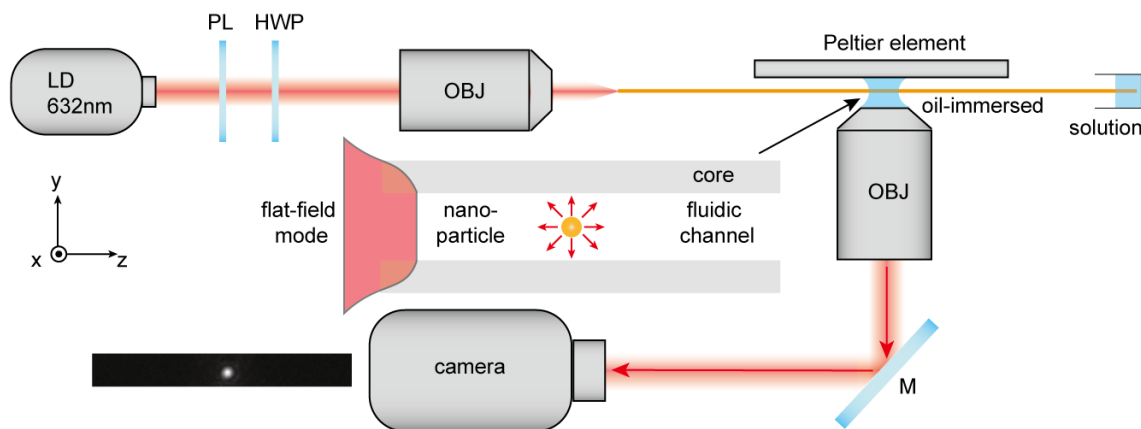


Figure 4.7: Schematic of the FaNTA experimental setup. LD: laser diode, PL: polarizer, HWP: half-wave plate, OBJ: objective lens. The inset in the center of the figure shows the elastic light scattering process of the nanosphere inside the nanochannel. The bottom left inset shows one of the diffraction-limited images of the nanosphere on the focal plane.

element with a distance of 1 mm (from the fiber to the heating surface), and a Bragg grating sensor (accuracy ± 0.5 K) was used for the temperature calibration. The scattering light from a single nanosphere was collected by an oil-immersed objective (60 \times , NA=1.25, UplanFl Olympus) and imaged in a CMOS camera (ANDOR Zyla 4.2 Plus, scale: 72.6 nm/pixel) with the exposure time $t_e = 0.08$ ms and the frame rate $\nu = 3592$ Hz. Glycerin was used as the immersion oil filled between the Peltier element and the

objective lens, which also served as a heat transfer medium. The sample of nanosphere suspension was filled into the nanochannel through capillary effect and the tip of the NBF was sealed using plasticine after the filling was completed.

4.3.3 Modal Distribution Measurement

The intensity of scattered light from FaNTA remains constant in case the modal fields are ideally flattened, however, due to background noise and RI mismatch of the liquid, the signal always fluctuates as the movements of nanoparticles inside the nanochannel. To characterize the modal intensity distribution, two spatial regions, noted as the side bin (SB) and central bin (CB), as shown in Fig. 4.8, are defined in the cross-section of the nanochannel, and the scattered intensities of the tracked nanoparticle with the locations in the SB and CB are then analyzed, so that shape of the mode distribution can be judged. From the data set of the FaNTA experiment, one can obtain the single nanoparticle's positions along both transversal (x -values) and longitudinal (z -values) directions with the associated scattered intensities. Regarding the symmetry of the circular cross-section, the averaged value of x has been subtracted, so that the data is centralized to 0. Figs. 4.9 (a) and (b) show the intensities corresponding to the x -positions for the experiment and simulation, respectively, as an example of the water-filled NBF. Then we find the maximal of the x -values $\max(x)$, which should equal the radius of the nanochannel. Finally, pick up the intensity data points of which the x -values are located in the CB ($|x| < r_1 \max(x)$) or SB ($|x| > r_2 \max(x)$), respectively. Here, $r_1 = 0.2$ and $r_2 = 0.6$, yield an 80 nm width to both the CB and SB. The chosen width provides a 30% relative separation of the CB and SB histograms in the water case, which is a proper reference for this analysis.

Statistical analysis, using histograms and non-parametric kernel density estimations, is performed on the data points in the SB and CB separately. Based on the histograms analysis, the following parameters can be defined: (1) the intensity at which the histogram gives the highest probability is noted as I_{\max}^{bin} ; and (2) the full-width-half-maximum (FWHM) of the intensity distribution, that is, the width between the intensities that drop to half of the highest probability, $p = p_{\max}/2$, is noted as $\Delta I_{\text{FWHM}}^{\text{bin}}$ (bin: SB or CB). All of the intensities presented in the histograms have been normalized corresponding to the intensity that has the highest probability in CB. To describe the shape of the measured mode, the relative distance between the peaks of the CB and SB histograms is defined as $\delta I_{\max} = (I_{\max}^{\text{CB}} - I_{\max}^{\text{SB}})/I_{\max}^{\text{CB}}$. This analysis is based on the fact that the sign of δI_{\max} (plus or minus) can refer to the mode types in the nanochannel of NBF. On the one hand, if the fields are evanescent ($n_1 < n_{\text{eff}}$), intensities sampled from the SB are higher than that from the CB, leading to a larger peak of the SB-histogram, thus, $\delta I_{\max} < 0$, on the other hand, if fields are Gaussian-shaped ($n_1 > n_{\text{eff}}$), we have

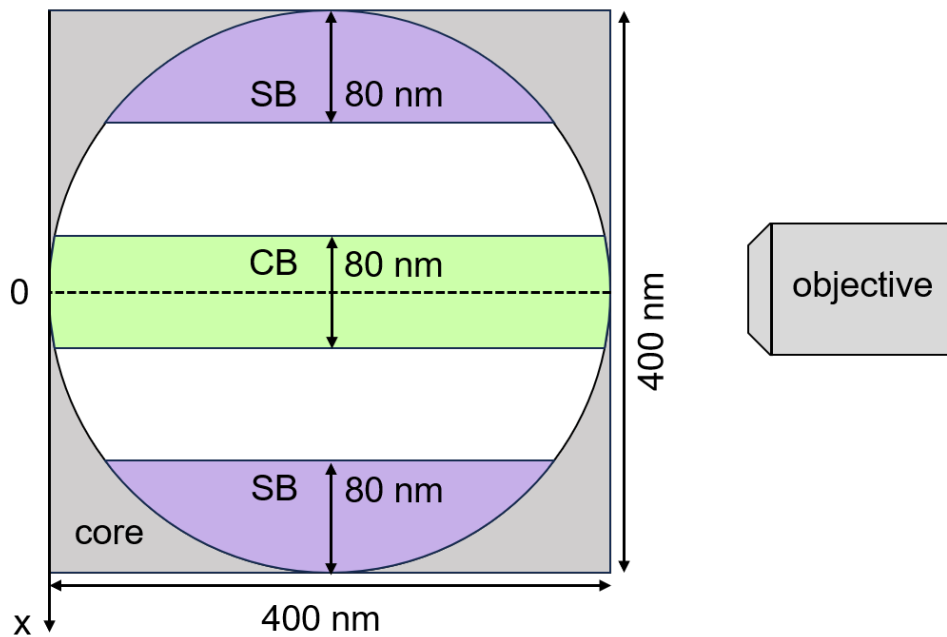


Figure 4.8: Definition of the bins for mode analysis. The cross-section of the nanochannel is divided into two spatial regions in the x -direction, noted as CB (light green) and SB (light purple).

$\delta I_{\max} > 0$. In the following, the segmented analysis is applied for two cases: evanescent mode in water-filled NBA; and near-flat mode in RI-adjusted NBF.

4.3.4 Case 1: Water-Filled NBF

Firstly, the NBF was filled with gold nanospheres ($d=50$ nm, concentration is 4.2×10^{10} particles/ml, ultrauniform, nanoComposix) suspended in water of which the RI is $n_1 = 1.3317 < n_{\text{eff}}$, thus the modal distribution in the nanochannel should be evanescent. The data of FaNTA experiments are processed by using the segmented analysis and the results are shown in Fig. 4.9 (c). The intensity histograms of CB and SB have separating maximum probabilities, and SB has obviously higher intensity than CB, that is, $I_{\max}^{\text{SB}} > I_{\max}^{\text{CB}}$ and $\delta I_{\max} = -0.332$. The results indicate that the modal intensity on the sides of the channel is larger than that in the central area, and this is a typical feature of an evanescent field, which is also in agreement with the results of the simulation, shown in Fig. 4.9 (d). The bandwidths of the histograms, $\Delta I_{\text{FWHM}}^{\text{SB}} = 0.251$ and $\Delta I_{\text{FWHM}}^{\text{CB}} = 0.275$ are relatively high, which is due to the spatial dependence of the evanescent field in the channel. Thanks to the confinement of the nanochannel, a large number of frames can be recorded, which is a key advantage of FaNTA, leading to sufficient data points in the CB and SB, where $N_{\text{CB}} = 6715$ and $N_{\text{SB}} = 579$.

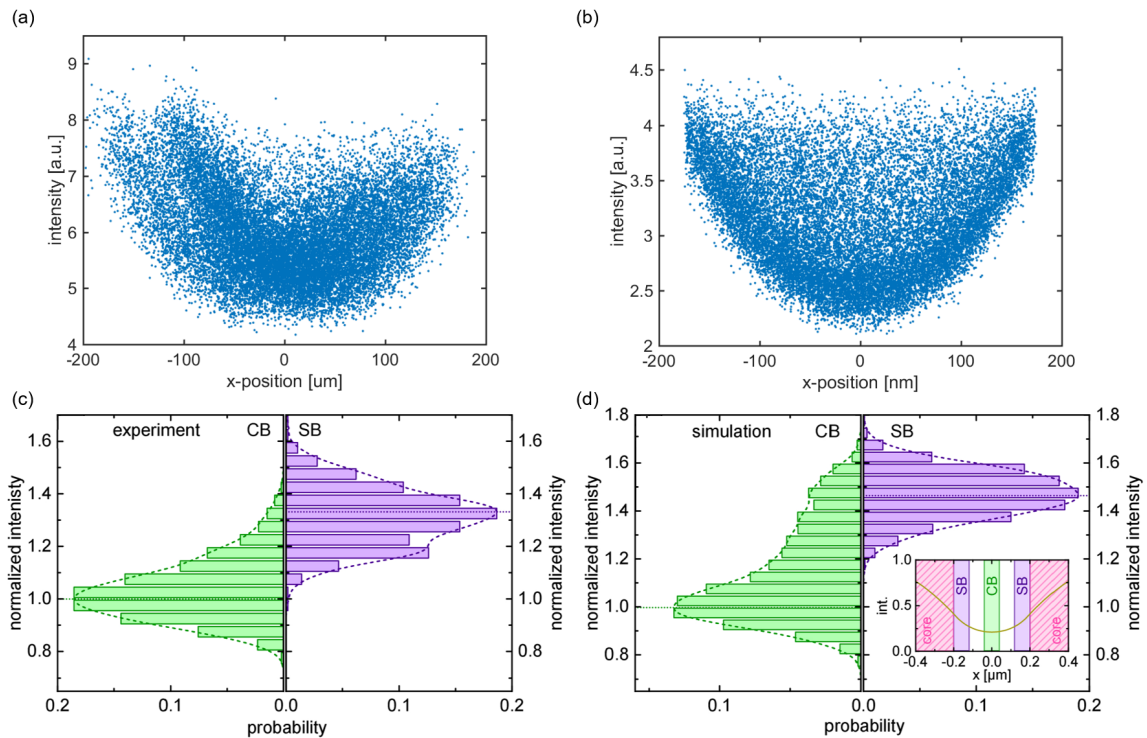


Figure 4.9: A representative example of the statistical analysis for the modal fields in the water-filled NBF. The intensity data is sampled by elastic light scattering from a nanosphere ($d = 50$ nm) diffusing in the nanochannel. The intensities and the corresponding x -positions were obtained from (a) experiment and (b) simulation. Histograms of the probability distribution of the scattered intensities in the CB (green) and SB (purple) defined in Fig. 4.8, obtained from (c) experiment and (d) simulation. The number of data points in the histograms are $N_{\text{CB}}^{\text{exp}} = 6715$, $N_{\text{CB}}^{\text{exp}} = 579$, $N_{\text{CB}}^{\text{sim}} = 4771$ and $N_{\text{CB}}^{\text{sim}} = 2263$. The inset in (d) shows the simulated line modal distribution in the water-filled channel ($n_1 = 1.3317$).

4.3.5 Case 2: RI-adjusted Liquid and Temperature Scan

We performed FaNTA experiments in NBF to verify the flat-field condition by using dimethyl sulfoxide (DMSO) aqueous solution of which the RI can be adjusted by mixing DMSO and water with different ratios. Furthermore, the RI of the liquid in the nanochannel is finely tuned based on the thermo-optic effect by using a Peltier element to control the temperature of the fiber, so that a series of RI above or below the flat-field condition can be achieved.

The temperature-dependent RI of the DMSO aqueous solution is assumed as a liner function, that is, $n(\lambda, c_m) = n_0(\lambda, c_m) + \Delta n_T \cdot (T - T_0)$, where $n_0(\lambda, c_m)$ is the dispersion of the mixture at a reference temperature T_0 and wavelength of λ , c_m is the ratio of DMSO weight in the mixture (e.g., $c_m = 100$ wt%: pure DMSO), and Δn_T is the thermo-optic coefficient, which can be obtained from the literature¹⁴⁴. The

authors present an empirical relation to calculate the temperature-induced changes of RI $\Delta n_T = -(\frac{dn}{dT} \cdot 10^{-4})$, where

$$\frac{dn}{dT} = -0.0000116c_m^2 + 0.0429c_m + 1.0837. \quad (4.9)$$

The liquid filled into the fiber was a mixture of DMSO and in-water suspending gold nanospheres ($d=50\text{nm}$, concentration is 4.2×10^{10} particles/ml, ultrauniform, nanoComposix), where the weight ratio $c_m=91$ wt%, and the RI is $n_1 = 1.4646$ at $\lambda = 632$ nm and 21°C (more information can be found in section 4.5.1). The calculated RIs of the DMSO/water mixture as a function of the weight ratios and temperatures are plotted in Fig. 4.10.

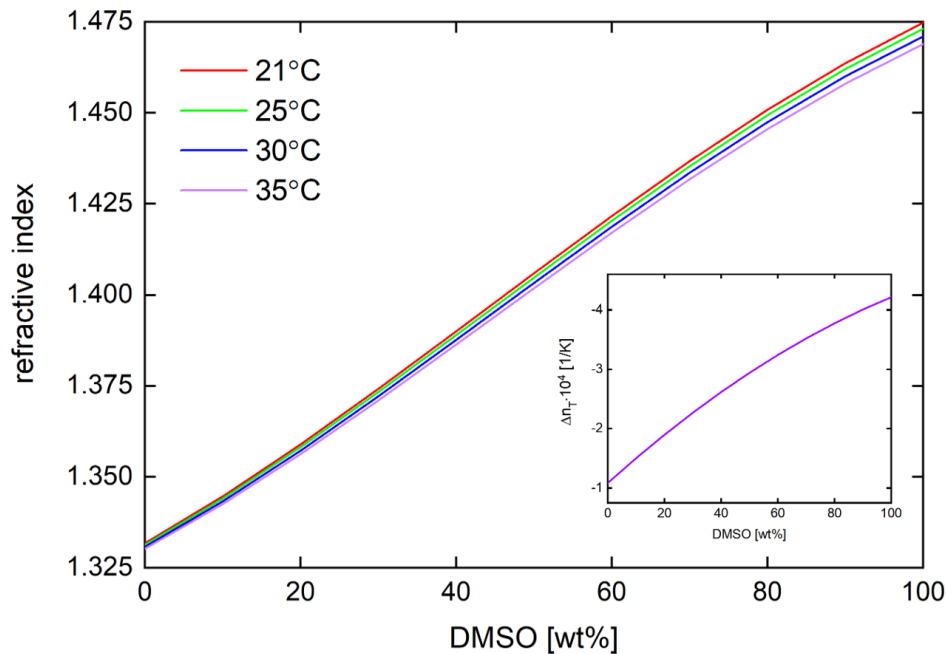


Figure 4.10: RIs of DMSO/water mixture as functions of the ratio of the weight between DMSO and water with different temperatures at the wavelength of 632 nm, which are calculated by using Eq. 4.9.

Similar to Fig. 4.9, the experimental results of the temperature scan are presented by using the CB/SB histogram analysis, which is shown in Fig. 4.11 (a) (the intensities associated with the x -positions used for the estimations can be found in Fig. 4.14 in section 4.5). Both probability histograms of the CB and SB show well-symmetric distributions centering to I_{\max}^{bin} , which is unlike the results of the water-filled case. The probability histograms correspond to the sampled intensities and appear as Gaussian-like distributions, demonstrating that the spatial variation of the intensity is quite small in the nanochannel. Note that even in the case of an ideally constant field, it is supposed to observe a Gaussian distribution in the histogram of the measured intensi-

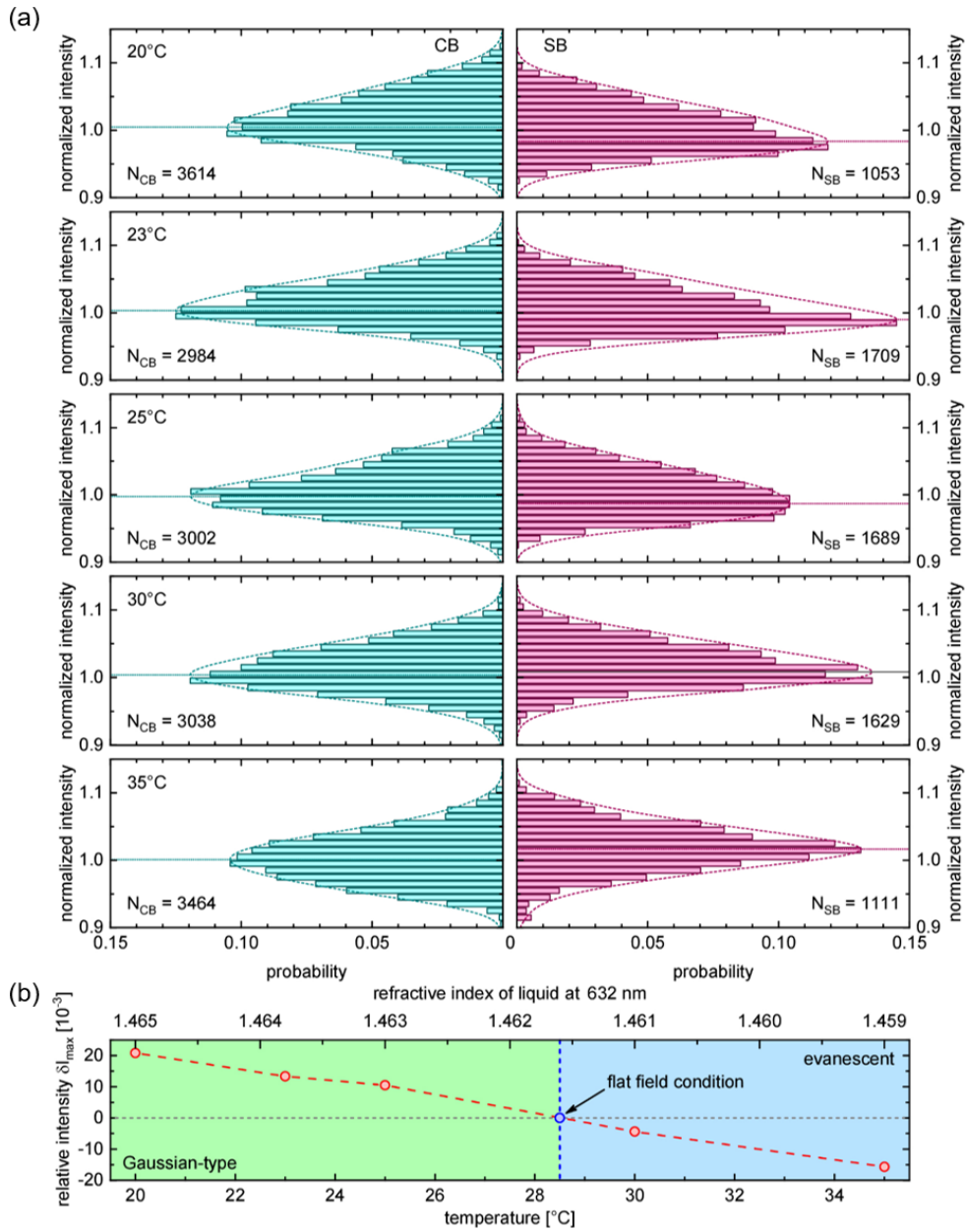


Figure 4.11: Statistical analysis of the FaNTA experiments with the RI of liquid (9 wt. % water and 91 wt. % DMSO mixture) tuned by temperature scan to determine the flat-field conditions. (a) Histograms of the CB and SB with temperature of 20, 23, 25, 30, 35 °C. The number of intensity points used in each histogram is noted as N_{CB} or N_{SB} . The dotted horizontal lines indicate the positions of the histogram peaks I_{\max}^{bin} . (b) The relative shifts of the peaks $\delta I_{\max} = (I_{\max}^{\text{CB}} - I_{\max}^{\text{SB}})/I_{\max}^{\text{CB}}$ as a function of temperatures (bottom axis) and RI of the liquid (top axis). The temperature at which the flat field condition occurs is determined by the linear interpolation of the two points beside. The colored backgrounds refer to the types of the mode near the flat field condition (light green: Gaussian-type, light blue: evanescent-type).

ties, since some inevitable noise, such as the background scattering and readout noise of the camera, can broaden the intensity distribution. In the simulation, noise-induced

broadening can be performed by adding Gaussian noise in the generated intensities from the random walk in a circular area.

A comparison of the statistical benchmarks between the water and RI-adjusted cases can be found in Table 4.2. It shows that the intensity bandwidth of the RI-adjusted mixture ($\Delta I_{\text{FWHM}}^{\text{bin}} = 0.093$, intensities range from 0.85 to 1.15) is obviously narrower than that of the pure water case ($\Delta I_{\text{FWHM}}^{\text{bin}} = 0.26$, intensities range from 0.65 to 1.7). Another notable difference is the distance between the peaks of CB and SB histograms, defined as $\delta I_{\text{max}} = (I_{\text{max}}^{\text{CB}} - I_{\text{max}}^{\text{SB}}) / I_{\text{max}}^{\text{CB}}$. The δI_{max} of RI-adjusted experiments are over 10 times smaller than that of the water case (RI-adjusted: $\delta I_{\text{max}} = 0.02$; water: $\delta I_{\text{max}} = 0.332$, see Table 4.2). All of these results straightforward indicate a modal field with less spatial dependence occurring in the RI-adjusted nanochannel.

Case	ΔI	$\Delta I_{\text{FWHM}}^{\text{CB}}$	$\Delta I_{\text{FWHM}}^{\text{SB}}$	δI_{max}
water	0.65~1.70	0.275	0.251	-0.332
RI-adjusted liquid	0.85~1.15	0.096	0.091	-0.015~0.02

Table 4.2: Comparison of the benchmarks between the water-filled and RI-adjusted FaNTA experiments. Note that the $\Delta I_{\text{FWHM}}^{\text{bin}}$ of the RI-adjusted case is the average value from all of the temperatures.

The temperature scanning experiments are based on the fact that the mixed solution of DMSO and water has a negative thermo-optic coefficient (see Fig. 4.10), that is, the increasing of temperature results in a decrease of RI (n_1). Although the changes of the modal fields near the flat-field condition are quite small, thanks to the statistical analysis, the relative shifts between peaks of the CB and SB histograms δI_{max} can still be observed (the value is around 1%), as shown in Fig. 4.11 (b). This is evidence that directly reveals the transition of the mode types in the nanochannel. The sign of δI_{max} changes from plus to minus, indicating that the modal field transfers from a Gaussian-type ($n_1 > n_{\text{eff}}$) to an evanescent-type distribution ($n_1 < n_{\text{eff}}$) within the nanochannel. The temperature at which the mode becomes flattened in the nanochannel is $T \approx 28.5^\circ\text{C}$, plotted as the blue dot in Fig. 4.11 (b), and the corresponding $n_1 \approx 1.4616$.

Simulations are performed to verify the temperature measurements (see Fig. 4.17 for details), and the results are highly consistent with the experimental data. In particular, the relative shifts of the CB/SB histogram peaks depending on the temperatures, $\delta I_{\text{max}}(T)$, are in good agreement with the results shown in Fig. 4.11 (b). Compared with the experiments, the temperature of the flat-field condition in the simulation occurred at $T_{\text{flat}}^{\text{sim}} = 30.45^\circ\text{C}$, and the in the experiment is at $T_{\text{flat}}^{\text{sim}} = 28.5^\circ\text{C}$. The deviations can be attributed to the difference between the assumed parameters in the simulation and the actual geometry of the used fiber. In addition, the intensity distributions in the simulation are narrower than those in the experiment, which is due to the inevitable errors in the experiment, such as the localization uncertainty during the exposure time.

4.4 Discussion

To clarify the properties of flat-field in nanochannel with different sizes, we performed numerical simulations (see Fig. 4.6). It shows that the modal intensity has less change with the mismatches of RI in smaller nanochannels, which means that it provides more error tolerance in the preparation of the liquids for the achievement of flattened mode. The used NBF in the NTA experiments relies on the weakly guiding approximation (the RI contrast between the core and cladding is small), and the fundamental mode has no azimuthal dependence so that the flat-field condition can be satisfied not only in the longitudinal direction but also along the radial directions. However, for large RI contrast, the situation is different, since the fiber could be multimode. Therefore, further studies are needed to clarify the behaviors of the flat-field mode in case the fiber has different geometry or RI configurations.

This work demonstrates the generation of a flat-field mode—the light strand—in the fluidic channel of NBF, leading to the illumination with constant intensity in all three spatial directions in the tracking area. This will effectively improve the depth of focus for NTA experiments and prevent interruptions of trajectory recordings arising from the diffusion motions of nanoparticles to the spatial area with low-intensity illumination (e.g., the edge of the nanochannel). It also eliminates the correlation between the signal intensity and the locations of nanoobjects in the nanochannel. As a consequence, the scattered intensity from a single nanoobject could be used as an independent parameter to extract some of the intensity-related information, such as the rotational dynamics of non-spherical nanoparticles, as well as the RI and morphological analysis, which opens up new potential applications of NTA.

Note that the intensity-related measurement is performed inside a waveguide, which is faster than conventional image-based analysis due to the reduced FoV of the tracking area, and the microfluidic environment is also applicable for monitoring biological and chemical reactions in the nanoscale. Besides, waveguides carrying flat-field modes could provide a new platform for nanorheology, for example, to study complex fluid phenomena or inhomogeneous media. Fundamentals of light-matter interactions with nanoscale can also be investigated by using the light strand. One example is the measurement of photon pressure under constant illumination, which may be useful in the context of the Abraham-Minkowski controversy.

The general condition of the flat-field formation, $n_{\text{eff}} = n_1$, is derived, which can also be applied to other layer-structured waveguides in cases the guidance mechanism is based on total internal reflection, one example could be the nanoslot waveguide^{137,138}. The strong modal dispersions of leaky waveguides such as hollow-core systems may suggest that the flat-field condition could be also applicable, the examples include the optofluidic light cages¹¹⁵, microgap waveguides¹⁴⁶, ARROW¹⁴⁷, hollow-core¹⁰³ or

single-element anti-resonant-element fibers¹⁴⁸. Note that the guiding mechanism of NBF used in this work is fundamentally different from that of leaky waveguides, thus more studies are needed to explore the features of flat-field mode in the background of leaky waveguides, which is one of the directions of future works.

4.5 Materials and Methods

4.5.1 Nanoparticle Solution

Gold nanospheres with 50 nm mean diameter (ultrauniform, nanoComposix) were used for FaNTA experiments in this work. The nanosphere's aqueous suspension was mixed with DMSO with particular ratios of weights, allowing to roughly adjust the RI of the liquid. A more precise tune of the RI is conducted by temperature control using the Peltier element. The thermo-optic coefficient of the liquid as a function of mixing ratio was calculated using the equation described in Eq. 4.9, where the reference temperature $T_0 = 25^\circ\text{C}$ and the corresponding RI n_0 can be obtained by using the dispersion equation from interpolation of the measured data

$$n(\lambda, X) = \sqrt{1 + \frac{A(X)\lambda^2}{\lambda^2 - B^2(X)}}, \quad (4.10)$$

where λ is the wavelength and X is the ratio of water weight in the mixture (e.g., $X = 100\%$, pure water), and $A(X)$, $B(X)$ are expressed as polynomials

$$A(X) = \sum_{i=0}^3 C_i X^i; \quad B(X) = \sum_{i=0}^3 D_i X^i. \quad (4.11)$$

Values of the coefficients are shown in Table 4.3. For example, at room temperature

C_0	C_1	C_2	C_3
1.129563	-0.270527	-0.287922	0.181959
D_0	D_1	D_2	D_3
0.117524	-0.025920	0.017386	-0.008894

Table 4.3: The coefficients for the polynomial expressions defined in Eq. 4.11. The data were measured by Dr. Jiangbo (Tim) Zhao.

$T = 25^\circ\text{C}$ and $\lambda = 632$ nm, the RI of the solution ranges from 1.33 to 1.47 depending on the ratio of the mixture, which allows to have a RI for the flat-field condition. DMSO is used as a solvent because of its stable chemical properties and solubility of water. Our previous work using DMSO for the FaNTA experiment has been reported¹⁰² and the relevant physical and chemical properties can be found in the literature¹⁴⁹. For filling

the liquid into the nanochannel, the NBF is inserted in the prepared sample and the liquid will spontaneously flow into the nanochannel via capillary force.

In the FaNTA experiment, the modal intensity in the nanochannel is measured by detecting the elastic scattering light from the gold nanosphere. The scattering cross-section of the nanoparticle determines the scattered intensity and whether the nanoobject can be detected or not. Thus the scattering cross-section of the used gold nanosphere in pure water or DMSO/water mixture has been studied by using FEM simulations, the results are shown in Fig. 4.12. For example, in a 50 nm nanosphere in liquid of RI=1.461, the scattered cross section is about 2000 nm² at the wavelength of 532 nm, which is 2 times larger than the case of water (RI=1.33).

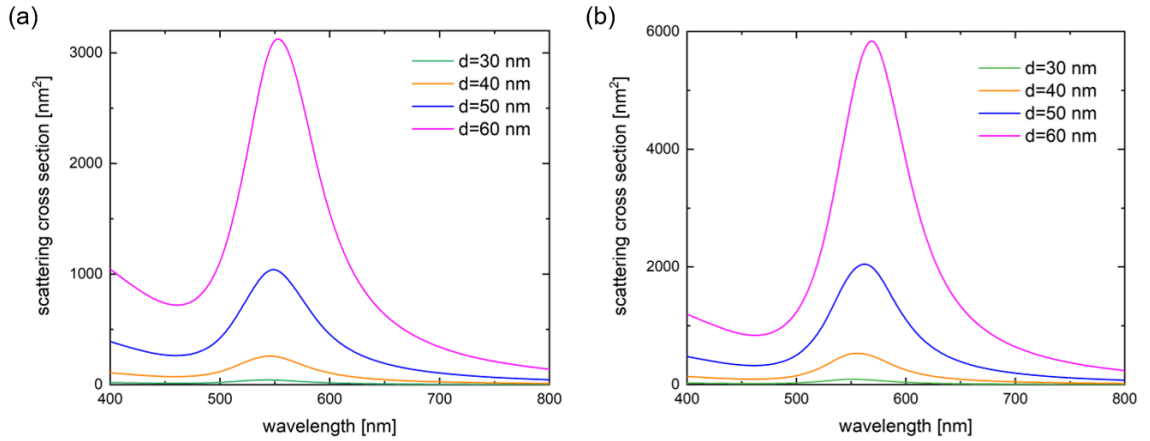


Figure 4.12: Simulated scattering cross-section of gold nanosphere as functions of the wavelength and diameters. (a) The nanoparticle in a liquid of RI=1.33. (b) The nanoparticle in a liquid of RI=1.461.

4.5.2 Optical Setup

Linear polarized laser (632 nm) is coupled into the liquid-filled NBF, and the fiber is kept straight to prevent mode distortions and polarization coupling effects. The Peltier element is placed above the optical fiber tracking area, in which the oil can eliminate the imaging aberration and act as a heat transfer medium. The RI of the liquid is finely tuned by controlling the temperatures. The optic-thermo coefficient of water/DMSO mixture is around $4 \times 10^{-4}/\text{K}$, which is higher than that of silica by two orders of magnitude. Thus the temperature-induced RI changes of the fiber materials are negligible.

In the FaNTA experiments, 20000 frames are recorded to sample the transversal intensity distribution of the channel, where the frame rate is $\nu = 3592$ Hz, duration is $\tau = 5.6$ s, and exposure time $t_e = 0.08$ ms. Due to the confinement of the nanochannel, the diffusion of nanoparticle is limited and extremely long trajectories can be recorded.

Within the 400 nm nanochannel, the nanoparticle can travel around the cross section more than 20 times in the recording duration, which guarantees high statistical accuracy of the intensity measurement.

Note that the relative standard deviation of the intensity variations around the flat-field condition is about 3.7% (shown in Figs. 4.11), arising from the modal distribution due to the RI mismatch and the systematic noise. Here we measured a static nanoparticle inside the channel to show the errors in the imaging process, and the results are shown in Fig. 4.13. The relative standard deviation of the measured scattered intensity is about 0.45%, which has a Gaussian distribution and is contributed by the inherent noise of the optical imaging system.

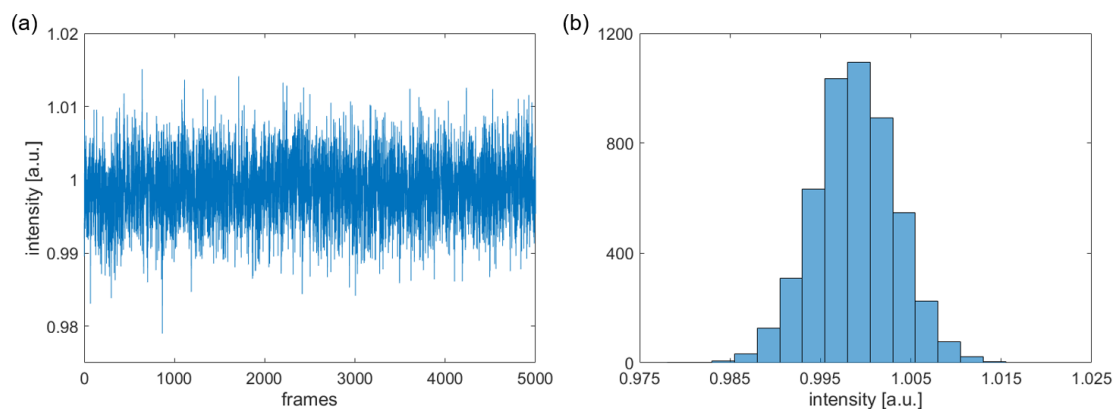


Figure 4.13: Intensity measurement of a static nanoparticle. (a) Scattered intensity as a function of the frame number. (b) Histogram of the intensities.

4.5.3 Data Analysis

The Python package *Trackpy* was used for the image processing of the recorded frames. The integration of the brightness within the pixels of the imaged nanoparticle refers to the scattered intensity, and the associated position (x and z) was determined by the centroid of the nanoparticle in each frame (taking the brightness-weighted average position of the pixels). Histograms and nonparametric kernel density estimation are then used to analyze the intensities in selected bins of the nanochannel's cross-section (defined as CB and SB in Fig. 4.8).

By comparing the relative shift of the peaks of CB and SB intensity histograms, δI_{\max} , we can judge the mode shapes in the nanochannel (shown in Fig. 4.11). For the case of $n_1 > n_{\text{eff}}$, the mode is Gaussian-like, meaning that the intensities around the central part are slightly higher than those around the edges, thus $\delta I_{\max} > 0$. For the complementary case, $n_1 < n_{\text{eff}}$, the mode is evanescent-like, as a consequence, $\delta I_{\max} < 0$. Thanks to the statistical analysis, the mode shape can be determined by

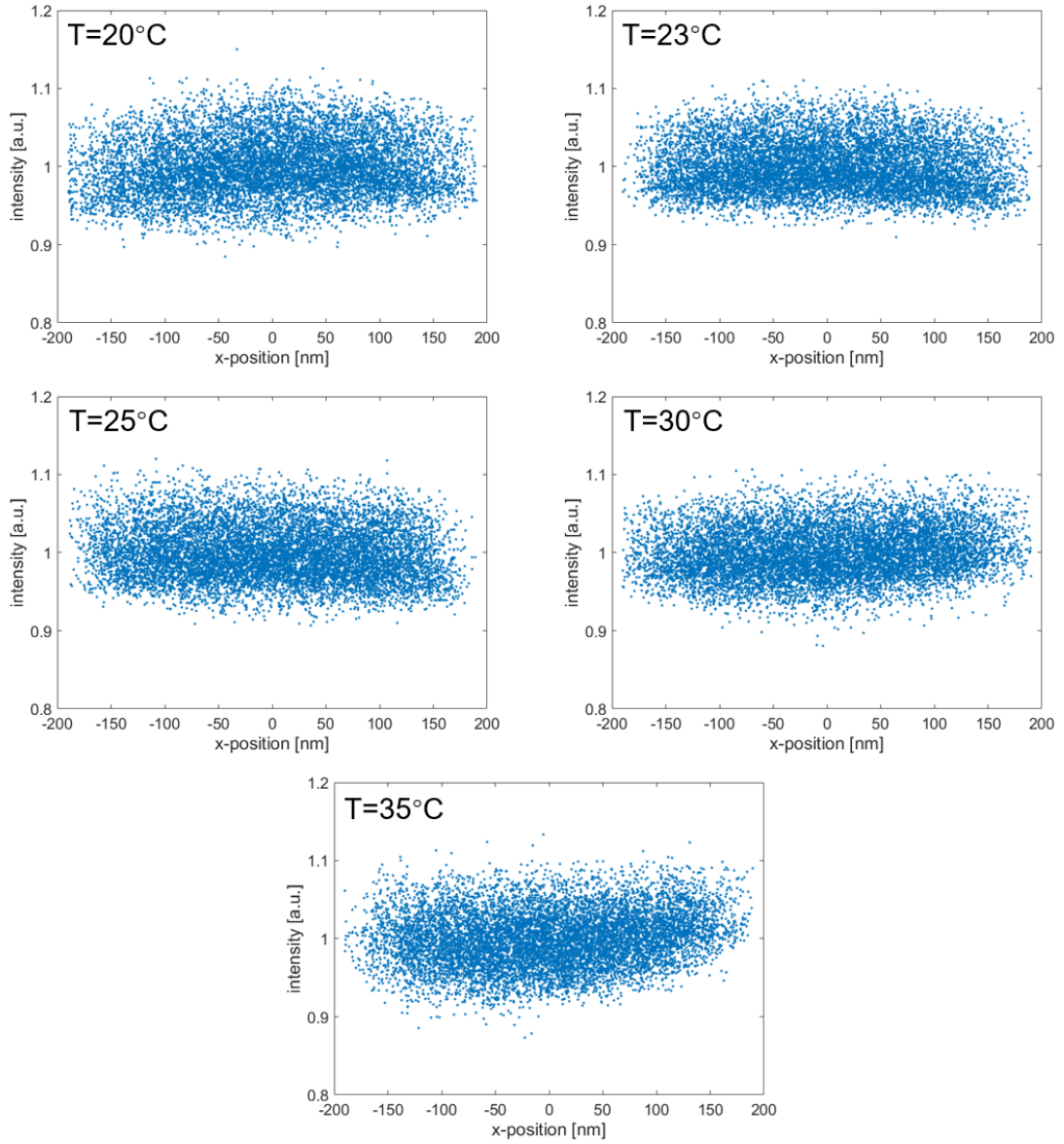


Figure 4.14: Scatter plots of the measured intensities corresponding to the transversal positions at temperatures 20, 23, 25, 30, and 35°C. The CB/SB histograms analysis are based on x -positions and the results are shown in Fig. 4.11.

comparing the peaks of the CB and SB histograms even though the mode distribution changes very slightly near the flat-field condition. The flattened mode is obtained when the peaks lie at the same intensity, that is, $\delta I_{\max} = 0$, which can be estimated by fitting the δI_{\max} as a function of temperatures.

The measured scattered intensities corresponding to the transversal (x) positions for different temperatures are depicted in Fig. 4.14. The scatter plots show a trend that as the temperature gets higher (RI of the liquid is lower), the intensities at the edge area of the nanochannel are slightly increasing. This is due to the mode transition

from Gaussian-like to evanescent-like, which is in agreement with the results of the histogram analysis shown in Fig. 4.11.

4.5.4 Random Walk Simulation in Circular Domain

The analysis of the modal distribution utilizes the Brownian motion of a single nanoparticle whose scattered signal is proportional to the local modal intensity in the nanochannel. To model this stochastic sampling process, a random walk simulation was performed in a circular domain. The generated positions (x and y) were combined with the calculated mode fields for simulating the randomly fluctuating scattered intensity caused by the Brownian motion. The simulations include the following steps:

1. 2-D random walk simulation of a 50 nm nanoparticle was carried out in a circular domain (diameter is 400 nm, frame rate is 3592 Hz) where reflecting boundary condition is used to model the wall of the nanochannel. The trajectory (x_i, y_i) is generated where the total number of steps is 2×10^4 .
2. The intensity distribution of the fundamental mode was calculated by using FEM modeling (Comsol Multiphysics 5.2). The RI of the liquid was calculated according to the temperature.
3. The intensity distribution inside the nanochannel was fitted by Gaussian function $I(x, y) = A \exp[(x^2 + y^2)/B] + C$, where A , B and C are fitting constants.
4. The local scattered intensities were obtained by using the generated positions in Step-1: $I(x_i, y_i) = A \exp[(x_i^2 + y_i^2)/B] + C$. Then the data is processed following the defined CB/SB histogram analysis.

An example of the simulated random walk trajectory (the first 1000 steps are shown) and the corresponding intensities are shown in Figs. 4.15. The use of the Gaussian function in Step 3 is justified since the modal field within the nanochannel is mathematically given by a modified or regular Bessel function, which can be well approximated by a Gaussian function in the case of small RI contrast between the core and nanochannel. Figs. 4.15 (b) and (c) depict the RI of liquid are 1.44 and 1.48, respectively. As expected, the evanescent mode (the side region has a larger modal intensity) shows an up-curved intensity distribution and the peak intensity of SB is larger than that of the CB; whereas, the Gaussian mode shows the opposite tendency.

The simulation is also applied for the temperature scans, where the related liquid RIs are calculated using Eq. 4.9. Fig. 4.16 shows the simulated scattered intensity corresponding to the x -position. It is observable that the intensities at the edge area of the nanochannel are slightly increased as the temperature gets higher. It indicates that the mode transit from Gaussian to evanescent, which is in agreement with the measured

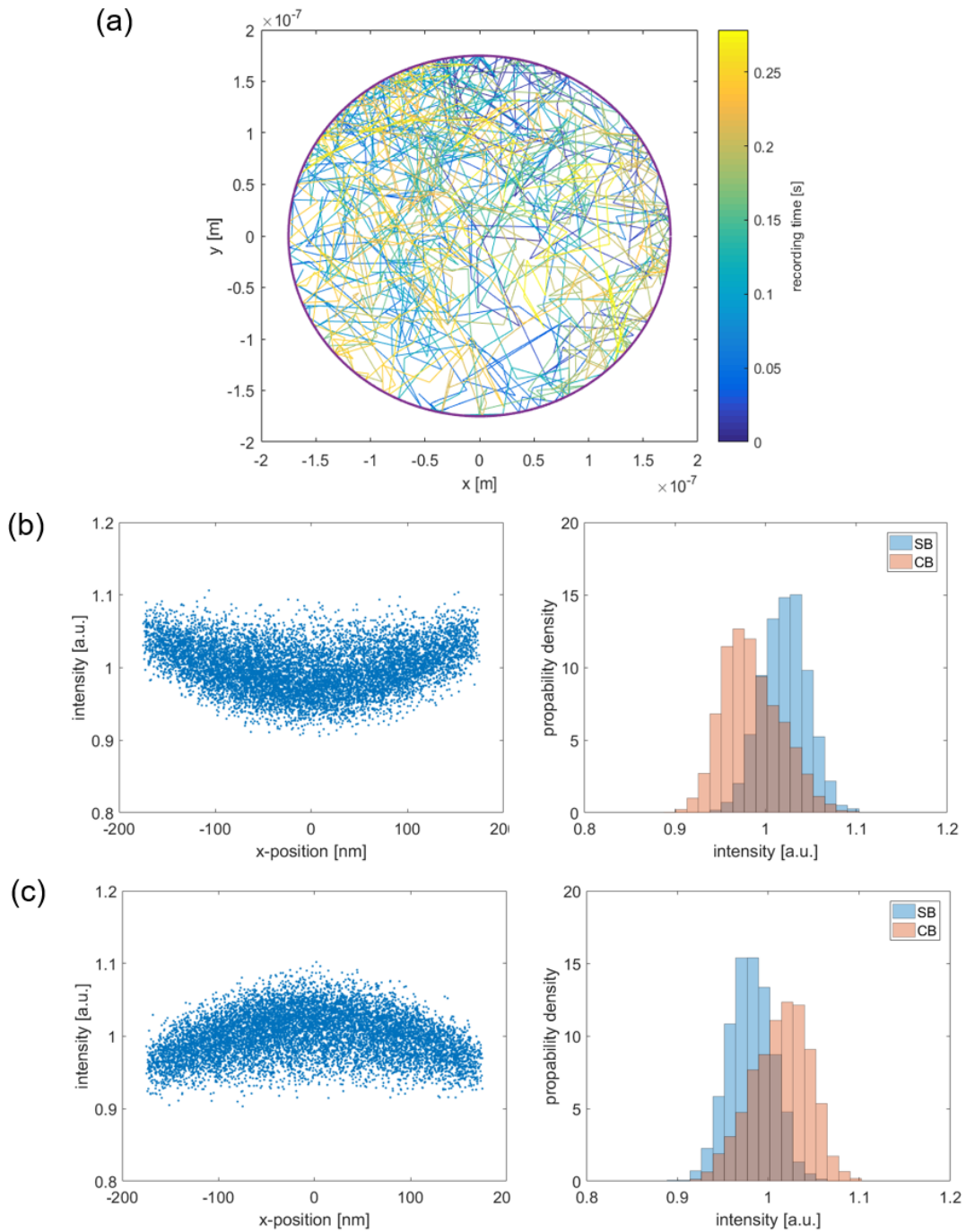


Figure 4.15: Simulation of the random walk and the sampled intensities. (a) Trajectory (1000 steps shown) of a 50 nm nanosphere within the nanochannel (the diameter is 400 nm). Intensities corresponding to the x -positions, and the histograms of the CB/SB, where the RI of liquids is (b) 1.44 (evanescent mode) or (c) 1.48 (Gaussian mode), respectively.

results shown in Fig. 4.14. The simulated CB/SB histograms corresponding to the temperatures are depicted in Fig. 4.17, and compared with the experimental results (Fig. 4.11), the results exhibit a high similarity, from which the simulated flat-field

condition occurs at 30.45 °C and the measured one is 28.5 °C. Thanks to the FaNTA which provides a long trajectory of the nanoparticle, it ensures sufficient accuracy in the statistical analysis. Even if the mode intensity changes very slightly around the flat-field condition, we can still judge the mode types through the peak positions of the histograms.

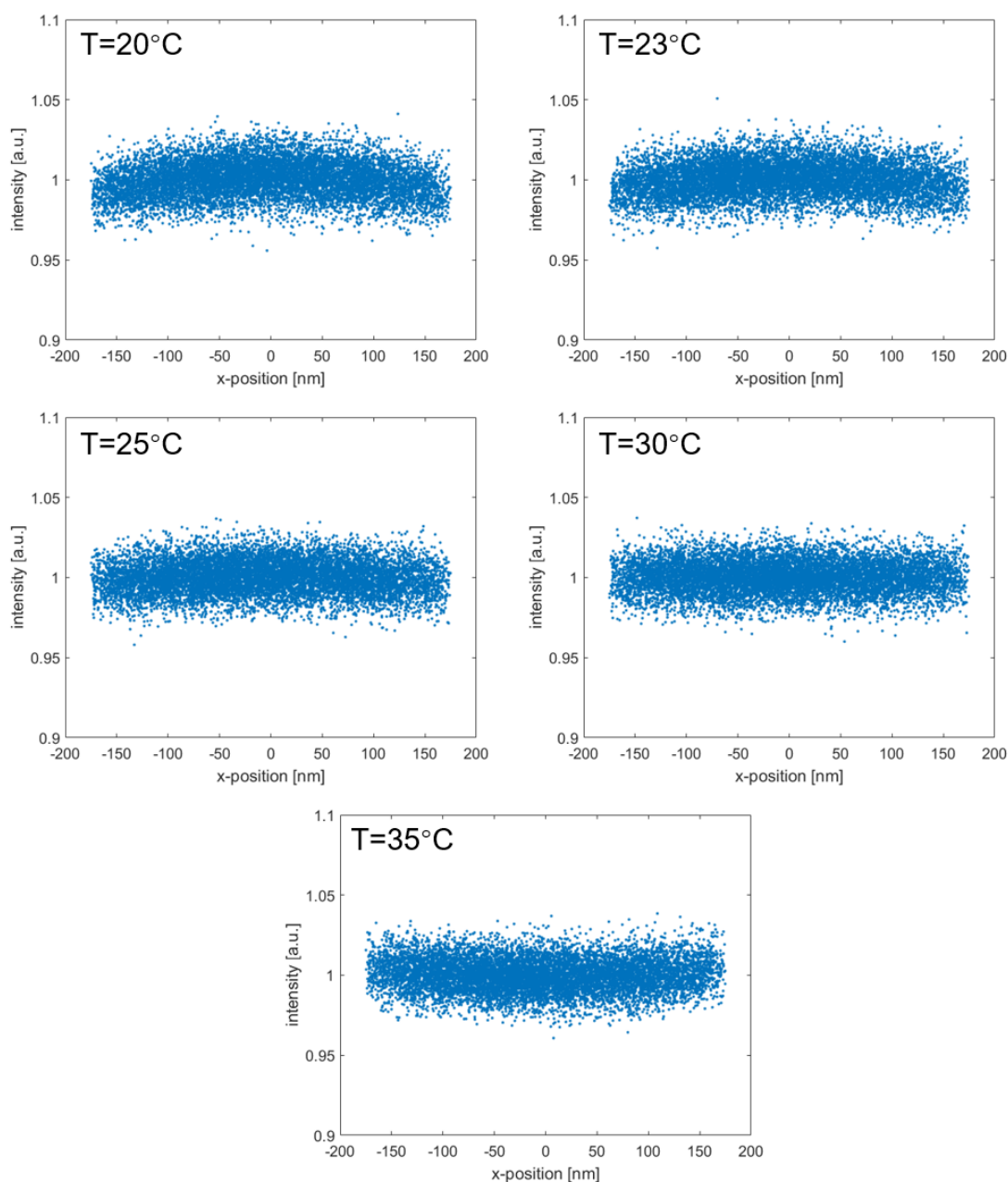


Figure 4.16: Scatter plots of the simulated intensities corresponding to the transversal positions at temperatures 20, 23, 25, 30, and 35°C.

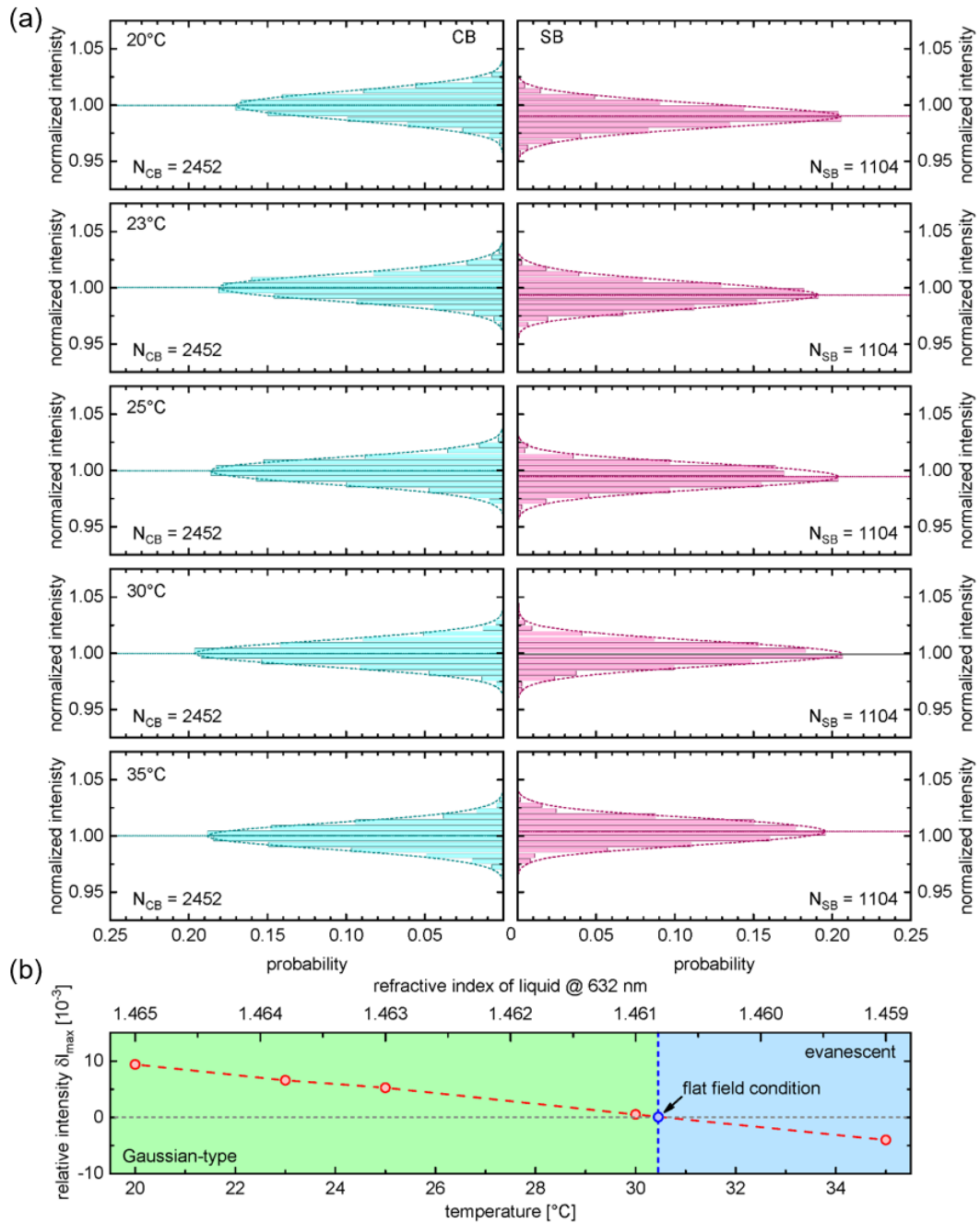


Figure 4.17: Simulation of the FaNTA experiments with the RI of liquid (9 wt. % water and 91 wt. % DMSO mixture) tuned by temperature scan to determine the flat-field conditions. (a) Histograms of the CB and SB with temperature of 20, 23, 25, 30, 35 °C. The number of intensity points used in each histogram is noted as N_{CB} or N_{SB} . The dotted horizontal lines indicate the positions of the histogram peaks I_{\max}^{bin} . (b) The relative shifts of the peaks $\delta I_{\max} = (I_{\max}^{\text{CB}} - I_{\max}^{\text{SB}})/I_{\max}^{\text{CB}}$ as a function of temperatures (bottom axis) and RI of the liquid (top axis). The temperature at which the flat field condition occurs is determined by the linear interpolation of the two points beside. The colored backgrounds refer to the types of the mode near the flat field condition (light green: Gaussian-type, light blue: evanescent-type).

4.6 Chapter Summary

This work presents for the first time the realization of an optical field with constant intensity along all three spatial directions (including the propagation direction), the so-called light strand, based on optofluidic nanostructured fiber. The essential feature of this approach is the integration of externally accessible nanochannel in the core of the step-index optical fiber, which enables the studies of light-matter interactions in nanoscale fluidic environments. This optical mode is generated by filling the nanochannel with RI-matched liquid and the RI is finely tuned through temperatures, which makes it satisfy the flat-field condition, resulting in an optical field intensity that exhibits no transversal or longitudinal intensity variation within the fluidic nanochannel. The analytical model reveals the generally valid condition for obtaining flat fields and modal dispersion properties, which can be appropriately extended to other types of waveguides.

Furthermore, the light strand was verified by performing FaNTA experiments, where a 50 nm gold nanosphere was used as a Brownian nanoprobe to sample the spatial intensity distribution inside the flat mode domain. The statistical method is designed to analyze the measured intensity data and the results clearly show evidence of the homogeneous intensity profile. Regarding the feature of waveguide mode, the longitudinal range of the light strand can be further prolonged to arbitrary length, which is principally challenging in free space optics due to the inherent diffracting nature of light. The flat-field condition is not limited to the regimes discussed in this work and could be extended to other waveguide systems, such as nanoslot waveguides, on-chip hollow-core waveguides, and antiresonant fibers, however, due to the specificities of the waveguide structures, more detailed studies are needed to uncover the mode properties.

In outlook, the concept of light strand provides a new platform applicable for many research fields, including life sciences (e.g., characterization of nanoobjects such as viruses and biomacromolecules and analysis of chemical or biological reactions), fluids dynamics (e.g., studies of softer matters or rheology in nanoscale), fundamentals of light-matter interactions (e.g., measurements of light scattering and photon pressure on nanoobjects), and optical sensing (e.g., measurements of RI, temperatures and viscosity of liquids).

5 | NTA in Fiber-assisted Optofluidic Device with Flattened Illumination

Thanks to the spatial restriction of nanoobjects by microfluidic channel and simultaneously the guided mode in microstructured optical fiber, the FaNTA platform can achieve ultralong and label-free tracking of the Brownian motions of a single nanoparticle. The previous chapter demonstrated the formation of a flattened light field in the fluidic nanochannel—light strand— could effectively increase the focal depth of the tracking measurement. However, regarding the used NBF, the volume of the specimen has been limited by the dimensions of the nanobore and optical core of the fiber. Thus, to detect and identify nanoparticles in extended space, a concept of a fiber-assisted optofluidic chip with flattened illumination is proposed in this work. It experimentally demonstrates that the device can work for a long nanoparticle tracking without spatial dependence of light field, in particular, a large fluidic channel (diameter is 4 μ m) is available, which may provide a new platform applying for the studies of nanomaterials and microfluidic technologies.

This chapter is based on the publication by Gui et al.¹⁵⁰, reproduced with a CC-BY license, published by De Gruyter.

5.1 Introduction

The development of microfluidic platforms has attracted great research interests and widely employed in many fields, such as biosensors^{151–154}, living cell analysis^{155–159}, nanomaterials characterization^{160,161} and nanomedicine^{162,163}. In recent years, one of the key directions is the detection of nanoparticles based on optofluidic devices, aiming to have high sensitivity, selectivity and high system integration, which is becoming an important experimental approach used in advanced biochemical sensing^{164–166}.

It has been demonstrated that the waveguide-based optofluidic system, such as the FaNTA using NBF as presented in the previous chapters, is an emerging scheme applied in NTA experiments. However, a common issue that may limit the use of waveguides in NTA is that the guided modal fields are spatially dependent, according to the guidance mechanisms. Although the flattened mode is developed in the NBF, the transversal dimension is nanoscale (400 nm). Furthermore, simulations show that as the channel size increases, more precise control (liquid RI or temperature) is required to obtain the flat-field condition. This fact may limit the applications of the light strand due to the restricted volume and accessibility of the specimens.

There is an increasing demand for integrated optofluidic sensing chips, e.g., spectroscopy measurements based on 3-D nanoprinted waveguide¹⁶⁷, on-chip molecular biosensor¹⁶⁸, single particle traps and fluorescence detection using optofluidic chip¹⁶⁹ and on-chip fluorescence optofluidic microscope¹⁷⁰. In this context, a fiber-integrated optofluidic chip is proposed and employs a capillary fiber with a larger fluidic channel (the diameter is 4 μm) for containing the analytes, and a single-mode launching fiber for straightforward illumination on the observing region. Note that the RI of the liquid needs to be consistent with that of the silica capillary ($n_c=1.4607$), which is by using a DMSO aqueous solution. As a result, the illuminating beam can propagate in a homogeneous medium and there is no guiding mode formation in the capillary fiber, which is the key aspect of the working principle for this device. This solution can not only achieve the constant illumination of nanoobjects but also shows two advantages compared to the light strand concept: i) it offers the specimens a larger volume capacity for light-matter interactions; ii) the optofluidic system has a higher on-chip integration degree, which provides more capacity and efficiency in understanding biochemical processes.

In this work, the proposed concept was experimentally verified by implementing NTA measurement, where a single 50 nm gold nanosphere was tested and the length of the obtained trajectory is 65000 frames with a total duration of 60 seconds. The light field distribution in the microchannel was analyzed by using statistical histograms, defined by the center and side regions according to the x -positions (see section 4.3.3), of the scattered intensity. The overlapping histograms indicate that the illumination in the microchannel is flattened. Therefore, these results confirm that the proposed optofluidic chip can achieve a uniform light field within the observation area and has the ability to track single nanoparticles with a large number of frames, demonstrating the potential of this technology applied in fundamental studies of life science and light-matter interaction.

5.2 Working Principle

The concept of fiber-assisted optofluidic chip for NTA measurement is illustrated in Fig. 5.1 (a). The experimental setup consists of a launching optical fiber and a capillary fiber which are aligned on a silica v-groove and exposed to the liquid environment of interest. The nanoparticles to be measured are filled in the capillary and the transversal diffusing motions are limited by the walls of the microchannel so that the nanoparticles will stay in the depth of focus for a long observation time. The lateral scattered light is collected via a standard optical microscope above the capillary fiber and imaged on a CMOS camera.

The crucial part of this approach is the special type of illumination provided for the tracking area. Here, the beam emitted from the launching fiber can be approximated as a Gaussian beam¹⁷¹. During the propagation, the diameter of the beam continues to expand, and when it reaches the observation area, the beam width will exceed the actual diameter of the microchannel. By properly adjusting the distance between the two fibers, the intensity distribution of the beam across the microchannel is almost uniform (the difference in light intensity between the center and edge of the channel is less than 1%, as shown in the inset of Fig. 5.1 (a)).

5.2.1 Illumination with Gaussian Beam

The top view of the chip with detailed parameters is shown in Fig. 5.1 (b). The intensity profile of the launching beam can be described as a Gaussian function,

$$I(r, z) = I_0 \left[\frac{\omega_0}{\omega(z)} \right]^2 \exp\left[-\frac{2r^2}{\omega^2(z)}\right], \quad (5.1)$$

where $\omega(z) = \omega_0 \sqrt{1 + (z/z_R)^2}$ is the beam radius as function of the propagating distance z , $z_R = \pi\omega_0^2 n/\lambda$ is the Rayleigh range, ω_0 is the beam waist, λ is the wavelength and n is the RI of the medium.

Using Eq. 5.1 and the experimental parameters that the diameter of the microchannel is 4 μm , $\lambda = 0.532 \mu\text{m}$, and $\omega_0 = 4.2 \mu\text{m}$, the light intensity at the liquid-solid interface ($r = 2 \mu\text{m}$, denoted as I_1) and that at the center of the microchannel ($r = 0 \mu\text{m}$, denoted as I_2) are calculated. The arrangement and coordinate system of the calculations are presented in Fig. 5.2 (a). The ratio I_1/I_2 as a function of the propagation distance z is shown in Fig. 5.2 (b). It indicates that the intensity difference along the transversal direction of the microchannel is about 1% when $z = 1 \text{ mm}$. The longitudinal intensity of the beam is reduced by 17% starting from $z = 1 \text{ mm}$ (the entrance of the capillary fiber) to $z = 1.1 \text{ mm}$, as shown in Fig. 5.2 (c).

Consider a single nanoparticle, e.g., the 50 nm gold nanosphere used in the experiment has a diffusing length of $L_{\text{dif}} = \sqrt{2D\tau} = 17 \mu\text{m}$, where $D = 2.23 \mu\text{m}^2/\text{s}$ (the measured diffusion constant) and $\tau = 65 \text{ s}$ (the observation time) are used for calculation. Thus, taking into account the dependence of the longitudinal intensity (decreasing 17% in 100 μm), the relative fluctuation of the scattered intensity of a single nanoparticle during the tracking can be estimated by $\delta I = 17\% \times 17\% = 2.9\%$, which indicates that the illumination has a good flatness for the NTA measurement. Note that the distance between the launching fiber and the capillary fiber can be further enlarged to reduce the intensity variation of the beam in all three dimensions.

The calculation is based on the ideally homogeneous medium where none of any leaky modes exist. Once the RI of the liquid is inconsistent with that of the silica cladding,

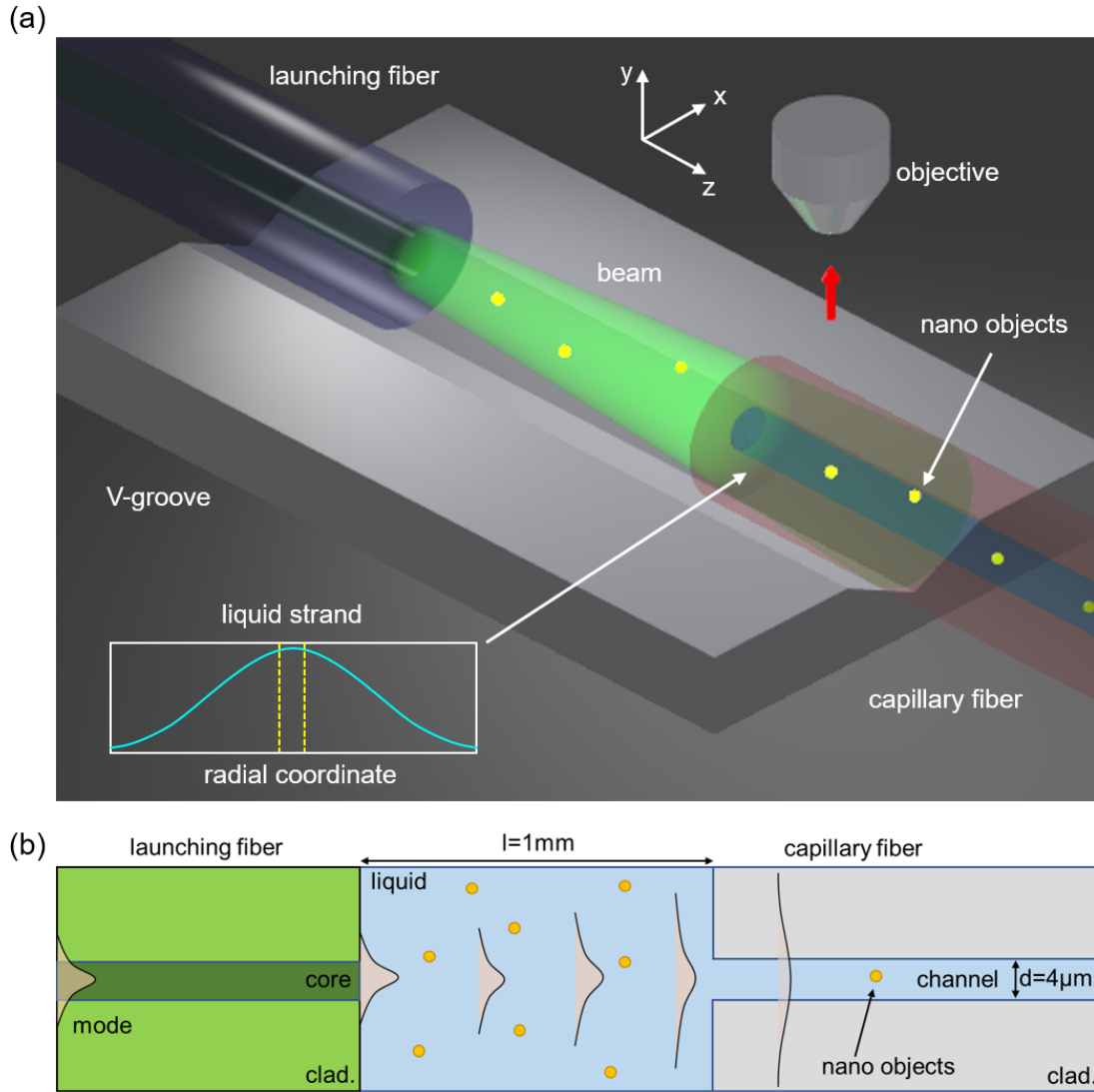


Figure 5.1: The concept of the fiber-assisted optofluidic device for NTA experiment under flattened illumination. (a) The concept of the nanoparticle tracking analysis using capillary fiber, where the launching and capillary fibers are placed on a silica V-shaped groove for alignment of the optical axis. The blue area refers to the fluidic channel with golden nanoparticles filled by water-DMSO mixture of which the refractive index is consistent with the cladding of the capillary. The insert shows the light intensity in the liquid strand with an almost flat field (the difference between center and edge is less than 1%). (b) The top view of the device and the corresponding parameters of the system.

leaky modes can emerge in the capillary fiber, depending on the RI contrast of the medium, which needs to be avoided in the NTA experiment. Numerical simulations are performed to study the mode properties in the presence of RI-mismatch.

5.2.2 Numerical Simulations

The key point of the working principle is the use of DMSO aqueous solution of which the RI (noted as n) needs to match the RI of the silica capillary fiber (n_c) to avoid

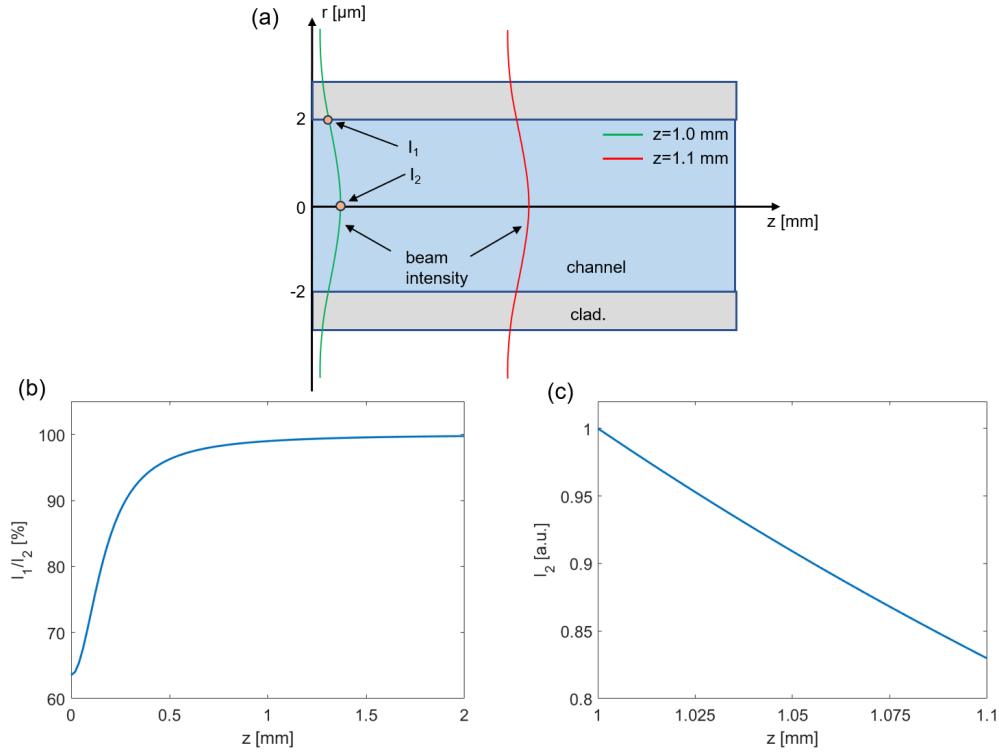


Figure 5.2: Intensity calculation of the launching beam using the experimental parameters $\lambda = 0.532 \mu\text{m}$, $\omega_0 = 4.2 \mu\text{m}$ and $n = 1.4607$. (a) The arrangement and coordinate system in the calculation. (b) The ratio of the beam intensities at the wall-liquid interface, I_1 ($r = 2 \mu\text{m}$), and the center, I_2 ($r = 0 \mu\text{m}$), of the microchannel as a function of the propagation distance z . (c) The longitudinal intensity of the beam (I_2) in the range from $z = 1 \text{ mm}$ to $z = 1.1 \text{ mm}$.

leaky mode formation in the capillary fiber. However, in practice, there is always an RI mismatch in the prepared liquids. Therefore, to investigate the mode behaviors in the presence of RI differences between the liquid and silica capillary fiber, numerical simulations are performed using FEM software COMSOL Multiphysics 5.2.

In the simulation, the frequency domain solver with a 2-D axisymmetric model is applied to compute the modal field distribution in the capillary fiber. The outer space is surrounded by perfectly matched layers (PML) to simulate the infinite domain. Without loss of generality, a plane wave is set as the excitation field in the simulation domain and the scattered field is computed in the existence of the fluidic microchannel. The working wavelength is 532 nm and the RI of silica $n_c = 1.4607$ with a capillary hole diameter of $4 \mu\text{m}$. Note that the liquid domain extends a distance of $1 \mu\text{m}$ outside the capillary as the launching area of the beam so that the excitation plane wave in the simulation can be written as piecewise expressions by using the Fresnel equation: (i) liquid part: $E_1 = E_0 \exp(-ik_1 z) + r_0 E_0 \exp(ik_1 z)$; (ii) capillary part: $E_2 = t_0 E_0 \exp(ik_2 z)$, where $r_0 = (n - n_c)/(n + n_c)$ is the reflection coefficient and $t_0 = 2n/(n + n_c)$ is the transmission coefficient at the liquid-silica interface. E_0 is the amplitude of the plane

wave, $k_1 = 2\pi n/\lambda$ and $k_2 = 2\pi n_c/\lambda$ are the wave numbers in the liquid and capillary fiber, respectively. The simulation model is depicted in Fig. 5.3 (a).

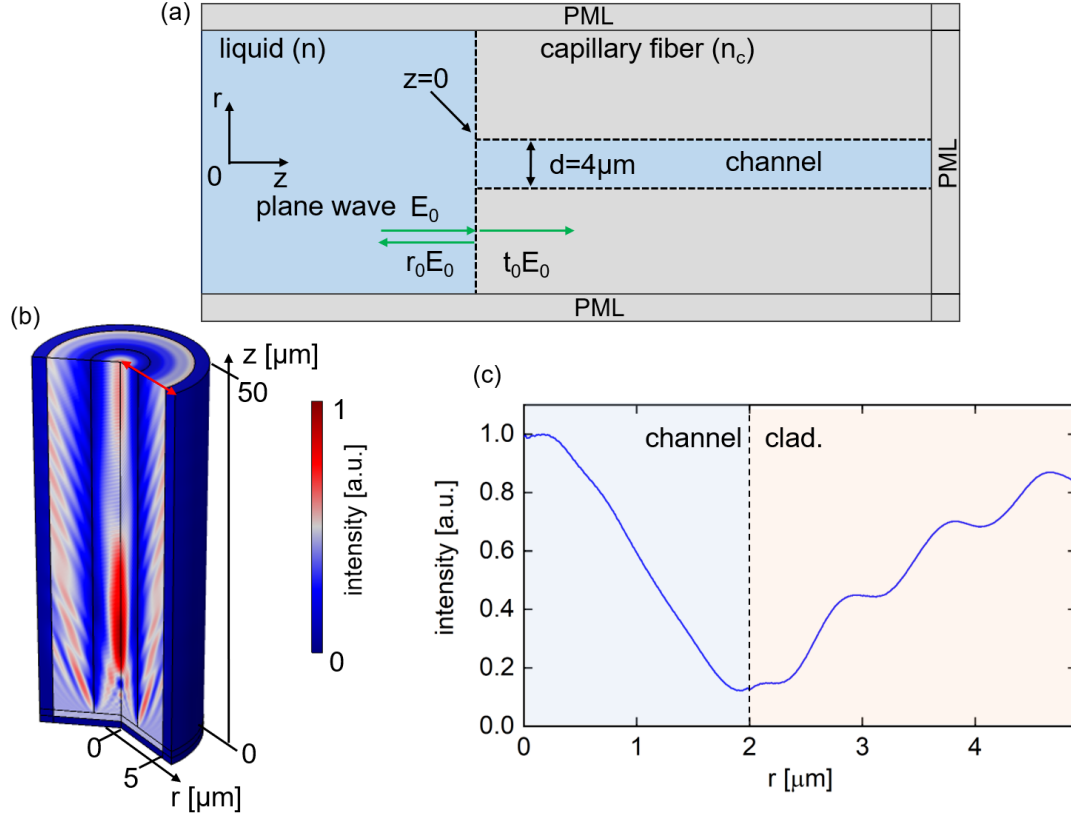


Figure 5.3: Simulations of the intensity distributions of electric fields in the capillary fiber filled with water that $n = 1.33$. (a) Sketch of the simulation domain, where the excitation fields are plane waves, and the scattered fields from the liquid channel are simulated. The length of the liquid part is set as $1 \mu\text{m}$ in the simulation. (b) A 3-D view of the modal distribution in the water-filled capillary. The red arrow indicates the position of $z=50 \mu\text{m}$. (c) Line plot of the radial modal intensity measured along the red arrow denoted in (b).

It is worth noting that the NTA experiment is conducted in the input area of the capillary fiber ($\Delta z < 200 \mu\text{m}$) taking into account two factors: (i) to avoid multi-reflection from the outer interface of the capillary fiber; (ii) to provide enough illuminating intensity for the detection of scattered light (central intensity of the beam reduces to 1.2% after a propagation distance of 1 mm). The longitudinal dimension of the simulation domain is $50 \mu\text{m}$ starting from the entrance of the microchannel. Firstly, the 3-D view of the field distributions for the case of the water-filled capillary is computed and shown in Fig. 5.3 (b), and the corresponding line plot of the radial profile is shown in Fig. 5.3 (c), which is measured at the position of $50 \mu\text{m}$ inside the microchannel.

It clarifies that leaky modes occur in this case since the total internal reflection fails due to the low RI of the water channel. There are complex field distributions in the

channel and cladding, showing both horizontal and longitudinal dependencies, which are not suitable for NTA experiments since the scattered intensity will change rapidly with the diffusing motions of the nanoparticle. For example, the light intensity at the edge of the microchannel has dropped by 90% compared to the center. As a result, the received scattered signal of the nanoparticle will be blinking as the diffusing motions, and the trajectory interrupts at the positions where the intensity is too low. This will significantly deteriorate the accuracy of the NTA measurement.

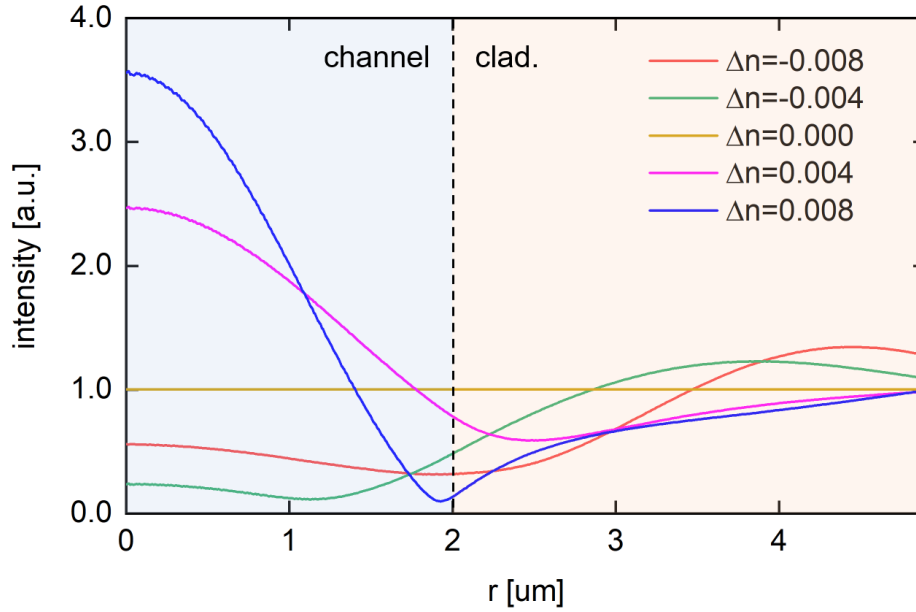


Figure 5.4: Simulations of the intensity distributions of electric fields in the capillary fiber filled with RI-mismatches, ranging from -0.008 to 0.008. The line plots are measured at the position of 50 μm inside the microchannel.

Next, the cases of relatively small RI-mismatch that could happen in practical applications are studied and the results of radial profile (measured at the position of 50 μm inside the microchannel) are shown in Fig. 5.4. The RI-mismatch is denoted as Δn and the RI of the liquid is denoted as $n = n_c + \Delta n$. The results indicate that when $\Delta n > 0$, the total internal reflection is valid and the capillary acts as a step-index optical fiber, most of the light fields are confined in the high-RI channel, forming a waveguide mode. On the contrary, once the $\Delta n < 0$, the leaky modes emerge in the cladding, and as the RI difference decreases, the amplitude of the leaky mode is further increasing. In the case of $\Delta n = 0.002$, the capillary fiber works as a weakly-guide optical fiber and the core mode is approximately Gaussian, where the modal intensity drops by 40% from the center to the channel's wall.

As a representative, the 3-D viewed distributions of electric field intensity with the RI-mismatches $\Delta n = -0.004$, 0.004, and 0.000 are shown in Figs. 5.5 (a), (b), and (c), respectively. The radial modal distributions measured at the distance of 50 μm inside

the microchannel are shown as the line plots in Fig. 5.5 (d). The results indicate that when the $\Delta n = 0.004$, a guided mode will be excited in the microchannel and the modal intensity of the center is about 3 times larger than that of the liquid-wall interface. Whereas, when $\Delta n = -0.004$, the leaky mode occurs, and within the microchannel, the central light field is about half of the lateral field intensity.

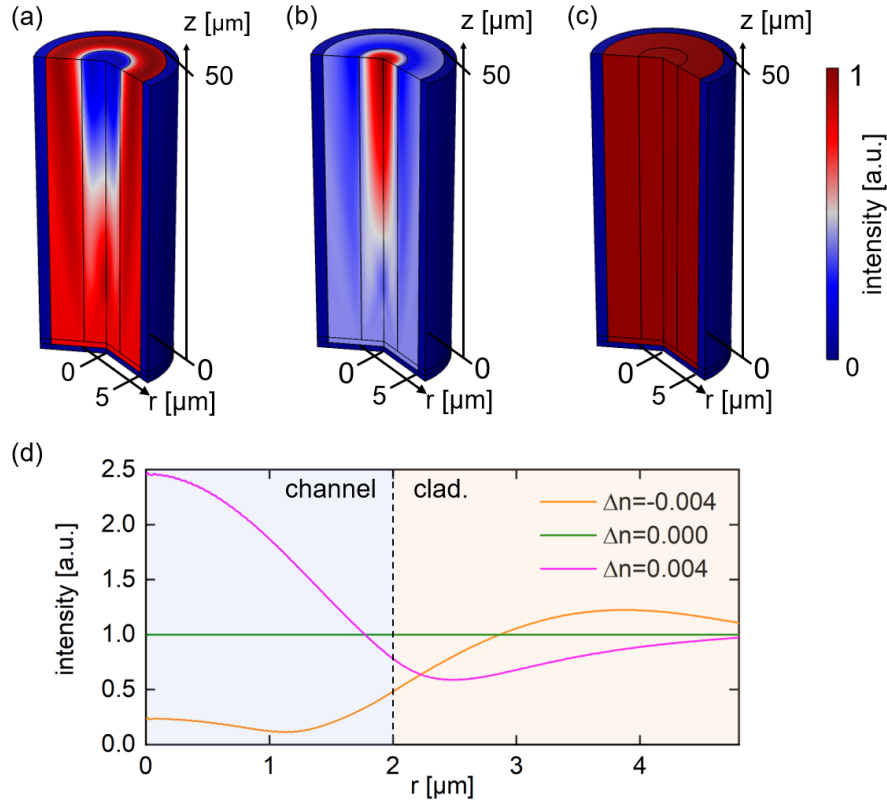


Figure 5.5: Simulations of the intensity distributions of electric fields in the capillary fiber with RI-mismatches of the liquid Δn . (a) $\Delta n = -0.004$. (b) $\Delta n = 0.004$. (c) $\Delta n = 0.000$. (d) Line plots of the radial modal intensity measured at the position of $z = 50 \mu\text{m}$.

5.2.3 Experimental Setup

We performed an NTA experiment to demonstrate the fiber-integrated optofluidic device with flattened illumination. The experimental setup is shown in Fig. 5.6. Here, the launching fiber and capillary fiber (channel diameter is $4 \mu\text{m}$) were aligned on a silica V-groove chip, where the launching fiber was fixed on the chip by using UV curing epoxy (Vitalit [®]1605) and maintained a distance of approximately 1 mm from the capillary fiber. To eliminate any potential bubble issues, plasma treatment with 100 W for 1 minute was performed before the tracking experiments.

In the experimental setup, the laser light (Coherent Verdi G, $\lambda=532$ nm) was delivered by a single-mode fiber (Thorlabs, S405-XP), which was then spliced with the polarization controlling loops (polarized along the x-direction) that were made by a low NA fiber (NA=0.05). The light was fiber-to-fiber coupled into the launching fiber (NA=0.05 and core diameter is about 7 μm), which is operating in single mode. The suspended solution of 50 nm gold nanospheres (nanoComposix, ultrauniform) was mixed with DMSO (the volume of water in the mixture is 18.2%). Then the liquid sample was loaded on the chip and a glass coverslip was covered above to improve the imaging quality. The nanoparticles were imaged using a 10x objective (Olympus Plan Achromat, NA=0.25, depth of field $d_z = 10$ μm) and recorded by a CMOS camera (Basler acA4096-40 μm) where the FoV of the captured frame is 30×600 pixels², and the used frame rate and exposure time were 1000 Hz and 0.2 ms, respectively.

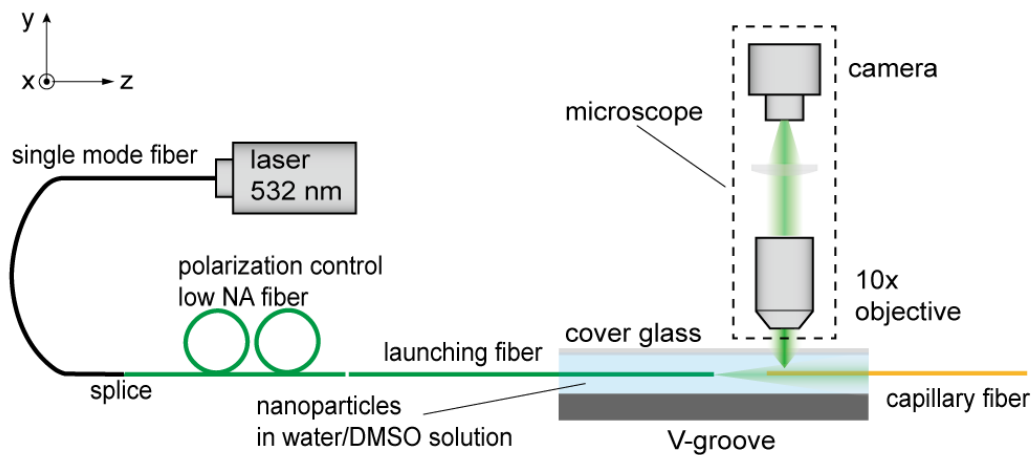


Figure 5.6: Experimental setup of the fiber-assisted optofluidic device with flattened illumination from a divergent Gaussian beam. The chip is placed under a standard optical microscope for the tracking measurements. 532 nm laser is delivered through a single-mode fiber with polarization control loops and fiber-to-fiber coupled into the launching fiber. The liquid is loaded directly on the chip and filled into the microchannel via capillary force, and the capillary is sealed by glycerin after the filling is done. A glass coverslip is used to enhance the imaging quality.

5.3 Results

The designed optofluidic chip was tested by carrying out an NTA experiment and directly exposed to the liquid sample of interest. The light beam emitted from the launching fiber propagates about 1 mm and then reaches the end face of the capillary fiber. Within the envelope of the illuminating beam, diffusing nanoparticles (the concentration is 8×10^8 particles/ml) can be observed in the free space. The region of the NTA experiment was selected in the entrance part of the microchannel, where the nanoparticles were transversely confined to obtain a long trajectory. The microscopic

image of the working area of the device is shown in Figs. 5.7 (a) and (b). A representative image of the tracked nanosphere is shown in Fig. 5.7(c) using a logarithmic scale and the Airy pattern indicates that the imaging system is diffraction-limited.

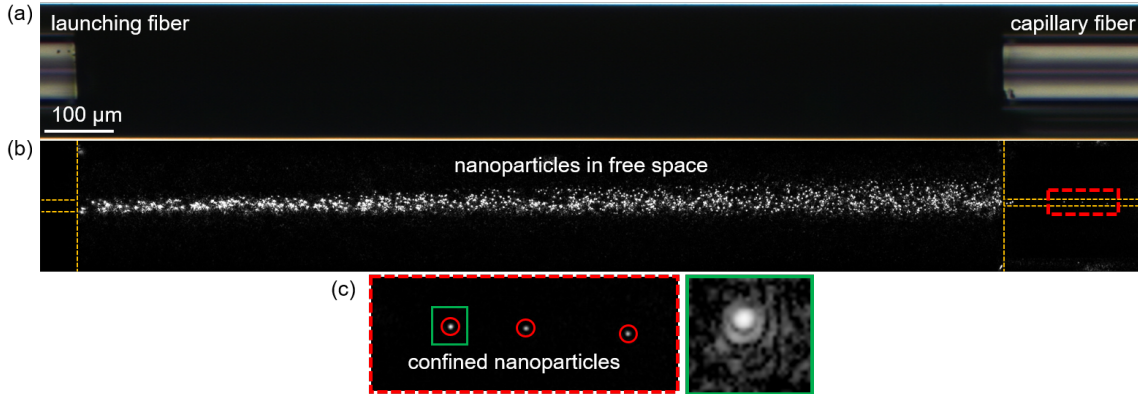


Figure 5.7: Representative images of the fiber-assisted optofluidic device and its working status for NTA experiments. (a) Microscopic image of the device before filling liquid. The distance between the launching and capillary is around 1 mm. (b) The working device after loading the liquid sample. (c) Enlarged views of the nanoparticles in the fluidic microchannel of the capillary. The nanoparticle framed by the green box is displayed in the logarithmic scale.

5.3.1 Scattered Intensity Measurement

Due to the confinement of the microchannel, nanoparticles can stay in the FoV with a long observation time to guarantee the statistical significance of the measurement. More importantly, the loading liquid has the same RI as the capillary fiber so that there is no guiding mode formation in the microchannel, leading to a free propagation of the illuminating beam. As calculated in Fig. 5.2, within the channel, the transversal intensity difference of the beam between the center and wall is less than 1%, which can effectively increase the depth of focus for the tracking experiment. Besides, the fluctuations of the longitudinal intensity of the beam can be ignored within the observing duration (60 s) due to the short diffusing length of the nanoparticle (17 μm). The measured time-dependent scattered intensities of a single nanoparticle diffusing in the microchannel are shown in Fig. 5.8.

A trajectory of a 50 nm single nanosphere has been obtained with 65,000 frames recorded and the total observing duration is 65 seconds, shown in Fig. 5.8 (a). The time-dependent scattered intensities have a Gaussian distribution, shown in Fig. 5.8 (b), from which the relative standard deviation is $\delta I = \sigma I / \bar{I} = 5.7\%$, which is consistent with the estimation in section 5.2, demonstrating the benefit of the flattened illumination that can improve the capability of the fiber-assisted optofluidic device in ultralong tracking of single nanoparticles. Note that the variation of both the transversal and longitudinal

intensity is negligible in the time window of the recording (typically 65 s and diffusing length is 10 μm), which is shown in Figs. 5.8 (c) and (d).

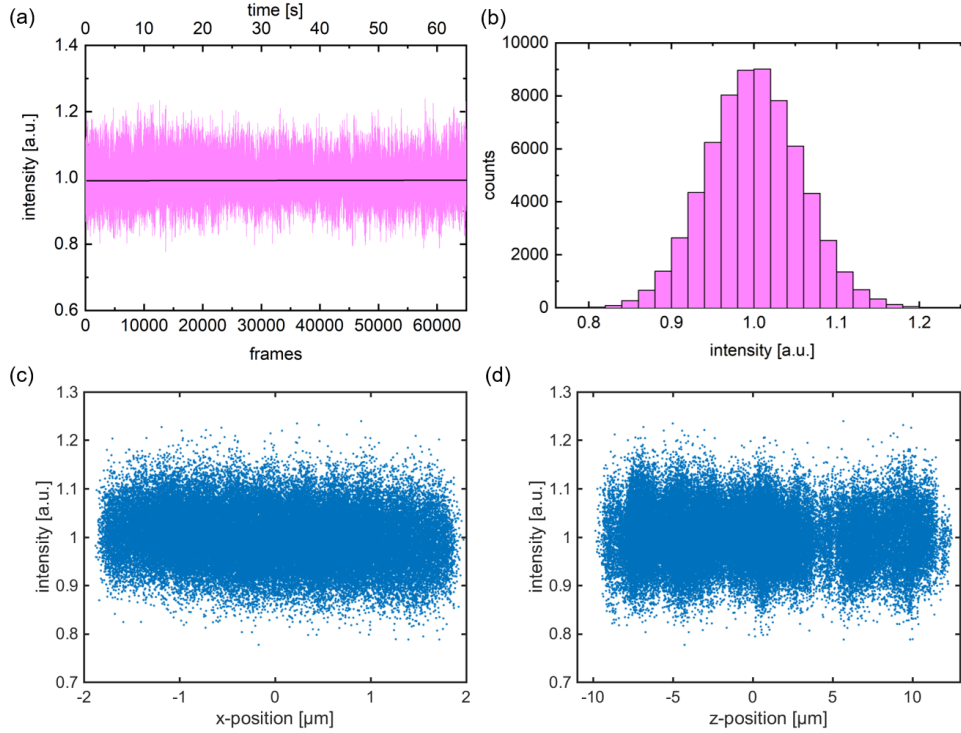


Figure 5.8: Results of the scattered intensity of a single nanosphere with the flattened illumination. (a) Scattered intensity (normalized by the averaged value) as a function of the recorded frames (bottom axis) and time (top axis). Here, the obtained trajectory length is 65000 frames with a total observation time of 65 seconds. (b) Statistical histogram of the intensity, showing a well Gaussian distribution with a relative standard deviation of 5.7%. (c) Scattered intensity as a function of x -positions, which shows a flat distribution along the transversal direction of the microchannel. (d) Scattered intensity as a function of z -positions, which shows a diffusing length of 20 μm in the longitudinal direction.

To further analyze the light field distribution in the transversal direction of the microchannel, similar to the method used in section 4.3.3, the cross-section was divided into the center bin (CB) and side bin (SB) according to the x -positions of the nanosphere, as shown in Fig. 5.9 (a). The data points of the scattered intensity located in the defined bins were extracted and plotted into histograms, and the results are plotted in Fig. 5.9 (b). It reveals that the histograms of the CB and SB possess well Gaussian distributions and overlap to each other. The intensities in the histograms are normalized by the intensity at the maximum probability (obtained by Gaussian fitting) of the CB. The related outputs are $I_{\text{max}}^{\text{CB}} = 1.00001$ and $I_{\text{max}}^{\text{SB}} = 1.00235$, and the FWHM of the CB and SB are $\Delta I_{\text{FWHM}}^{\text{CB}} = 0.13351$ and $\Delta I_{\text{FWHM}}^{\text{SB}} = 0.13529$, respective. The relative shift between the peaks of the CB and SB is defined as $\delta I_{\text{max}} = (I_{\text{max}}^{\text{CB}} - I_{\text{max}}^{\text{SB}}) / I_{\text{max}}^{\text{CB}} = -0.23\%$, which indicates that the intensity difference between the central and lateral areas of

the fluidic microchannel is quite subtle and demonstrates a well establishment of the nearly flattened illumination through the Gaussian beam.

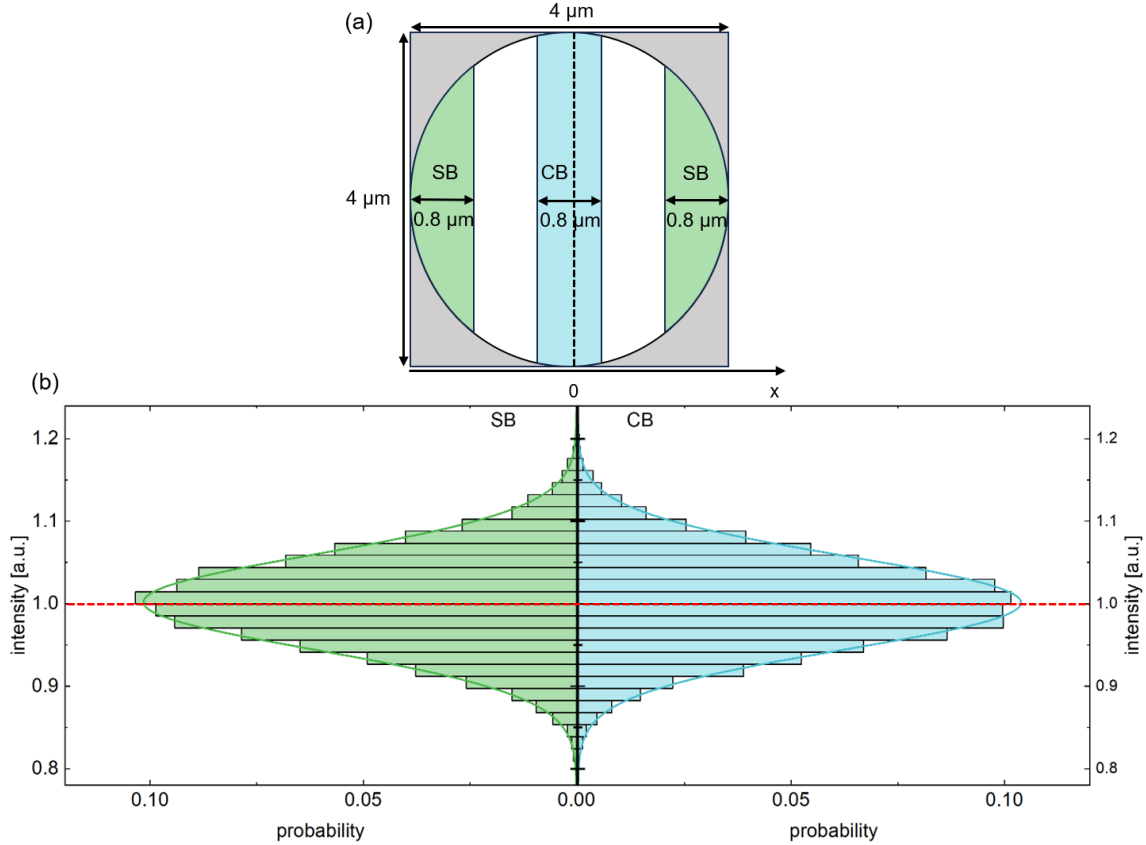


Figure 5.9: Histograms analysis of the scattered intensity using the center/side bins defined by the x -positions of the nanoparticle. The trajectory of the nanoparticle includes 65,000 frames which has been shown in Fig. 5.8 (a). (a) The defined center bin (CB) and side bin (SB) in the cross-section of the fluidic microchannel. (b) Statistical histograms of the intensities in the CB and SB. The numbers of data points used for the histograms are $N_{SB} = 14821$ and $N_{CB} = 17632$, respective.

The key results of the intensity measurement have been summarized in Table 5.1. It is worth noting that here the diameter of the fluidic channel is 4 μm, which is much larger than the ones used in NBF^{91,123}. The advantages arise from the straightforward illumination in a homogeneous medium that avoids the formation of guiding modes as well as the spatial intensity dependency inside the microchannel.

Scattered Intensity of Static Nanosphere

To quantify the intrinsic noise of the optofluidic system, the scattered intensity of an immobile nanoparticle in the microchannel was measured, and the results are shown in Fig. 5.10. The time-dependent intensity has a Gaussian distribution with a relative

standard deviation of 1.1%, which could be caused by the freely diffusing nanoparticles outside the capillary.

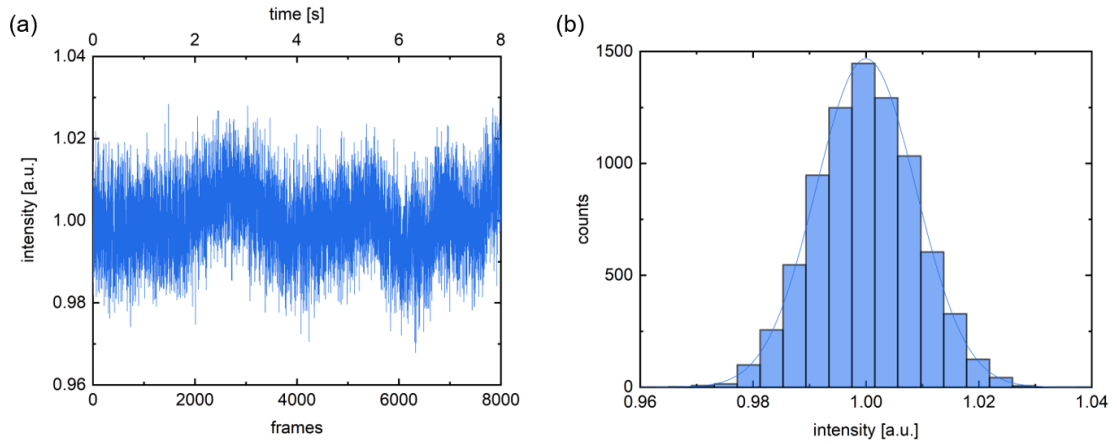


Figure 5.10: Intensity measurement of static nanoparticle in the fluidic microchannel. (a) Scattered intensity as a function of the frame index (bottom axis) and the recording time (top axis). (b) Statistical histogram of the recorded intensities with a Gaussian fitting, where the relative standard deviation is 1.1%.

Parameters	Symbol	Unit	Value
Number of frames	N_f	1	65,000
Recording time	τ	s	65
Frame rate	ν	Hz	1000
Exposure time	t_e	ms	0.2
Measured relative standard deviation of intensity	$\delta I^{\text{exp.}}$	%	5.7
Calculated relative standard deviation of intensity	$\delta I^{\text{cal.}}$	%	2.9
Peak intensity of CB	$I_{\text{max}}^{\text{CB}}$	1	1.00001
Peak intensity of SB	$I_{\text{max}}^{\text{SB}}$	1	1.00235
FWHM of CB	$\Delta I_{\text{FWHM}}^{\text{CB}}$	1	0.13351
FWHM of SB	$\Delta I_{\text{FWHM}}^{\text{SB}}$	1	0.13529
Peak shift	δI_{max}	%	-0.23

Table 5.1: Key results of the intensity measurements obtained from the NTA experiments using the fiber-assisted optofluidic device.

5.3.2 MSD Analysis

With the benefits of the flattened illumination and confinement of the microchannel, the nanoparticle can be continuously tracked with ultralong duration, providing extraordinary statistical accuracy. Note that the total number of frames in this work

may be limited by the tracking area chosen as the input part of the capillary (a length of 100 μm). The trajectory of the nanoparticle in z-direction as the index of recording frames (time) is shown in Fig. 5.11 (a). For different lag times, the displacements display well Gaussian distributions, indicating that the nanoparticle behaves with good characteristics of Brownian motion, which is shown in Fig. 5.11 (b). The diffusing coefficient of the nanoparticle was measured by fitting the first two lag times of MSD, and the output is $D = 2.23 \mu\text{m}^2/\text{s}$. The result is verified by performing PSD fitting and the obtained $D = 2.37 \mu\text{m}^2/\text{s}$. The hydrodynamic diameter can be calculated using the Stokes-Einstein relation $\tilde{d} = K_B T / 3\pi\eta D$. Considering the experimental environment, the temperature $T = 293.15 \text{ K}$, the viscosity of DMSO/water mixture is roughly $\eta = 3.3 \times 10^{-3} \text{ Pa}\cdot\text{s}$, giving the $\tilde{d} = 58.44 \text{ nm}$.

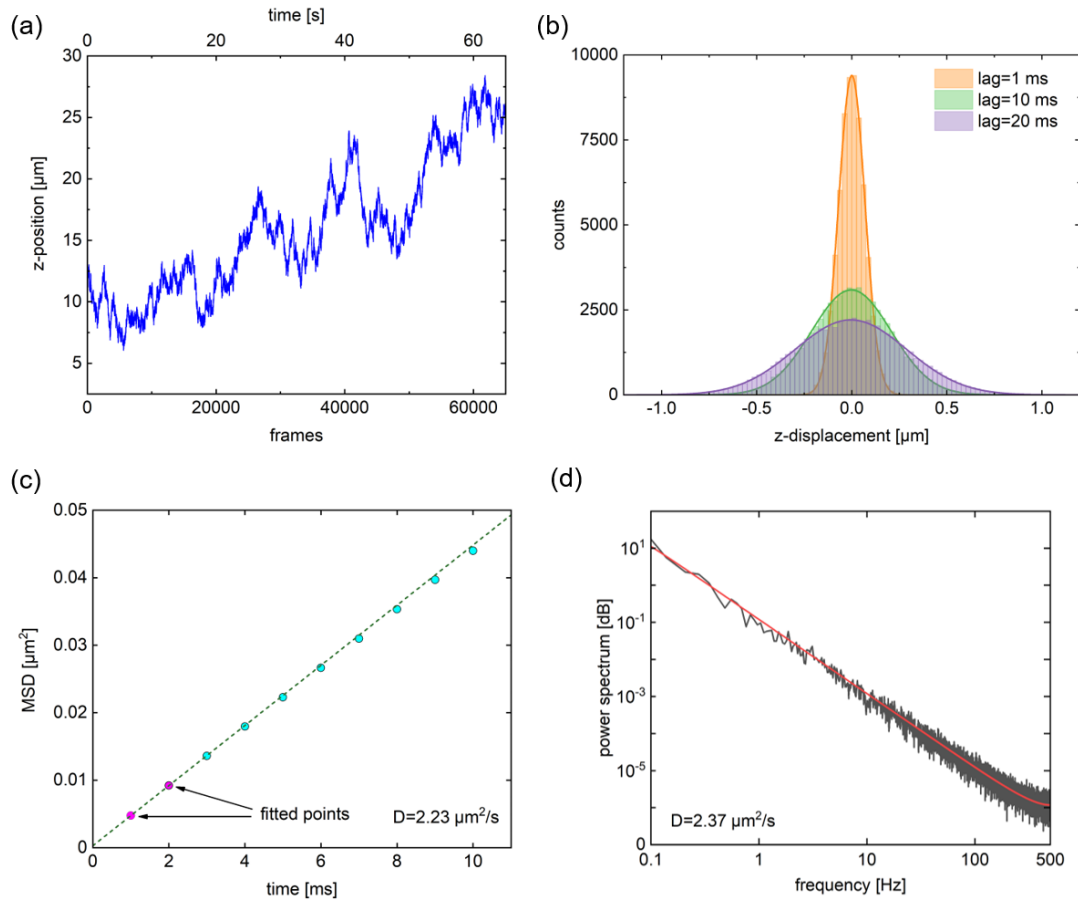


Figure 5.11: MSD analysis of the obtained trajectory of a single nanoparticle. (a) The trajectory of the nanoparticle in z-direction as a function of the frames (bottom axis) and time (top axis). (b) Statistical histograms for the displacements of the nanoparticle with different lag times of 1, 10, and 20 ms. Gaussian functions are used for the fittings of the histograms. (c) MSD fitting using the full trajectory. The first two lag times are used for the fitting. The cyan circles are the calculated MSD and the dashed line is the fitted curve. (d) PSD fitting to the trajectory.

Note that the calculated \tilde{d} is measured in a confined domain with the walls of the microchannel, which will be larger than the one diffusing in unconfined space (more discussions see section 3.3.4). As shown in Fig. 5.11 (c), note that the nanoparticle is still acting as free diffusing regarding the fact that the MSD has a linear dependency up to the first 10 lag times, which means the hindrance effect of the microchannel does only have a linear modification to the diffusion coefficient. The hindrance effect, referring to the averaged resistance factor R_{avg} , is calculated based on the theoretical model introduced in the literature¹¹⁴. The retrieved diameter of the nanosphere (unconfined) $d_f = \tilde{d}/R_{\text{avg}} = 54.82$ nm, where $R_{\text{avg}} = 1.066$ and more details about the calculation can be found in section 3.3.4.

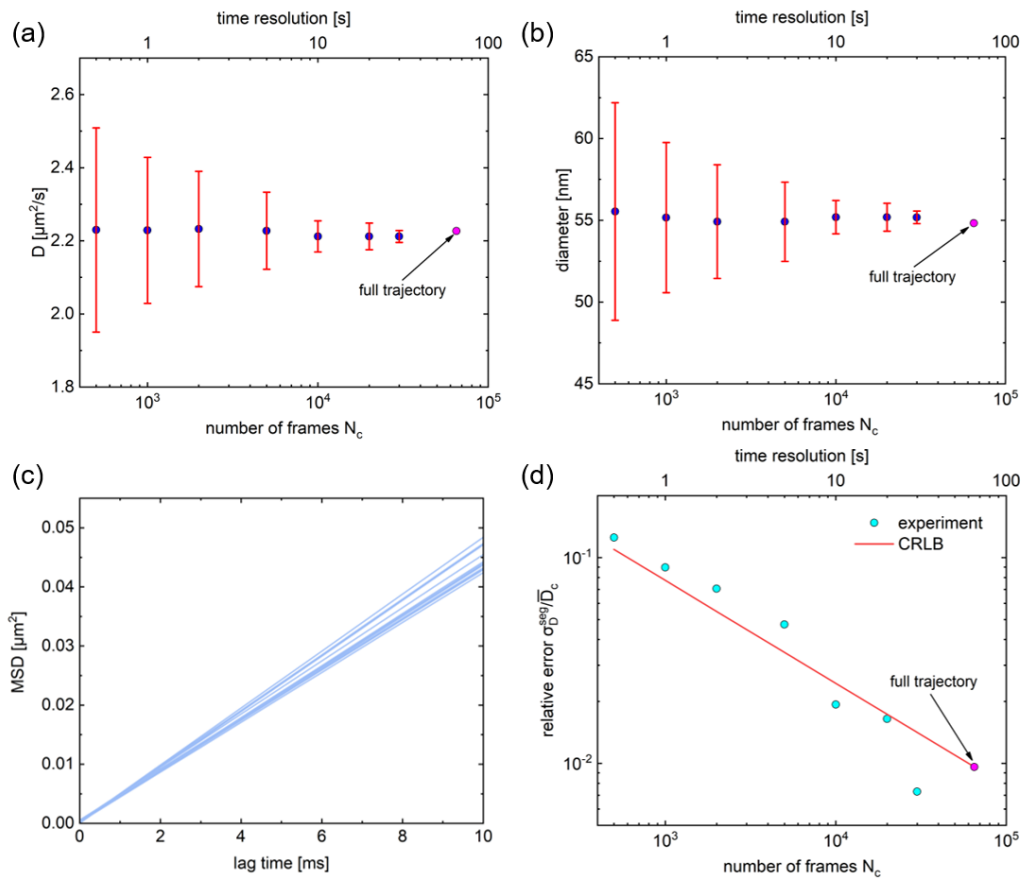


Figure 5.12: Segmented analysis of the full trajectory. (a) Diffusion coefficient D as a function of the number of frames per sub-trajectories N_c . (b) The diameter of the nanosphere retrieved from the obtained D with corrections of the hindrance effect. The error bars in (a) and (b) represent the standard deviations of the D and d_f in the assembles of sub-trajectories. (c) MSD curves with the $N_c = 5000$. (d) Relative standard deviations of the measured D as function of N_c , which are compared with the theoretical prediction by CRLB.

To reveal the accuracy of the NTA experiment in the determination of diffusion coefficient, MSD analysis was individually performed on the sub-trajectories that were

segmented from the full trajectory (65,000 frames), and the standard deviations of D were calculated. The obtained values of D and retrieved diameter d_f (corrected by the resistance factor) as functions of the frames of sub-trajectories N_c are separately shown in Figs. 5.12 (a) and (b), where the error bars refer to the standard deviations in the assemble of sub-trajectories. It indicates that the errors of D and d_f are both decreasing as the increasing of N_c , whereas the averaged D and d_f keep almost unchanged, giving the values of $2.23 \mu\text{m}^2/\text{s}$ and 55 nm , respectively.

Due to the statistical nature of MSD analysis, even though the sub-trajectories are obtained from the identical nanoparticle, there are still deviations in the slopes (D) and offsets of MSD curves. The fitted MSDs for which $N_c = 5000$ are represented in Fig. 5.12 (c). The MSDs of 13 sub-trajectories have offsets which are all near to 0, indicating the noise is very small in the measurement. The relative error of the diffusion coefficients $\sigma_D^{\text{seg}}/\bar{D}$ obtained from the sub-trajectories as a function of N_c are plotted in Fig. 5.12 (d), and compared with the theoretical CRLB. Here, the CRLB has been expressed in Eq. 2.42 and rewritten as below

$$\frac{S(D)}{D} \geq \sqrt{\frac{2}{d(N-1)}} \left(1 + 2\sqrt{1+2x}\right)^{\frac{1}{2}} \approx \sqrt{\frac{6}{N_c-1}}, \quad (5.2)$$

where $x \approx 0$ is the reduced square localization error⁴⁵, referring to a negligible localization uncertainty of the measurement.

The experimental results are in good agreement with the theoretical lower bound of errors, which demonstrates that the proposed device has been working with an ultra-low level of noise in the NTA measurement. The key results of the MSD analysis are summarized in Table 5.2.

Parameters	Symbol	Unit	Value
Diameter of the nanosphere	d	nm	50
Temperature	T	K	293.15
Viscosity of the liquid	η	Pa·s	3.3×10^{-3}
Radius of the channel	a	μm	2
Diffusion coefficient ($N_c=65,000$)	D	$\mu\text{m}^2/\text{s}$	2.23
Retrieved diameter (unconfined)	d_f	nm	54.82
Averaged resistance factor	R_{avg}	1	1.066
Relative standard deviation of D ($N_c=5000$)	$\sigma_D^{\text{seg}}/\bar{D}$	%	4.74
CRLB ($N_c=5000$)	σ_D/D	%	3.46
CRLB ($N_c=65,000$)	σ_D/D	%	0.96

Table 5.2: Key results of the MSD analysis for the segmented sub-trajectories and the estimation of errors.

5.4 Discussion

The concept of an on-chip fiber-assisted optofluidic device allows for nanoparticle tracking analysis with ultralong trajectories, which is attributed to the confinement of nanoobjects in microchannel and the flattened illumination, eliminating the spatial intensity dependence of the scattered light. The constant field in the tracking area has been demonstrated by the overlapping intensity histograms of central and lateral bins of the microchannel, and the segmented MSD analysis clarifies that the approach can provide ultralow noise in the determination of diffusion coefficient.

One key point of the working principle is the use of DMSO aqueous solution which is prepared to have the identical RI with the silica capillary fiber, to construct a homogeneous medium for the launching beam and avoid any guided mode formation. In the presence of RI-mismatches between the liquid and capillary, simulations show that two types of modes can exist in the domain of capillary fiber, the leaky mode ($n_1 < n_c$) and core mode ($n_1 > n_c$), for which the modal fields have complex distributions in both transversal and longitudinal directions. Therefore the RI-adjusted liquid needs to be calibrated and prepared carefully according to the experimental environment. The launching and capillary fibers have the same outer diameter (125 μm) and are placed on the V-groove to align their optical axes. Many freely diffusing nanoobjects can be seen in the path before the launching beam reaches the capillary fiber, which is shown in Fig. 5.7 (b). To reveal the impacts of these mobile scatters on the illumination fields in the tracking area, the scattered intensity of a static nanoparticle inside the microchannel was measured and the results are shown in Fig. 5.10. It indicates that the time-dependent intensity in the channel remains quite stable ($\delta I = 1\%$) and the disturbing introduced by the dynamic scattering in the free space can be ignored.

Another important issue of the microfluidic chip is the air bubbles that could arise from the trench of the V-groove. Thus plasma treatment has been done before loading the specimen solution on the device to improve the surface wettability and adhesion of the liquid, which can eliminate the risk of bubble formation. It is worth noting that the tracking area was selected at the part close to the entrance of the capillary ($\sim 200 \mu\text{m}$ as shown in Fig. 5.7), which is to avoid the disturbing by the reflected beams from the outer surface of the capillary fiber. This may limit the applications of the device due to the restricted tracking domain and static microfluidic environment. A potential solution is to integrate a flow-controlling system so that the targets can be purposefully selected and manipulated, which requires further design and study.

Regarding the NBF that uses the guiding mode to generate flattened fields¹²³, it requires critical structural parameters of the optical fibers, and a single mode operation as well as a particular RI of the working solution is desirable. As a consequence, the fluidic channel may be restricted to a relatively small size. Whereas, the on-chip optofluidic

device allows quite flexible scales of the channel (several micrometers in this work and larger ones are possible), which unlocks the dimensional limit of the detecting volume in NBF. With these benefits, the proposed method enhances the capability of FaNTA for ultralong tracking of single nanoobjects and opens up new possibilities in fundamental studies of light-matter interactions, for example, characterizing the rotational diffusion of nonspherical nanoparticles or for the size and RI measurements.

5.5 Chapter Summary

This work develops an on-chip fiber-assisted optofluidic device, and an NTA experiment was performed to demonstrate that the method allows for ultralong tracking of nanoparticles (65000 frames with a total observation of 60 seconds) and high accuracy of diffusion coefficient measurement (relative error of 1%). This approach can simultaneously illuminate and limit diffusing nanoparticles in microscale, particularly, providing a spatial-independent illuminating field in the fluidic domain. The unique feature of the flat field is the employment of an expanded Gaussian beam as illumination of the NTA experiment, where the intensity difference is negligible in the tracking area. The working principle is based on the RI-matched liquid filling around the optofluidic environment, leading to a vanished RI contrast between the solid-liquid components and homogeneous medium for the launching beam. Moreover, the flat field supports fluidic channels with microscale (4 μm) and the size can be further increased upon request, which is difficult to achieve in case the guiding modes are used in NBF. These advantages expand the FaNTA more application prospects in the context of life science and the fundamental study of light-matter interactions.

6 | Summary and Outlook

6.1 Summary of the Thesis

Chapter 1 starts from the background of Brownian motion of nanoparticles in liquid environments and reviews the concept of NTA and its state-of-the-art applications in multiple research fields. The chapter then introduces the FaNTA method and discusses the advantages compared to the conventional setups. The motivation of the thesis is to demonstrate the capability of FaNTA in ultralong tracking of label-free and fast-diffusing single nanoparticles. Moreover, two schemes are proposed to further improve the performance by utilizing the flattened light fields in microstructured fibers.

Chapter 2 introduces the fundamentals of fiber optics including step-index optical fiber and nanobore fiber, and the general condition of flat-field mode is given for waveguides working with the total internal reflection. Then the theoretical description of Brownian motion and the MSD method are presented. In addition, the PSD method is introduced as an alternative approach to determine the diffusion coefficient from the data of trajectory.

Chapter 3 presents an ultralong tracking of 50 nm gold nanosphere (typically 100,000 frames and 40 s duration obtained) by using NBF. This work clarifies the advantages of NBF in continuous tracking of fast-diffusing single nanoobjects, which is due to the fluidic nanochannel that spatially confines the targets in the FoV. It demonstrates that the FaNTA is a useful platform in the dynamic characterization of nanoparticles or associated fluids environment, in particular, it provides extraordinarily high accuracy in the measurement of diffusion coefficient.

Chapter 4 points out an issue with using NBFs for NTA experiments: the length of the tracking could be limited by the variant scattered signal arising from the spatial-dependent intensity of the guided modes in optical fiber. To overcome this problem, this work introduces a scheme to establish a flat mode—light strand—in the fluidic nanochannel of NBF. The key feature of the light strand is the constant modal intensity in all three dimensions of the tracking domain, which can significantly improve the depth of focus for the NTA experiments. Besides, the flat mode is experimentally demonstrated by analyzing the scattered light from a single nanoparticle diffusing in the nanochannel, and the mode transition from Gaussian to evanescent is observed via temperature-induced RI tunes of the liquid.

Chapter 5 presents an on-chip approach to realize the flat-field illumination for NTA experiments by employing a fiber-assisted optofluidic device. The idea is to use a divergent Gaussian beam for direct illumination of nanoparticles, and the changes

in intensity of the beam are negligible within the tracking area. The concept has been experimentally demonstrated by analyzing the scattered intensity from the central and lateral regions of the microchannel, where 65000 frames (65 s duration) are typically obtained and the intensity distribution is almost flat (3% relative fluctuation). Compared to the light strand implemented in NBF, this method is free of guided modes and allows larger-sized fluidic channels to accommodate more samples of interest, which brings a new optofluidic platform in the context of NTA.

The main contributions of the thesis include two aspects: (i) to reveal the ability of FaNTA in dynamic monitoring of nanoobjects with ultralong time and high localization accuracy; (ii) to increase the focal depth of NTA experiments by employing the flattened light fields within the observation area. The results indicate that FaNTA has application prospects in the research fields, such as biochemistry sensing, nanomaterials science, and the fundamental study of light-matter interactions.

6.2 Outlook

As an outlook of the current works, the smallest limit of the detectable nanoparticle in FaNTA with flattened modes needs to be investigated. So far, the size measurement of sub-10 nm nanoobjects using antiresonant-element optical fiber has been reported¹⁷². The NBF could also provide an opportunity to break through the limit in case the illuminating fields are enhanced and flattened. Furthermore, the flat-field FaNTA is an ideal platform for the intensity-based measurement of the scattered light. For example, the rotational diffusion of non-spherical nanoparticles, such as nanorods, produce varying scattered intensity to the azimuth angles of the cylindrical axis¹⁷³. Another possible application of the flat field is the RI determination of dielectric nanoparticles¹²², which relies on the measurement of the scattering cross-section. In addition, the general condition of the flat field could be applied to other types of microstructured waveguides, e.g., square-shaped microgap waveguide^{146,174}, microstructured graded index fiber¹⁰², nanoslot waveguide¹³⁷ and cylindrical photonic-bandgap fibers^{80,175}. More detailed perspectives can be found at the end of each chapter.

Besides, regarding the applications of FaNTA in the fields of bioanalytics and life sciences, future studies could focus on the interactions between nanoparticles and biological macromolecules. For example, it was reported that the conformations of a single protein can be monitored by using a nanoparticle-based plasmon ruler¹⁷⁶. The FaNTA is a potential approach used for that in case the samples can be prepared in proper solutions. Furthermore, virus particles can also be analyzed by using FaNTA, and the experiments for coronavirus have been reported¹⁷⁷. In particular, the FaNTA with a flat field may achieve better detection limits, enabling the characterization of smaller-sized viruses.

References

1. Gallego-Urrea, J. A., Tuoriniemi, J. & Hassellöv, M. Applications of particle-tracking analysis to the determination of size distributions and concentrations of nanoparticles in environmental, biological and food samples. *TrAC Trends in Analytical Chemistry* **30**, 473–483 (2011).
2. Lee, S. *et al.* Nanoparticle size detection limits by single particle icp-ms for 40 elements. *Environmental Science & Technology* **48**, 10291–10300 (2014).
3. Walkey, C. D., Olsen, J. B., Guo, H., Emili, A. & Chan, W. C. Nanoparticle size and surface chemistry determine serum protein adsorption and macrophage uptake. *Journal of the American Chemical Society* **134**, 2139–2147 (2012).
4. Montes-Burgos, I. *et al.* Characterisation of nanoparticle size and state prior to nanotoxicological studies. *Journal of Nanoparticle Research* **12**, 47–53 (2010).
5. Park, M. V. *et al.* The effect of particle size on the cytotoxicity, inflammation, developmental toxicity and genotoxicity of silver nanoparticles. *Biomaterials* **32**, 9810–9817 (2011).
6. De Jonge, N. & Ross, F. M. Electron microscopy of specimens in liquid. *Nature Nanotechnology* **6**, 695–704 (2011).
7. Frisken, B. J. Revisiting the method of cumulants for the analysis of dynamic light-scattering data. *Applied Optics* **40**, 4087–4091 (2001).
8. Hassan, P. A., Rana, S. & Verma, G. Making sense of brownian motion: colloid characterization by dynamic light scattering. *Langmuir* **31**, 3–12 (2015).
9. Stetefeld, J., McKenna, S. A. & Patel, T. R. Dynamic light scattering: a practical guide and applications in biomedical sciences. *Biophysical Reviews* **8**, 409–427 (2016).
10. Lim, J., Yeap, S. P., Che, H. X. & Low, S. C. Characterization of magnetic nanoparticle by dynamic light scattering. *Nanoscale Research Letters* **8**, 1–14 (2013).
11. Filipe, V., Hawe, A. & Jiskoot, W. Critical evaluation of nanoparticle tracking analysis (NTA) by nanosight for the measurement of nanoparticles and protein aggregates. *Pharmaceutical Research* **27**, 796–810 (2010).
12. Einstein, A. Über die von der molekularkinetischen theorie der wärme geforderte bewegung von in ruhenden flüssigkeiten suspendierten teilchen. *Annalen der Physik* **332**, 549–560 (1905).
13. Bian, X., Kim, C. & Karniadakis, G. E. 111 years of brownian motion. *Soft Matter* **12**, 6331–6346 (2016).
14. Szakács, Z., Mészáros, T., de Jonge, M. I. & Gyurcsányi, R. E. Selective counting and sizing of single virus particles using fluorescent aptamer-based nanoparticle tracking analysis. *Nanoscale* **10**, 13942–13948 (2018).
15. Zhang, W. *et al.* Characterization of exosomes derived from ovarian cancer cells and normal ovarian epithelial cells by nanoparticle tracking analysis. *Tumor Biology* **37**, 4213–4221 (2016).
16. Soo, C. Y. *et al.* Nanoparticle tracking analysis monitors microvesicle and exosome secretion from immune cells. *Immunology* **136**, 192–197 (2012).
17. Dragovic, R. A. *et al.* Sizing and phenotyping of cellular vesicles using nanoparticle tracking analysis. *Nanomedicine: Nanotechnology, Biology and Medicine* **7**, 780–788 (2011).
18. Taylor, R. W. *et al.* Interferometric scattering microscopy reveals microsecond nanoscopic protein motion on a live cell membrane. *Nature Photonics* **13**, 480–487 (2019).
19. Bachurski, D. *et al.* Extracellular vesicle measurements with nanoparticle tracking analysis—an accuracy and repeatability comparison between nanosight ns300 and zetaview. *Journal of Extracellular Vesicles* **8**, 1596016 (2019).

-
20. Dehghani, M., Gulvin, S. M., Flax, J. & Gaborski, T. R. Systematic evaluation of pkh labelling on extracellular vesicle size by nanoparticle tracking analysis. *Scientific Reports* **10**, 9533 (2020).
 21. Errington, R. J. *et al.* Single cell nanoparticle tracking to model cell cycle dynamics and compartmental inheritance. *Cell Cycle* **9**, 121–130 (2010).
 22. Wu, H.-M., Lin, Y.-H., Yen, T.-C. & Hsieh, C.-L. Nanoscopic substructures of raft-mimetic liquid-ordered membrane domains revealed by high-speed single-particle tracking. *Scientific Reports* **6**, 20542 (2016).
 23. Kusumi, A., Sako, Y. & Yamamoto, M. Confined lateral diffusion of membrane receptors as studied by single particle tracking (nanovid microscopy). effects of calcium-induced differentiation in cultured epithelial cells. *Biophysical Journal* **65**, 2021–2040 (1993).
 24. Hsieh, C.-L., Spindler, S., Ehrig, J. & Sandoghdar, V. Tracking single particles on supported lipid membranes: multimobility diffusion and nanoscopic confinement. *The Journal of Physical Chemistry B* **118**, 1545–1554 (2014).
 25. Ryu, J. H., Bang, S. Y., Yoon, J.-W., Lim, C. S. & Shim, K. B. Pulsed laser induced synthesis of scheelite-type colloidal nanoparticles in liquid and the size distribution by nanoparticle tracking analysis. *Applied Surface Science* **253**, 8408–8414 (2007).
 26. Mair, L. & Superfine, R. Single particle tracking reveals biphasic transport during nanorod magnetophoresis through extracellular matrix. *Soft Matter* **10**, 4118–4125 (2014).
 27. Gong, X. *et al.* Single-particle tracking for understanding polydisperse nanoparticle dispersions. *Small* **15**, 1901468 (2019).
 28. Tang, S. *et al.* Enzyme-powered janus platelet cell robots for active and targeted drug delivery. *Science Robotics* **5**, eaba6137 (2020).
 29. Tu, Y. *et al.* Biodegradable hybrid stomatocyte nanomotors for drug delivery. *ACS Nano* **11**, 1957–1963 (2017).
 30. Navarro Sanchez, M. *et al.* Rabies vaccine characterization by nanoparticle tracking analysis. *Scientific Reports* **10**, 8149 (2020).
 31. von Diezmann, L., Shechtman, Y. & Moerner, W. Three-dimensional localization of single molecules for super-resolution imaging and single-particle tracking. *Chemical Reviews* **117**, 7244–7275 (2017).
 32. Manley, S. *et al.* High-density mapping of single-molecule trajectories with photoactivated localization microscopy. *Nature Methods* **5**, 155–157 (2008).
 33. Pouget, N. *et al.* Single-particle tracking for dna tether length monitoring. *Nucleic Acids Research* **32**, e73–e73 (2004).
 34. Spillane, K. M. *et al.* High-speed single-particle tracking of gm1 in model membranes reveals anomalous diffusion due to interleaflet coupling and molecular pinning. *Nano Letters* **14**, 5390–5397 (2014).
 35. Alcor, D., Gouzer, G. & Triller, A. Single-particle tracking methods for the study of membrane receptors dynamics. *European Journal of Neuroscience* **30**, 987–997 (2009).
 36. Bayle, V. *et al.* Single-particle tracking photoactivated localization microscopy of membrane proteins in living plant tissues. *Nature Protocols* **16**, 1600–1628 (2021).
 37. Ewers, H. *et al.* Single-particle tracking of murine polyoma virus-like particles on live cells and artificial membranes. *Proceedings of the National Academy of Sciences* **102**, 15110–15115 (2005).
 38. Saxton, M. J. & Jacobson, K. Single-particle tracking: applications to membrane dynamics. *Annual Review of Biophysics and Biomolecular Structure* **26**, 373–399 (1997).
 39. Renner, M., Wang, L., Levi, S., Hennekinne, L. & Triller, A. A simple and powerful analysis of lateral subdiffusion using single particle tracking. *Biophysical Journal* **113**, 2452–2463 (2017).

-
40. Weiss, M. Single-particle tracking data reveal anticorrelated fractional brownian motion in crowded fluids. *Physical Review E* **88**, 010101 (2013).
 41. Jin, S., Haggie, P. M. & Verkman, A. S. Single-particle tracking of membrane protein diffusion in a potential: simulation, detection, and application to confined diffusion of cftr cl- channels. *Biophysical Journal* **93**, 1079–1088 (2007).
 42. Langevin, P. Sur la théorie du mouvement brownien. *Compt. Rendus* **146**, 530–533 (1908).
 43. Uhlenbeck, G. E. & Ornstein, L. S. On the theory of the brownian motion. *Physical Review* **36**, 823 (1930).
 44. Michalet, X. Mean square displacement analysis of single-particle trajectories with localization error: Brownian motion in an isotropic medium. *Physical Review E* **82**, 041914 (2010).
 45. Michalet, X. & Berglund, A. J. Optimal diffusion coefficient estimation in single-particle tracking. *Physical Review E* **85**, 061916 (2012).
 46. Qian, H., Sheetz, M. P. & Elson, E. L. Single particle tracking. analysis of diffusion and flow in two-dimensional systems. *Biophysical Journal* **60**, 910–921 (1991).
 47. Wagner, T., Lipinski, H.-G. & Wiemann, M. Dark field nanoparticle tracking analysis for size characterization of plasmonic and non-plasmonic particles. *Journal of Nanoparticle Research* **16**, 1–10 (2014).
 48. Haiden, C., Wopelka, T., Jech, M., Keplinger, F. & Vellekoop, M. J. Sizing of metallic nanoparticles confined to a microfluidic film applying dark-field particle tracking. *Langmuir* **30**, 9607–9615 (2014).
 49. Qian, W., Huang, X., Kang, B. & El-Sayed, M. A. Dark-field light scattering imaging of living cancer cell component from birth through division using bioconjugated gold nanoprobe. *Journal of Biomedical Optics* **15**, 046025–046025 (2010).
 50. Chen, S. *et al.* Label free imaging and deep tracking of single biological nanoparticles in free solution by reflection enhanced dark field scattering microscopy. *Sensors and Actuators B: Chemical* **355**, 131317 (2022).
 51. Kukura, P. *et al.* High-speed nanoscopic tracking of the position and orientation of a single virus. *Nature Methods* **6**, 923–927 (2009).
 52. Faez, S. *et al.* Fast, label-free tracking of single viruses and weakly scattering nanoparticles in a nanofluidic optical fiber. *ACS Nano* **9**, 12349–12357 (2015).
 53. Sleiffer, V. A. *et al.* High capacity mode-division multiplexed optical transmission in a novel 37-cell hollow-core photonic bandgap fiber. *Journal of lightwave technology* **32**, 854–863 (2013).
 54. Zhang, H. *et al.* A new type circular photonic crystal fiber for orbital angular momentum mode transmission. *IEEE Photonics Technology Letters* **28**, 1426–1429 (2016).
 55. Slater, J. A. *et al.* Microstructured fiber source of photon pairs at widely separated wavelengths. *Optics Letters* **35**, 499–501 (2010).
 56. Limpert, J. *et al.* High-power rod-type photonic crystal fiber laser. *Optics Express* **13**, 1055–1058 (2005).
 57. Bouillet, J. *et al.* High power ytterbium-doped rod-type three-level photonic crystal fiber laser. *Optics Express* **16**, 17891–17902 (2008).
 58. Aghbolagh, F. *et al.* Mid ir hollow core fiber gas laser emitting at 4.6 μm . *Optics Letters* **44**, 383–386 (2019).
 59. Wang, Z., Yu, F., Wadsworth, W. J. & Knight, J. C. Efficient 1.9 μm emission in h2-filled hollow core fiber by pure stimulated vibrational raman scattering. *Laser Physics Letters* **11**, 105807 (2014).
 60. Town, G. E., Yuan, W., McCosker, R. & Bang, O. Microstructured optical fiber refractive index sensor. *Optics Letters* **35**, 856–858 (2010).

-
61. Zhao, Y., Deng, Z.-q. & Li, J. Photonic crystal fiber based surface plasmon resonance chemical sensors. *Sensors and Actuators B: Chemical* **202**, 557–567 (2014).
 62. Wu, D. K., Kuhlmeiy, B. T. & Eggleton, B. J. Ultrasensitive photonic crystal fiber refractive index sensor. *Optics Letters* **34**, 322–324 (2009).
 63. Chen, T. *et al.* Regenerated gratings in air-hole microstructured fibers for high-temperature pressure sensing. *Optics letters* **36**, 3542–3544 (2011).
 64. Jin, L., Guan, B.-O. & Wei, H. Sensitivity characteristics of fabry-perot pressure sensors based on hollow-core microstructured fibers. *Journal of Lightwave Technology* **31**, 2526–2532 (2013).
 65. Jewart, C. *et al.* Sensitivity enhancement of fiber bragg gratings to transverse stress by using microstructural fibers. *Optics Letters* **31**, 2260–2262 (2006).
 66. Warren-Smith, S. C., Nguyen, L. V., Lang, C., Ebendorff-Heidepriem, H. & Monro, T. M. Temperature sensing up to 1300 c using suspended-core microstructured optical fibers. *Optics Express* **24**, 3714–3719 (2016).
 67. Zuo, Y. *et al.* Optical fibres with embedded two-dimensional materials for ultrahigh nonlinearity. *Nature Nanotechnology* **15**, 987–991 (2020).
 68. Gu, B. *et al.* Nonlinear fiber-optic strain sensor based on four-wave mixing in microstructured optical fiber. *Optics Letters* **37**, 794–796 (2012).
 69. Yamamoto, T., Kubota, H., Kawanishi, S., Tanaka, M. & Yamaguchi, S. Supercontinuum generation at 1.55 μm in a dispersion-flattened polarization-maintaining photonic crystal fiber. *Optics Express* **11**, 1537–1540 (2003).
 70. Singh, N. *et al.* Octave-spanning coherent supercontinuum generation in silicon on insulator from 1.06 μm to beyond 2.4 μm . *Light: Science & Applications* **7**, 17131–17131 (2018).
 71. Cheng, T. *et al.* Soliton self-frequency shift and third-harmonic generation in a four-hole as 2 s 5 microstructured optical fiber. *Optics Express* **22**, 3740–3746 (2014).
 72. He, W. *et al.* Formation of optical supramolecular structures in a fibre laser by tailoring long-range soliton interactions. *Nature Communications* **10**, 5756 (2019).
 73. Sazio, P. J. *et al.* Microstructured optical fibers as high-pressure microfluidic reactors. *Science* **311**, 1583–1586 (2006).
 74. Bertucci, A. *et al.* Detection of unamplified genomic dna by a pna-based microstructured optical fiber (mof) bragg-grating optofluidic system. *Biosensors and Bioelectronics* **63**, 248–254 (2015).
 75. Williams, G. O., Chen, J. S., Euser, T. G., Russell, P. S. J. & Jones, A. C. Photonic crystal fibre as an optofluidic reactor for the measurement of photochemical kinetics with sub-picomole sensitivity. *Lab on a Chip* **12**, 3356–3361 (2012).
 76. Thakur, H. V., Nalawade, S. M., Gupta, S., Kitture, R. & Kale, S. Photonic crystal fiber injected with fe₃o₄ nanofluid for magnetic field detection. *Applied Physics Letters* **99** (2011).
 77. Zhang, N. *et al.* Ultra-sensitive chemical and biological analysis via specialty fibers with built-in microstructured optofluidic channels. *Lab on a Chip* **18**, 655–661 (2018).
 78. Zeltner, R., Xie, S., Pennetta, R. & Russell, P. S. J. Broadband, lensless, and optomechanically stabilized coupling into microfluidic hollow-core photonic crystal fiber using glass nanospike. *ACS Photonics* **4**, 378–383 (2017).
 79. Snyder, A. W., Love, J. D. *et al.* *Optical waveguide theory*, vol. 175 (Chapman and hall London, 1983).
 80. Yeh, P., Yariv, A. & Marom, E. Theory of bragg fiber. *Journal of the Optical Society of America* **68**, 1196–1201 (1978).
 81. Zienkiewicz, O. C., Taylor, R. L. & Zhu, J. Z. *The finite element method: its basis and fundamentals* (Elsevier, 2005).

-
82. Kubo, R. Brownian motion and nonequilibrium statistical mechanics. *Science* **233**, 330–334 (1986).
 83. Cecconi, F., Cencini, M., Falcioni, M. & Vulpiani, A. Brownian motion and diffusion: From stochastic processes to chaos and beyond. *Chaos: An Interdisciplinary Journal of Nonlinear Science* **15** (2005).
 84. Saffman, P. Brownian motion in thin sheets of viscous fluid. *Journal of Fluid Mechanics* **73**, 593–602 (1976).
 85. van Zanten, J. H. & Rufener, K. P. Brownian motion in a single relaxation time maxwell fluid. *Physical Review E* **62**, 5389 (2000).
 86. Petrov, E. P., Petrosyan, R. & Schwille, P. Translational and rotational diffusion of micrometer-sized solid domains in lipid membranes. *Soft Matter* **8**, 7552–7555 (2012).
 87. Bayles, A. V., Squires, T. M. & Helgeson, M. E. Dark-field differential dynamic microscopy. *Soft Matter* **12**, 2440–2452 (2016).
 88. Yanagida, T., Ueda, M., Murata, T., Esaki, S. & Ishii, Y. Brownian motion, fluctuation and life. *Biosystems* **88**, 228–242 (2007).
 89. Li, G., Tam, L.-K. & Tang, J. X. Amplified effect of brownian motion in bacterial near-surface swimming. *Proceedings of the National Academy of Sciences* **105**, 18355–18359 (2008).
 90. Frey, E. & Kroy, K. Brownian motion: a paradigm of soft matter and biological physics. *Annalen der Physik* **517**, 20–50 (2005).
 91. Gui, F. *et al.* Ultralong tracking of fast-diffusing nano-objects inside nanofluidic channel-enhanced microstructured optical fiber. *Advanced Photonics Research* **2**, 2100032 (2021).
 92. Jiang, S. *et al.* Three dimensional spatiotemporal nano-scale position retrieval of the confined diffusion of nano-objects inside optofluidic microstructured fibers. *Nanoscale* **12**, 3146–3156 (2020).
 93. Berg-Sørensen, K. & Flyvbjerg, H. Power spectrum analysis for optical tweezers. *Review of Scientific Instruments* **75**, 594–612 (2004).
 94. Wong, W. P. & Halvorsen, K. The effect of integration time on fluctuation measurements: calibrating an optical trap in the presence of motion blur. *Optics Express* **14**, 12517–12531 (2006).
 95. Lansdorp, B. M. & Saleh, O. A. Power spectrum and allan variance methods for calibrating single-molecule video-tracking instruments. *Review of Scientific Instruments* **83** (2012).
 96. Welch, P. The use of fast fourier transform for the estimation of power spectra: a method based on time averaging over short, modified periodograms. *IEEE Transactions on Audio and Electroacoustics* **15**, 70–73 (1967).
 97. Metzler, R., Jeon, J.-H. & Cherstvy, A. Non-brownian diffusion in lipid membranes: Experiments and simulations. *Biochimica et Biophysica Acta (BBA)-Biomembranes* **1858**, 2451–2467 (2016).
 98. Granik, N. *et al.* Single-particle diffusion characterization by deep learning. *Biophysical Journal* **117**, 185–192 (2019).
 99. Ernst, D. & Köhler, J. Measuring a diffusion coefficient by single-particle tracking: statistical analysis of experimental mean squared displacement curves. *Physical Chemistry Chemical Physics* **15**, 845–849 (2013).
 100. Lin, Y.-H., Chang, W.-L. & Hsieh, C.-L. Shot-noise limited localization of single 20 nm gold particles with nanometer spatial precision within microseconds. *Optics Express* **22**, 9159–9170 (2014).
 101. Faez, S. *et al.* Nanocapillary electrokinetic tracking for monitoring charge fluctuations on a single nanoparticle. *Faraday Discussions* **193**, 447–458 (2016).

-
102. Jiang, S. *et al.* Three-dimensional spatiotemporal tracking of nano-objects diffusing in water-filled optofluidic microstructured fiber. *Nanophotonics* **9**, 4545–4554 (2020).
 103. Foerster, R. *et al.* Tracking and analyzing the brownian motion of nano-objects inside hollow core fibers. *ACS Sensors* **5**, 879–886 (2020).
 104. Schaarschmidt, K., Weidlich, S., Reul, D. & Schmidt, M. A. Bending losses and modal properties of nano-bore optical fibers. *Optics Letters* **43**, 4192–4195 (2018).
 105. Tuniz, A., Weidlich, S. & Schmidt, M. A. Effectively single-mode self-recovering ultrafast non-linear nanowire surface plasmons. *Physical Review Applied* **9**, 044012 (2018).
 106. Jiang, S., Schaarschmidt, K., Weidlich, S. & Schmidt, M. A. Fiber-integrated absorption spectroscopy using liquid-filled nanobore optical fibers. *Journal of Lightwave Technology* **36**, 3970–3975 (2018).
 107. Washburn, E. W. The dynamics of capillary flow. *Physical Review* **17**, 273 (1921).
 108. Faez, S., Carattino, A. & Mosk, A. PyNTA: An open source software application for live particle tracking. *Preprints* (2019). URL <https://doi.org/10.20944/preprints201906.0251.v1>.
 109. Plidschun, M. *et al.* Ultrahigh numerical aperture meta-fibre for flexible optical trapping. *Light: Science & Applications* **10**, 57 (2021).
 110. Plidschun, M. *et al.* Nanobore fiber focus trap with enhanced tuning capabilities. *Optics Express* **27**, 36221–36230 (2019).
 111. Yu, Z. *et al.* A force calibration standard for magnetic tweezers. *Review of Scientific Instruments* **85** (2014).
 112. Benesch, T., Yiacoymi, S. & Tsouris, C. Brownian motion in confinement. *Physical Review E* **68**, 021401 (2003).
 113. Wagner, T., Kroll, A., Haramagatti, C. R., Lipinski, H.-G. & Wiemann, M. Classification and segmentation of nanoparticle diffusion trajectories in cellular micro environments. *PloS one* **12**, e0170165 (2017).
 114. Higdon, J. & Muldowney, G. Resistance functions for spherical particles, droplets and bubbles in cylindrical tubes. *Journal of Fluid Mechanics* **298**, 193–210 (1995).
 115. Kim, J. *et al.* Locally structured on-chip optofluidic hollow-core light cages for single nanoparticle tracking. *ACS Sensors* **7**, 2951–2959 (2022).
 116. Wang, X., Yi, H., Gdor, I., Hereld, M. & Scherer, N. F. Nanoscale resolution 3D snapshot particle tracking by multifocal microscopy. *Nano Letters* **19**, 6781–6787 (2019).
 117. Ruggeri, F. *et al.* Single-molecule electrometry. *Nature Nanotechnology* **12**, 488–495 (2017).
 118. Skaug, M. J., Schwemmer, C., Fringes, S., Rawlings, C. D. & Knoll, A. W. Nanofluidic rocking brownian motors. *Science* **359**, 1505–1508 (2018).
 119. Feng, J., Zhang, Z., Wen, X., Xue, J. & He, Y. Single nanoparticle tracking reveals efficient long-distance undercurrent transport in upper fluid of bacterial swarms. *iScience* **22**, 123–132 (2019).
 120. Gardiner, C., Ferreira, Y. J., Dragovic, R. A., Redman, C. W. & Sargent, I. L. Extracellular vesicle sizing and enumeration by nanoparticle tracking analysis. *Journal of Extracellular Vesicles* **2**, 19671 (2013).
 121. Moschakis, T. Microrheology and particle tracking in food gels and emulsions. *Current Opinion in Colloid & Interface Science* **18**, 311–323 (2013).
 122. Van Der Pol, E., Coumans, F. A., Sturk, A., Nieuwland, R. & Van Leeuwen, T. G. Refractive index determination of nanoparticles in suspension using nanoparticle tracking analysis. *Nano Letters* **14**, 6195–6201 (2014).
 123. Gui, F. *et al.* Light strands: exploring flat-field modes in optofluidic fibers for tracking single nano-objects. *Optica* **10**, 717–724 (2023).

-
124. Forbes, A., de Oliveira, M. & Dennis, M. R. Structured light. *Nature Photonics* **15**, 253–262 (2021).
 125. Rubinsztein-Dunlop, H. *et al.* Roadmap on structured light. *Journal of Optics* **19**, 013001 (2016).
 126. Cao, R. *et al.* Optical-resolution photoacoustic microscopy with a needle-shaped beam. *Nature Photonics* **17**, 89–95 (2023).
 127. Chen, B.-C. *et al.* Lattice light-sheet microscopy: imaging molecules to embryos at high spatiotemporal resolution. *Science* **346**, 1257998 (2014).
 128. Power, R. M. & Huisken, J. A guide to light-sheet fluorescence microscopy for multiscale imaging. *Nature Methods* **14**, 360–373 (2017).
 129. Gao, L., Shao, L., Chen, B.-C. & Betzig, E. 3D live fluorescence imaging of cellular dynamics using bessel beam plane illumination microscopy. *Nature Protocols* **9**, 1083–1101 (2014).
 130. Kim, G. *et al.* Metasurface-driven full-space structured light for three-dimensional imaging. *Nature Communications* **13**, 5920 (2022).
 131. Yu, N. & Capasso, F. Flat optics with designer metasurfaces. *Nature Materials* **13**, 139–150 (2014).
 132. Shi, L., Li, B. & Matusik, W. End-to-end learning of 3D phase-only holograms for holographic display. *Light: Science & Applications* **11**, 247 (2022).
 133. Plidschun, M., Zeisberger, M., Kim, J., Wieduwilt, T. & Schmidt, M. A. Fiber-based 3D nano-printed holography with individually phase-engineered remote points. *Scientific Reports* **12**, 20920 (2022).
 134. Pal, V. *et al.* Generating flat-top beams with extended depth of focus. *Applied Optics* **57**, 4583–4589 (2018).
 135. Jollivet, C. *et al.* Specialty flat-top beam delivery fibers with controlled beam parameter product. *Proc. SPIE* **9727**, 97270T (2016).
 136. Litvin, I. A. & Forbes, A. Intra-cavity flat-top beam generation. *Optics Express* **17**, 15891–15903 (2009).
 137. Makela, M. & Lin, P. T. Detection of sars-cov-2 dna targets using femtoliter optofluidic waveguides. *Analytical Chemistry* **93**, 4154–4159 (2021).
 138. Koos, C. *et al.* All-optical high-speed signal processing with silicon-organic hybrid slot waveguides. *Nature Photonics* **3**, 216–219 (2009).
 139. Rodrigues, J. R. *et al.* All-dielectric scale invariant waveguide. *Nature Communications* **14**, 6675 (2023).
 140. Wiederhecker, G. *et al.* Field enhancement within an optical fibre with a subwavelength air core. *Nature Photonics* **1**, 115–118 (2007).
 141. Uebel, P., Schmidt, M. A., Scharrer, M. & Russell, P. S. J. An azimuthally polarizing photonic crystal fibre with a central gold nanowire. *New Journal of Physics* **13**, 063016 (2011).
 142. Šimić, M. *et al.* Real-time nanoparticle characterization through optofluidic force induction. *Physical Review Applied* **18**, 024056 (2022).
 143. Bag, A., Neugebauer, M., Woźniak, P., Leuchs, G. & Banzer, P. Transverse kerker scattering for angstrom localization of nanoparticles. *Physical Review Letters* **121**, 193902 (2018).
 144. Akmarov, K., Lapshov, S., Sherstobitova, A. & Yas'kov, A. Optical properties of aqueous solutions of dimethyl sulfoxide and application of refractometry for monitoring their composition. *Journal of Applied Spectroscopy* **80**, 610–614 (2013).
 145. Malitson, I. H. Interspecimen comparison of the refractive index of fused silica. *Journal of the Optical Society of America* **55**, 1205–1209 (1965).
 146. Burger, J. *et al.* 3D-nanoprinted antiresonant hollow-core microgap waveguide: An on-chip platform for integrated photonic devices and sensors. *ACS Photonics* **9**, 3012–3024 (2022).

-
147. Yin, D. *et al.* Planar optofluidic chip for single particle detection, manipulation, and analysis. *Lab on a Chip* **7**, 1171–1175 (2007).
 148. Nissen, M. *et al.* Nanoparticle tracking in single-antiresonant-element fiber for high-precision size distribution analysis of mono- and polydisperse samples. *Small* **18**, 2202024 (2022).
 149. LeBel, R. & Goring, D. Density, viscosity, refractive index, and hygroscopicity of mixtures of water and dimethyl sulfoxide. *Journal of Chemical and Engineering Data* **7**, 100–101 (1962).
 150. Gui, F. *et al.* Capillary-assisted flat-field formation: a platform for advancing nanoparticle tracking analysis in an integrated on-chip optofluidic environment. *Nanophotonics* (2024).
 151. Ouyang, X. *et al.* Ultrasensitive optofluidic enzyme-linked immunosorbent assay by on-chip integrated polymer whispering-gallery-mode microlaser sensors. *Lab on a Chip* **20**, 2438–2446 (2020).
 152. Gao, Y., Gan, Q., Xin, Z., Cheng, X. & Bartoli, F. J. Plasmonic mach–zehnder interferometer for ultrasensitive on-chip biosensing. *ACS Nano* **5**, 9836–9844 (2011).
 153. Du, K. *et al.* Multiplexed efficient on-chip sample preparation and sensitive amplification-free detection of ebola virus. *Biosensors and Bioelectronics* **91**, 489–496 (2017).
 154. Guo, Y. *et al.* Optofluidic fabry–pérot cavity biosensor with integrated flow-through micro-/nanochannels. *Applied Physics Letters* **98** (2011).
 155. Zeng, L. *et al.* Extraction of small extracellular vesicles by label-free and biocompatible on-chip magnetic separation. *Lab on a Chip* **22**, 2476–2488 (2022).
 156. Nie, F.-Q. *et al.* On-chip cell migration assay using microfluidic channels. *Biomaterials* **28**, 4017–4022 (2007).
 157. Huang, N.-T., Zhang, H.-l., Chung, M.-T., Seo, J. H. & Kurabayashi, K. Recent advancements in optofluidics-based single-cell analysis: optical on-chip cellular manipulation, treatment, and property detection. *Lab on a Chip* **14**, 1230–1245 (2014).
 158. Zheng, G., Lee, S. A., Yang, S. & Yang, C. Sub-pixel resolving optofluidic microscope for on-chip cell imaging. *Lab on a Chip* **10**, 3125–3129 (2010).
 159. Jahani, Y. *et al.* Imaging-based spectrometer-less optofluidic biosensors based on dielectric metasurfaces for detecting extracellular vesicles. *Nature Communications* **12**, 3246 (2021).
 160. Liu, S. *et al.* Correlated electrical and optical analysis of single nanoparticles and biomolecules on a nanopore-gated optofluidic chip. *Nano Letters* **14**, 4816–4820 (2014).
 161. Liang, L., Zuo, Y., Wu, W., Zhu, X. & Yang, Y. Optofluidic restricted imaging, spectroscopy and counting of nanoparticles by evanescent wave using immiscible liquids. *Lab on a Chip* **16**, 3007–3014 (2016).
 162. Carvalho, M. *et al.* Colorectal tumor-on-a-chip system: A 3D tool for precision onco-nanomedicine. *Science Advances* **5**, eaaw1317 (2019).
 163. Kim, C., Bang, J. H., Kim, Y. E., Lee, S. H. & Kang, J. Y. On-chip anticancer drug test of regular tumor spheroids formed in microwells by a distributive microchannel network. *Lab on a Chip* **12**, 4135–4142 (2012).
 164. Mitra, A., Deutsch, B., Ignatovich, F., Dykes, C. & Novotny, L. Nano-optofluidic detection of single viruses and nanoparticles. *ACS Nano* **4**, 1305–1312 (2010).
 165. Chung, J., Kang, J. S., Jurng, J. S., Jung, J. H. & Kim, B. C. Fast and continuous microorganism detection using aptamer-conjugated fluorescent nanoparticles on an optofluidic platform. *Biosensors and Bioelectronics* **67**, 303–308 (2015).
 166. Yazdi, S. H. & White, I. M. Optofluidic surface enhanced raman spectroscopy microsystem for sensitive and repeatable on-site detection of chemical contaminants. *Analytical Chemistry* **84**, 7992–7998 (2012).

-
167. Kim, J. *et al.* The optofluidic light cage–on-chip integrated spectroscopy using an antiresonance hollow core waveguide. *Analytical Chemistry* **93**, 752–760 (2020).
 168. Chandra Roy, A., Bangalore Subramanya, S., Manohar Rudresh, S. & Venkataraman, V. On chip optofluidic low-pressure monitoring device. *Journal of Biophotonics* **14**, e202000381 (2021).
 169. Kühn, S., Phillips, B., Lunt, E., Hawkins, A. & Schmidt, H. Ultralow power trapping and fluorescence detection of single particles on an optofluidic chip. *Lab on a Chip* **10**, 189–194 (2010).
 170. Pang, S., Han, C., Lee, L. M. & Yang, C. Fluorescence microscopy imaging with a fresnel zone plate array based optofluidic microscope. *Lab on a Chip* **11**, 3698–3702 (2011).
 171. Kowalevicz Jr, A. M. & Bucholtz, F. Beam divergence from an smf-28 optical fiber. *Naval Research Laboratory Memorandum Report* 0704–0188 (2006).
 172. Wieduwilt, T., Förster, R., Nissen, M., Kobelke, J. & Schmidt, M. A. Characterization of diffusing sub-10 nm nano-objects using single anti-resonant element optical fibers. *Nature Communications* **14**, 3247 (2023).
 173. Molaei, M., Atefi, E. & Crocker, J. C. Nanoscale rheology and anisotropic diffusion using single gold nanorod probes. *Physical Review Letters* **120**, 118002 (2018).
 174. Kim, J. *et al.* 3D-nanoprinted on-chip antiresonant waveguide with hollow core and microgaps for integrated optofluidic spectroscopy. *Optics Express* **31**, 2833–2845 (2023).
 175. Stolyarov, A. M. *et al.* Microfluidic directional emission control of an azimuthally polarized radial fibre laser. *Nature Photonics* **6**, 229–233 (2012).
 176. Ye, W. *et al.* Conformational dynamics of a single protein monitored for 24 h at video rate. *Nano Letters* **18**, 6633–6637 (2018).
 177. Förster, R., Wieduwilt, T., Nissen, M. & Schmidt, M. A. Tracking of individual nano-objects inside hollow core fibers on the example sars-cov-2. In *CLEO: Science and Innovations*, JTu1R–4 (Optica Publishing Group, 2021).

Acknowledgment

I express my deepest gratitude to my supervisor, Prof. Markus Schmidt. His full support, patient guidance and scientific insights were instrumental in forming this thesis. I sincerely thank him for the opportunity he provided for my doctoral research, which was a delightful and valuable experience in my life.

I sincerely thank Torsten Wieduwilt for his support and help during my experiments, and I would also like to thank Dr. Matthias Zeisberger for his guidance and advice with the numerical simulations.

I am grateful to my colleagues and friends, Ramona Scheibinger, Shiqi Jiang, Dr. Xue Qi, Dr. Jiangbo Zhao, Dr. Tilman Lühder, Dr. Ronny Förster, Dr. Jisoo Kim, Bumjoon Jang, Dr. Malte Plidschun and Mona Nissen. Their support and help enabled me to continuously overcome challenges in life and research work.

I am very grateful to my family for their unconditional love and support. It is the motivation that keeps me moving forward. Thank Duoli for the company during those seven years, bringing us many joyful memories.

I would like to acknowledge the China Scholarship Council (CSC) for providing me with four-year financial support to complete my PhD project in Germany (201906070166), and support from Deutsche Forschungsgemeinschaft (SCHM2655/15-1, SCHM2655/8-1, Projekt-Nr. 512648189), Volkswagen Foundation and the Open Access Publication Fund of the Thueringer Universitaets- und Landesbibliothek Jena.

Personal Information

Date of birth: 19.10.1993
 Location of birth: Chongqing
 Nationality: China
 Email: guifengji023@gmail.com

Education

10.2019 - 05.2024 PhD, Faculty of Physics and Astronomy, Friedrich Schiller University Jena
 09.2016 - 06.2019 M.Sc, School of Physics, University of Electronic Science and Technology of China (UESTC)
 09.2012 - 06.2016 B.Sc, School of Optoelectronic Science and Engineering, UESTC

Research Experiences

10.2019 - 05.2024 PhD study at Leibniz Institute of Photonic Technology (IPHT), Advisor: Prof. Markus Schmidt, thesis: Nanoparticle tracking analysis based on microstructured Waveguides
 09.2016 - 06.2019 Graduate study, Advisor: Prof. Huajun Yang, thesis: Design of high birefringence photonic crystal fiber and the applications in optical communications

Teaching Experiences

Tutor of graduate lectures: Active Photonic Device (2020WS, 2021WS), Fiber Optics (2021SS, 2022SS) by Prof. Markus Schmidt, Friedrich Schiller University Jena

Software Skills

COMSOL Multiphysics, Lumerical FDTD, Python, Matlab, LabVIEW, LaTeX

Awards

2014, UESTC, Third Academic Scholarship, Progressive Scholarship
 2015, UESTC, Second Academic Scholarship
 2016, UESTC, Admission Scholarship for Graduate Student
 2016, UESTC, Fundamental Research Scholarship
 2017, UESTC, Second Academic Scholarship
 2018, UESTC, First Academic Scholarship
 2019, CSC scholarship for abroad PhD student

Publications

Journal Articles

1. **F. Gui**, M. Schmidt, "Flattening of the electromagnetic fields in the liquid core of rectangular waveguide," (in preparation)
2. **F. Gui**, R. Förster, T. Wieduwilt, M. Zeisberger, J. Kim, M. Schmidt, "Capillary-Assisted Flat-Field Formation: a Platform for Advancing Nanoparticle Tracking Analysis in an Integrated On-Chip Optofluidic Environment," *Nanophotonics* (accepted)
3. **F. Gui**, S. Jiang, T. Wieduwilt, R. Scheibinger, J. Hofmann, R. Förster, M. Schmidt, "Light strands: exploring flat-field modes in optofluidic fibers for tracking single nano-objects," *Optica*, 10, 717-724, 2023
4. **F. Gui**, S. Jiang, R. Förster, M. Plidschun, S. Weidlich, J.B. Zhao, M. Schmidt, "Ultralong tracking of fast-diffusing nano-objects inside nanofluidic channel enhanced microstructured optical fiber," *Advanced Photonics Research*, 2, 2100032, 2021
5. **F. Gui**, P. Jiang, H. Yang, Y. Qin, and W. Caiyang, "Design for a high birefringence photonic crystal fiber with multimode and low loss," *Applied Optics*, 57, 6-13, 2018
6. Y. Wan, X. Qi, J. Hofmann, R. Scheibinger, G. Jia, **F. Gui**, J. Plentz, J. Wen, and M. Schmidt, "Optical heating-induced spectral tuning of supercontinuum generation in liquid core fibers using multiwall carbon nanotubes," *Optics Express*, 31, 30911-30920, 2023
7. Z. Chen, P. Jiang, W. Caiyang, **F. Gui**, M. Wang, H. Yang, "Higher-order modes suppression in negative curvature anti-resonance hollow core fibers by multiple resonant coupling," *Optics Communications*, 475, 126246, 2020
8. Y. Niu, P. Jiang, H. Yang, W. Caiyang, Y. Qin, **F. Gui**, "Tunable converge optical elliptical vortex based on elliptical helical lens," *Applied Physics B*, 126 (7), 1-8, 2020
9. W. Caiyang, P. Jiang, Y. Qin, S. Mao, B. Cao, **F. Gui**, H. Yang, "Design of a high-Q fiber cavity for omnidirectionally emitting laser with one-dimensional topological photonic crystal heterostructure," *Optics Express*, 27, 4176-4187, 2019

-
10. W. Caiyang, H. Yang, P. Jiang, Y. Qin, **F. Gui** and B. Cao, “Omnidirectional emission from micro-notched bragg fiber,” *Laser Physics Letters*, 16(3), 035109, 2019
 11. Y. Qin, H. Yang, P. Jiang, **F. Gui**, W. Caiyang and B. Cao, “Design and analysis for a bend-resistant and large-mode-area photonic crystal fiber with hybrid cladding,” *Applied Optics*, 57, 3976-3982, 2018

Conference Contributions

1. **F. Gui**, M. Schmidt, “Flattening of electromagnetic fields in liquid region of nanofluidic micro-structured optical fiber,” DokDok, Arnstadt, Germany, 2022

Ehrenwörtliche Erklärung

Hiermit erkläre ich ehrenwörtlich,

1. dass mir die geltende Promotionsordnung bekannt ist;
2. dass ich die Dissertation selbst angefertigt habe, keine Textabschnitte eines Dritten oder eigener Prüfungsarbeiten ohne Kennzeichnung übernommen und alle von mir benutzten Hilfsmittel, persönlichen Mitteilungen und Quellen in meiner Arbeit angegeben habe;
3. dass bei der Auswahl und Auswertung folgenden Materials mich die nachstehend aufgeführten Personen in der jeweils beschriebenen Weise unterstützt haben:
 - SEM-Messungen: Franka Jahn
 - Herstellung von V-Groove-Chips: Uwe Huebner
 - Montage eines V-groove-Chips mit Faser: Torsten Wieduwilt
 - Plasma-Behandlung für V-Groove-Chips: Jisoo Kim
4. dass die Hilfe einer kommerziellen Promotionsvermittlerin/eines kommerziellen Promotionsvermittlers nicht in Anspruch genommen wurde und dass Dritte weder unmittelbar noch mittelbar geldwerte Leistungen für Arbeiten erhalten haben, die im Zusammenhang mit dem Inhalt der vorgelegten Dissertation stehen;
5. dass die Dissertation noch nicht als Prüfungsarbeit für eine staatliche oder andere wissenschaftliche Prüfung eingereicht wurde;
6. dass eine gleiche, eine in wesentlichen Teilen ähnliche oder eine andere Abhandlung bei einer anderen Hochschule als Dissertation nicht eingereicht.

Ort, Datum

Unterschrift